SANDIA REPORT
SAND2009-7605
Unlimited Release
Printed December 2009

Validation and Uncertainty Quantification of Fuego Simulations of Calorimeter Heating in a Wind-Driven Hydrocarbon Pool Fire

Anay Luketa, Vicente Romero, Stefan Domino, David Glaze, Martin Sherman, and Victor Figueroa

Prepared by
Sandia National Laboratories
Albuquerque, New Mexico 87185 and Livermore, California 94550

Sandia is a multiprogram laboratory operated by Sandia Corporation,
a Lockheed Martin Company, for the United States Department of Energy's
National Nuclear Security Administration under Contract DE-AC04-94AL85000.

Approved for public release; further distribution unlimited.

Issued by Sandia National Laboratories, operated for the United States Department of Energy by Sandia Corporation.

NOTICE: This report was prepared as an account of work sponsored by an agency of the United States Government. Neither the United States Government, nor any agency thereof, nor any of their employees, nor any of their contractors, subcontractors, or their employees, make any warranty, express or implied, or assume any legal liability or responsibility for the accuracy, completeness, or usefulness of any information, apparatus, product, or process disclosed, or represent that its use would not infringe privately owned rights. Reference herein to any specific commercial product, process, or service by trade name, trademark, manufacturer, or otherwise, does not necessarily constitute or imply its endorsement, recommendation, or favoring by the United States Government, any agency thereof, or any of their contractors or subcontractors. The views and opinions expressed herein do not necessarily state or reflect those of the United States Government, any agency thereof, or any of their contractors.

Printed in the United States of America. This report has been reproduced directly from the best available copy.

Available to DOE and DOE contractors from
U.S. Department of Energy
Office of Scientific and Technical Information
P.O. Box 62
Oak Ridge, TN 37831

Telephone: (865) 576-8401
Facsimile: (865) 576-5728
E-Mail: reports@adonis.osti.gov
Online ordering: http://www.osti.gov/bridge

Available to the public from
U.S. Department of Commerce
National Technical Information Service
5285 Port Royal Rd.
Springfield, VA 22161

Telephone: (800) 553-6847
Facsimile: (703) 605-6900
E-Mail: orders@ntis.fedworld.gov
Online order: http://www.ntis.gov/help/ordermethods.asp?loc=7-4-0#online

SAND2009-7605
Unlimited Release
Printed December 2009

Validation and Uncertainty Quantification of Fuego Simulations of Calorimeter Heating in a Wind-Driven Hydrocarbon Pool Fire

Anay Luketa
Fire and Aerosol Sciences Department

Vicente Romero and Martin Sherman
Validation and Uncertainty Quantification Department

Stefan Domino and David Glaze
Computational Thermal and Fluid Mechanics Department

Victor Figueroa
Transportation and Environmental Safety

Sandia National Laboratories
P.O. Box 5800
Albuquerque, New Mexico 87185-MS1135

Abstract

The objective of this work is to perform an uncertainty quantification (UQ) and model validation analysis of simulations of tests in the cross-wind test facility (XTF) at Sandia National Laboratories. In these tests, a calorimeter was subjected to a fire and the thermal response was measured via thermocouples. The UQ and validation analysis pertains to the experimental and predicted thermal response of the calorimeter. The calculations were performed using Sierra/Fuego/Syrinx/Calore, an Advanced Simulation and Computing (ASC) code capable of predicting object thermal response to a fire environment. Based on the validation results at eight diversely representative TC locations on the calorimeter the predicted calorimeter temperatures effectively bound the experimental temperatures. This post-validates Sandia's first integrated use of fire modeling with thermal response modeling and associated uncertainty estimates in an abnormal-thermal QMU analysis.

Acknowledgements

The authors would like to thank Jim Nakos for his discussion and interpretation of the experiments and Sheldon Tieszen for developing the computational meshes and original input file. We would also like to thank Alex Brown and Rich Hills for their review of this document.

CONTENTS

List of Figures

List of Tables

Nomenclature/Acronyms

ASC	Advanced Simulation and Computing Program, formerly Accelerated Strategic Computing Initiative
CALORE	ASCI developed thermal response simulation tool
DOM	Discrete Ordinates Method – a radiation solution technique
DTM	Discrete Transfer Method – a radiation solution technique
Fuego	ASC developed CFD fire simulation tool
LES	Large Eddy Simulation – a filtering technique
RANS	Reynolds Averaged Navier Stokes – a filtering technique
SIERRA	ASC developed computation infrastructure for multiphysics integration
SNL	Sandia National Laboratories
SYRINX	ASC developed participating media radiation simulation tool
TFNS	Temporally Filtered Navier Stokes – a temporal filtering technique
UQ	Uncertainty Quantification
V&V	Verification and Validation ASC program
XTF	Cross-wind Test Facility

1 Introduction

The objective of this work is to perform an uncertainty quantification (UQ) and model validation analysis of simulations of tests in the cross-wind test facility (XTF). The tests have been extensively documented elsewhere (Nakos, 2007). In these tests, a calorimeter was subjected to a fire and the thermal response was measured via thermocouples. The UQ analysis pertains to the experimental and predicted thermal response of the calorimeter. The calculations were performed using Sierra/Fuego/Syrinx/Calore, an Advanced Simulation and Computing (ASC) code capable of predicting object thermal response to a fire environment. A major focus of the ASC program is the development and application of verification and validation (V&V) along with uncertainty quantification practices. Demonstrating new advances in UQ and validation methodology, this work is in the same spirit as a previous study by Black, et al., 2007 in which uncertainties were characterized for the thermal response of a calorimeter in a fire, but in a calm wind condition. The following provides a description of the facility and experiments chosen for comparison, simulation specifications, the uncertainty quantification matrix, and the analysis results.

2 Description of Facility and Experiments for Comparison

The cross-wind test facility (XTF) shown in Figure 1(exterior) and Figure 2 (interior) was designed to provide a controlled environment with reproducible boundary conditions for a fire in a cross wind. It should be noted that direct one-to-one geometric representation of outdoor tests in a cross-wind in the XTF will not result in the same heat-flux loading on a system due to the pressure field, differences in air velocity profile and magnitude, and limitations on the pool size as discussed in Tieszen, et al, 2007.

The test chamber has a cross section of 25 ft wide by 25 ft high, with an effective length of 60 ft (Figure 2). The facility is designed to have uniform inlet airflow with a variance no larger than +/-1 mph at the final vertical screen which is located 5 ft upstream of the leading edge of the test chamber. XTF has a single outlet located above the access downstream doors. It is 20 ft wide by 7 ft high with the lower lip of the exhaust 18 ft above the floor. The overall length of the facility from the inlet screen to the exhaust is approximately 75 ft long.

For the entire cross-section, a maximum of nominally 5 mph of uniform airflow is possible. An area reduction section called an air bell can be mounted within the inlet to reduce the inlet area to 12 ft by 12 ft. With the air bell in place, the maximum uniform velocity in the inlet is nominally 20 mph. The air bell is mounted on the floor centered horizontally with 6.5 ft on each side. With the air bell in place, the remainder of the inlet is blocked off so that air only flows through the air bell. There is also an L-bracket mounted on the ceiling, blocking the top 7 ft of the final inlet screen to provide a stable recirculation zone near the ceiling corner. For this 18 by 25 ft open configuration, the maximum uniform airflow velocity is 8 ft/sec. The maximum pool fire diameter that can be tested in XTF is limited by the exhaust gas flow rate and temperature. The maximum corresponds to a 20 MW fire, which for JP8 is nominally 10 ft (3 m) in diameter.

Figure 1: External view Thermal Test Complex. XTF is the building in the lower left corner.

Figure 2: **Internal view of XTF showing the air inlet (far end)**

(a) **(b)**

Figure 3: a) Cone-shaped-shaped calorimeter inside flow-through enclosure with fuel pan in front. b) Front view of cone-shaped-shaped calorimeter and flow-through enclosure. Stands at sides of calorimeter hold thermocouples and (visible) flux gauges. Back end of XTF flow chamber is open (for loading) in this view, but for tests is closed and exhausts to outside.

The calorimeter thermal response from two experimental tests (#6 and #7) was chosen for comparison with simulation results since these were nearly repeat tests. Instrumentation consisted of thermocouples (TCs), heat flux gages (HFGs), pressure gages (PGs) and the wind velocity measuring system. For both tests, an 8' 10" (2.69 m) square and 20.25" deep, 0.5" thick mild steel pan containing JP-8 fuel was placed 20" from an enclosure containing the calorimeter as shown in Figures 3a and 3b. The enclosure, resting on a platform 28" tall, was a box 12' wide, 8' long, and 10'3" tall, with an 8' square centered inlet and an outlet of 42" wide by 67" tall. The enclosure was made of approximately 1/16" thick stainless steel with exterior surfaces of the walls and roof insulated to provide an easily modeled boundary condition for the model validation activity. Thus, an adiabatic boundary condition was modeled on the exterior of the enclosure walls and roof in the Fuego simulation. The enclosure serves the purpose of imitating foreseeable conditions where a fire heats up the walls and roof of a storage or transportation room or container. The walls and roof then radiate heat, imparting more heat and thus embodying a more severe heating condition than if no enclosure and only a shallowly engulfing fire (non-optically-thick) is present.

The calorimeter was centered within the enclosure and was comprised of a 1/8" thick 304 stainless steel shell filled with insulation as shown in Figure 3a to prevent convective and

radiative heat exchange among the inside walls of the cone for ease of modeling. Thus, the boundary condition on the interior of the cone-shell model in the Fuego simulations is modeled as adiabatic. Ninety two (92) TCs were installed on the inside surface of the calorimeter which were fastened by welding a ¼" wide by 3 mil thick nichrome straps at 45° increments around the calorimeter perimeter at 12 levels from the bottom to the top as shown in Figure 4. The angle designated as 0° directly faces toward the fuel pan and oncoming fire.

The steel interior walls, roof, and floor of the enclosure, and the exterior of the calorimeter, were painted with black Pyromark high-emissivity paint so that they would readily exchange radiative heat with the fire and with each other, therefore more quickly reaching steady-state temperature and re-radiation conditions. Concerning steady-state temperature and re-radiation conditions, the Pyromarked surfaces have an initial emissivity, ε, of nominally 0.86 upon application to the room-temperature steel surfaces, but the emissivity after experimental "burn-in" of the paint at high temperature is a significant unknown in the experiments. Later we describe how this important uncertainty is accounted for in the model validation analysis. The nearly adiabatic walls (with insulated back-sides) of the calorimeter and enclosure also strongly promote a quicker arrival to steady-state wall temperatures and re-radiation conditions in the experiments.

For both tests the air inflow was set at 150,000 cfm (1.7 m/s). The difference between test #6 and #7 was the presence of water within the pan. Test #6 had 11.3" of water with 6.7" of fuel floating on top of the water and a distance from fuel surface to pan lip of 2.25". Test #7 did not use water, but only fuel with a distance from fuel surface to pan lip similar to that of test #6. Thus, more fuel was used in Test #7. The approximate fuel regression rates measured for test #6 and #7 were 4.0 mm/min and 4.16 mm/min, respectively. Thus, the absence of water in test #7 provided a minor difference in the fuel regression rate.

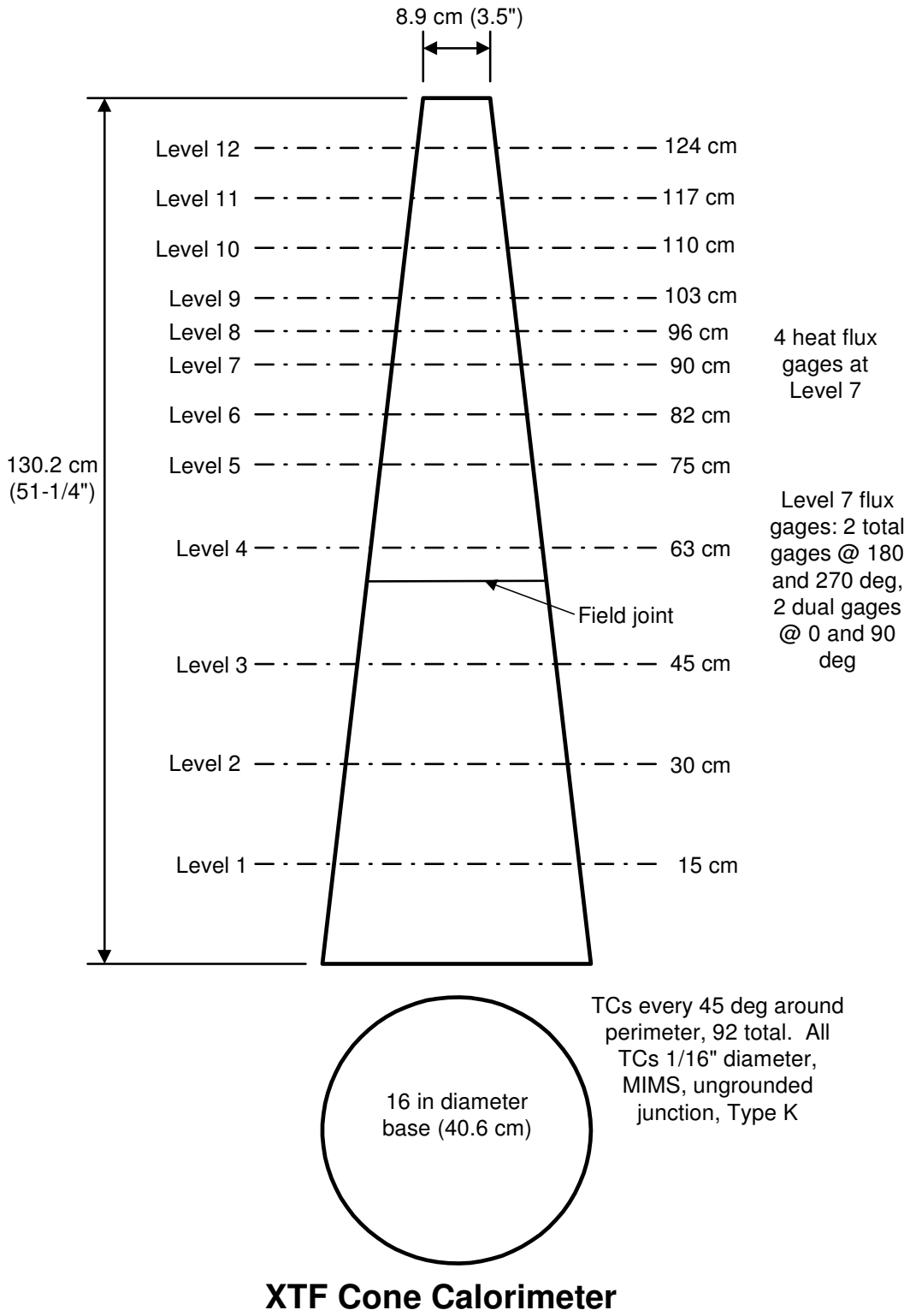

Figure 4: Cone-shaped Calorimeter TC Locations

3 Simulation Specifications

A total of eight simulations were performed each taking approximately 3 weeks of CPU time for a total of approximately 200 seconds of real time for each simulation. The medium mesh simulations were performed either on the Thunderbird or Redstorm cluster at Sandia National Laboratories using 256 processors. The coarse mesh was performed on the Rogue cluster using 200 processors. The fine mesh simulation requiring 2500 processors on Redstorm was not completed due to difficulties with the transfers that occur between Fuego and Calore. The following sections describe features of the computational suite, simulation parameters, geometry and mesh, and boundary conditions. The versions used to perform these calculations were 2.5.8 beta for Fuego, 4.5.5 beta for Calore, and 2.5.1 beta for Syrinx.

3.1 Computational Suite

Several computational codes, Sierra/Fuego/Syrinx/Calore (Moen, et al., 2002), were coupled to perform these calculations. These codes each have specific functions in order to simulate the thermal response of an object in a fire. Sierra provides a general framework for multi-physics coupling that allows Fuego, Syrinx and Calore to interact via volume and surface transfers for either one-way or two-way coupling. Fuego computes the fluids region, Syrinx computes the participating media radiation field and Calore the solid heat conduction regions. Fuego can simulate three-dimensional low Mach number turbulent reacting flows on heterogeneous topological meshes, e.g., a mixture of hexahedral, tetrahedral, pyramid, and wedge. An approximate projection algorithm is used with Control Volume Finite Element Method (CVFEM) discretization. SIERRA/Syrinx uses a discrete ordinates method assuming a grey non-scattering media in which radiative sources include soot as well as gases. Calore computes steady and unsteady conduction using the Galerkin Finite Element Method (FEM) for spatial semi-discretization and a finite difference discretization in time.

Two different turbulence models were tested for this study, both variations of the standard k-ε turbulence subgrid closure model (Jones and Launder, 1972) for the Reynolds Averaged Navier Stokes (RANS) equations. The standard k-ε turbulence model will perform very poorly in fires since this model does not produce enough turbulent shear production in the first half diameter of a fire. Strong turbulent mixing occurs in this region due to density gradients. Thus, a term has been added to the production of turbulent kinetic energy to capture the buoyant vorticity generation (BVG) (Nicolette, et al., 2005). The term has the form

$$G_B = \frac{0.35 m_t}{r^2} \left\| \vec{r} \cdot \vec{p} \right\|. \qquad \text{(Eq. 1)}$$

The term attempts to model the time-average effect of the roll-up of the large vortices that are characteristic of puffing fires as an additional turbulent kinetic energy production source term. The effects of both buoyant and shear production are contained in the eddy viscosity. The second variant allows the large vortices associated with puffing to be resolved on the grid. In order to avoid changing the filter from temporal (RANS) to spatial (LES) filtering, the Navier-Stokes

equations are temporally filtered (TFNS) and the closure model is a function of the filter width, Δ, (Tieszen, et al., 2005) and has the following form

$$\mu_t = c_\mu \rho k \Delta \qquad \text{(Eq. 2)}$$

This definition for the eddy viscosity is also used in the turbulent kinetic energy and dissipation equations and results in source terms that are proportional to the filter width, Δ, as opposed to the integral turbulence timescale, k/ε. Since the large scales are resolved, as opposed to modeled, Eq. 1 is not used with TFNS. Herein, the models tested will be referred to as the BVG model and TFNS model.

3.2 Simulation Parameters

All simulations were preformed with two-way coupling among Fuego, Syrinx, and Calore. The enclosure and calorimeter have two materials, stainless steel and insulation. Both materials in the enclosure and calorimeter are treated with temperature dependent properties (density, specific heat, conductivity). The insulation surrounding the enclosure and the inside of the calorimeter was given the thermal properties of calcinated kaolin. The steel comprising the enclosure and calorimeter was given the thermal properties of stainless steel 304. All regions were initialized with a uniform temperature of 298K and pressure of 0.84 atm. The fluid region was initialized with the values in Table 1.

Table 1: Initial values for fluid region

u-velocity (downstream velocity)	1.7 m/s
v-velocity (cross stream velocity)	0 m/s
z-velocity (vertical velocity)	0 m/s
Pressure above atmospheric	0 N/m^2
turbulent kinetic energy*	0.011 m^2/s^2
turbulent dissipation*	0.0185 m^2/s^3

* corresponds to 5% turbulent intensity and length scale of 0.01 m for eddies

The fuel used was iso-octane instead of JP8 since that is the heaviest hydrocarbon fuel available in the Fuego properties library at the time these simulations were performed. Iso-ocatane has the following properties as shown in Table 2.

Table 2: Properties of JP-8

Molecular formula	C8H18
Molecular weight	114 kg/kmol
Liquid fuel density	688 kg/m^3
Vapor mid-boiling point	485 K
Vapor density at 485 K and 0.84 atm.	2.41 kg/m^3

A fixed time step of 0.002 s was used for all simulations using the TFNS model, with a time filter of 0.008 s. This time step provided a CFL number of approximately 1.5. Simulations using the BVG model had variable time steps restricted by a CFL number of 2. Two non-linear

iterations were taken for the energy equation, while for all other equations one non-linear iteration was taken. The quadrature order (QO) used for all simulations was 4. From the study by Black, et al., 2007 it was shown that this QO order is sufficient for tracking the near radiation field. The projection scheme used was "fourth order smoothing with timestep scaling." The linear equation residual norm tolerance was set to 1.E-04 for the continuity equation and 1.E-03 for the scalar and momentum equations. A MUSCL upwind scheme with Van Leer limiting was used. The first order upwind factor was set to 0.2 for all fluid equations except k and epsilon.

3.3 Geometry and Mesh

The geometry used for all simulations is shown in Figure 5a. The enclosure and calorimeter are treated as two-way participating conduction regions with the fluid and participating media radiation regions. Three-dimensional, transient heat conduction is being solved in the enclosure and in the calorimeter. The mesh generation software, Cubit, was used to create meshes for three different levels of refinement to determine sensitivity to mesh size. The simulations for the model validation assessment to follow used the medium sized mesh. The number of hexahedral elements used for each mesh is provided in Table 3. Nodes were clustered in areas of importance as indicated in Figure 5b which shows the mesh along the centerline and enclosure entrance/exit. There is a high mesh density in the region above the pool, around the calorimeter, and into the enclosure. The outlined cone shape within the enclosure is the calorimeter as shown in Figure 5b.

Table 3: Number of hexahedral elements for each mesh

Region	**Mesh**		
	coarse	**medium**	**fine**
Fluids and participating media radiation regions	608 K	1.25 M	10 M
Enclosure	19 K	493 K	3.8 M
Calorimeter	74 K	525 K	4.7 M

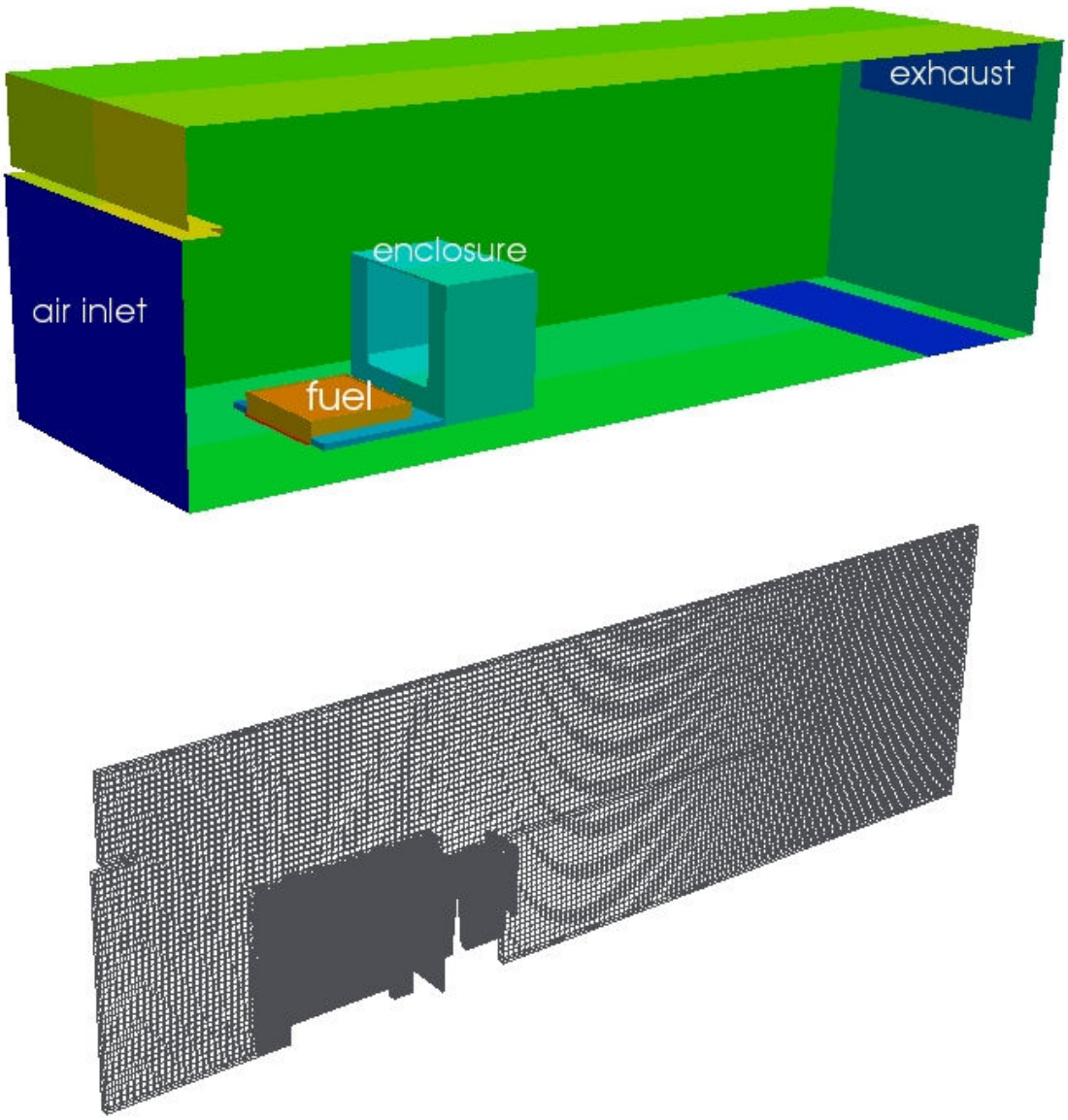

Figure 5: (a) XTF Geometry, (b) Centerline Medium Mesh

3.4 Boundary Conditions

All simulations used the same boundary conditions except for the emissivity value of the enclosure which will be described in section 4. Within the Syrinx region all walls were assigned a gray diffuse boundary condition with an emissivity of 0.86 and transmissivity of 0, while the fuel surface had an emissivity value of 1 and transmissivity of 0. The boundary conditions used in Fuego for the inlet, outlet, fuel, XTF walls are listed in Table 4. The boundary conditions used in Calore for the calorimeter and enclosure surfaces are provided in Table 5.

Table 4: Boundary Conditions used in Fuego region

Surface	**Boundary Type**	**Specifications**
XTF air inlet	Inflow	X_velocity = 1.7 m/s Y_velocity = 0 m/s X_velocity = 0 m/s Turbulent kinetic energy* = 0.011 m^2/s^2 Turbulent dissipation* = 0.0185 m^2/s^3 Temperature = 298 K *assumes turbulent length scale of 0.01m
XTF wall and floor	Wall	Adiabatic Wall friction factor = 9.8 Equilibrium production model
Enclosure and calorimeter	Wall	Interface boundary (with Calore) Wall friction factor = 9.8 Equilibrium production model
XTF outflow	Open Boundary	Pressure = 0.0 Turbulent kinetic energy = 1.0e-6 m^2/s^2 Turbulent dissipation = 1.0e-6 m^2/s^3 Temperature = 298 K
Fuel	Inflow	X_velocity = 0 m/s Y_velocity = 0 m/s Z_velocity* = 0.0224 m/s Turbulent kinetic energy** = 7.1e-5 m2/s2 Turbulent dissipation**= 1.0e-6 Temperature = 485 K *Determined by using a fuel regression rate of 4.08 mm/mm from averaging data from tests #6 and #7 as well as fuel liquid and vapor densities at 485 K **assumes turbulent length scale of 0.1 m

Table 5: Boundary Conditions used in Calore region

Surface	Boundary Type	Specifications
Calorimeter*		
Side surface	Radiative Flux	Emissivity** = 0.86 Temperature = 298 K Initial value = 418 kW/m^2
Side surface	Convective Flux	Initial convective coefficient = 0 Initial temperature = 298 K
Bottom surface	Heat flux	Flux = 0 kW/m^2
Enclosure*		
Inner right and left walls	Radiative flux	Emissivity** = 0.86 Temperature = 298 K Initial value = 418 kW/m^2
Inner right and left walls	Convective Flux	Initial convective coefficient = 0 Initial temperature = 298 K

*All other surfaces are adiabatic
**Nominal case

4 Methodology and Procedures Applied for Uncertainty Quantification and Model Validation

4.1 Initial Model Validation Considerations

Although a wealth of experimental data from the tests is available to compare against FUEGO predictions for model validation purposes, time and resource considerations dictated that comparisons in the project be confined to only calorimeter temperature response. Such response is most directly associated with the validation question driving the experimental and simulation work here: how well does FUEGO calculate surface heating conditions on objects in wind-driven hydrocarbon fires?

To bring the scope of the validation activity into line with project resources, the validation comparisons are further limited to eight diverse and representative TC locations on the calorimeter. Figure 6 shows four comparison locations (at 0˚, 90˚, 180˚, and 270˚) on the upper section of the cone above a field joint (internal bolted attachment) at mid-height, and another four at the same angular positions on the lower section of the cone below the attachment joint.

On the upper section of the cone, the Level 10 set of TCs in Figure 6 was chosen in order to minimize local edge or anomaly effects on conduction behavior and therefore temperature of the calorimeter shell. Level 10 is about half way between the top edge of the cone and the height discernable in Fig. 6 where flux gauges inserted into holes of 1.5 to 2 inch diameter in the shell create local anomalies in the conduction and temperature fields. On the lower section of the cone, unknown and possibly highly varying contact resistance around the bolted attachments at the mid-height field joint and the base of the cone could produce local effects on calorimeter temperature. The Level 2 height in Figure 6 was chosen in order to minimize local effects due to these bolted joints.

Calorimeter temperature response is not the only quantity relevant to FUEGO validation. For example, enclosure temperature response is just as indicative of how well FUEGO calculates object surface heating. Certainly, it would be significantly more revealing to compare FUEGO predictions against experimental response for both the calorimeter and enclosure, instead of just one or the other. Both are time-space integrating sensors of the experimental and simulated fires, and corroboration (validation) based on two diverse such sensors are of course stronger than corroboration from one alone. However, corroboration based on two diverse integrating sensors also cannot be said to be *absolutely sufficient* to settle the model validation question with regard to the present experiments. For instance, a further check against the TCs and flux gauges on the stand in the flow field of the fire (see Figure 1) could indicate differently, and refute the fire model's predictive capability locally there. (Such further checks are essentially infinitely prescribable—see discussion in Romero, 2007a on "field validation" versus the validation of only certain *resultant effects* of the field important to an engineering purpose, "effect validation".)

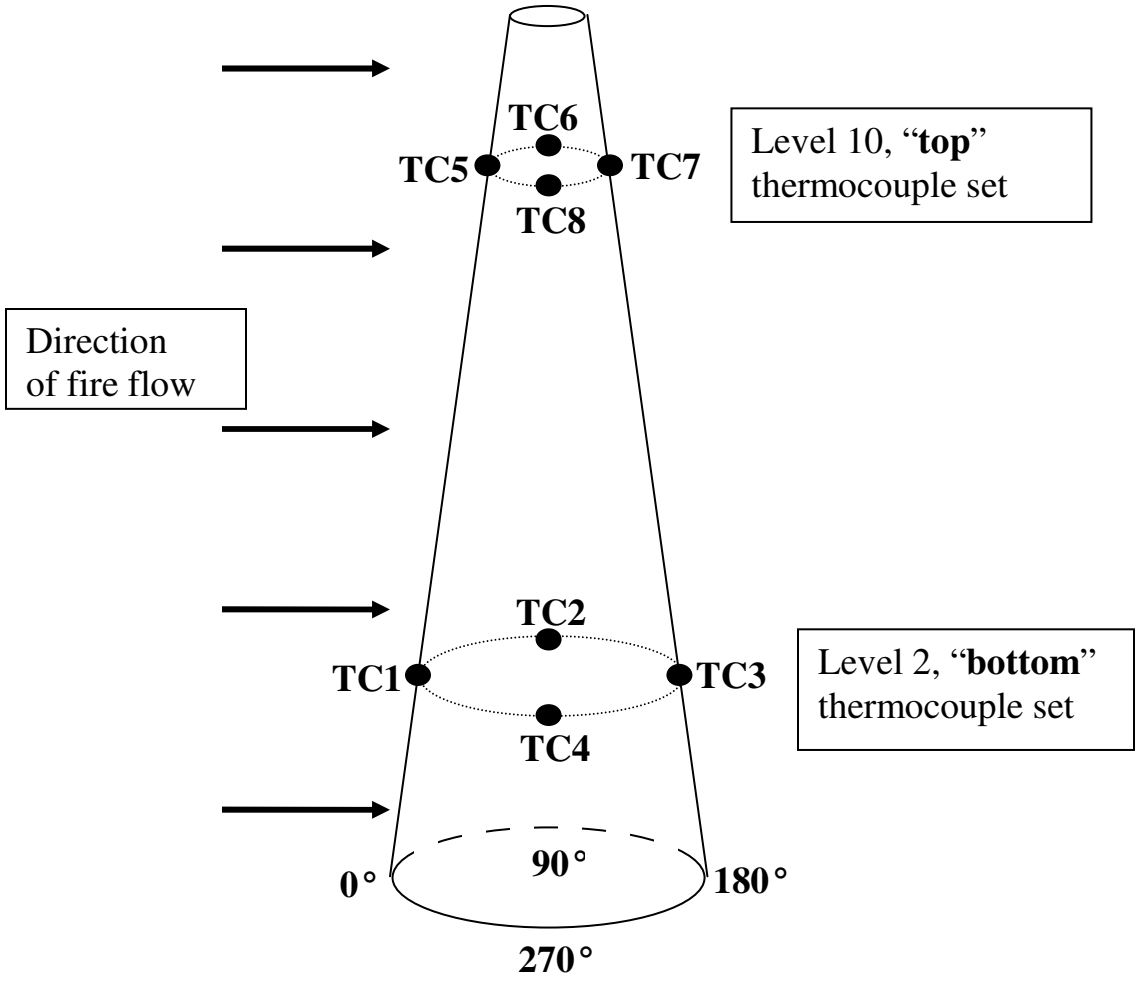

Figure 6: Thermocouple comparison locations for experimental results versus Fuego predicted results.

In fact, absolute sufficiency is probably only reachable in theoretical limits and it would appear that statistical procedures and arguments would have to be invoked to establish validation sufficiency in practical terms (e.g., odds or significance level associated with a validation conclusion). This is beyond the scope of the present treatment. In the present circumstances we can only address whether a *necessary* test of model adequacy is met by FUEGO with respect to the narrow program-relevant quantity of calorimeter steady-state temperature. Indeed, it is shown in the following that a significant validation test is passed in this regard, lending credibility to FUEGO's predictive abilities in the present experimental circumstances, although not sufficient to absolutely confirm its predictive capability—even for the present experimental conditions.

A substantial relaxation in the strength of the validation case also comes from the fact that we compare only steady-state temperature of the calorimeter, as opposed to transient temperature response. This is forced by several reasons. First, capabilities for realistic modeling of transient startup and growth of the pool fire were not yet available in FUEGO. Second, the predominant project driver, assessment of safety risk in fires, is concerned with internal response events that

take 10's of minutes to develop and are the result of sustained fire heating and are fairly insensitive to the early-time initial flare-up and stabilization transients of the fire.

Thus, although transient response is a more stringent test of FUEGO predictive capability, project constraints dictated that we could only reasonably compare steady-state temperatures, and this was felt to be acceptable with respect to the driving purpose of predicting heating response simulations for risk analysis.

4.2 Plan of Fuego Simulations for Uncertainty Quantification in the Model Validation Procedure

FUEGO simulations were used in the validation procedure to quantify modeling uncertainty. Resource constraints dictated that only 5 or 6 steady-state FUEGO simulations could be run at the medium-resolution model described in section 3.3. (Each simulation took several weeks on 256 processors.)

Here model resolution involves spatial-discretization cell size; number of discrete-ordinate directions for solution of participating-media radiation transport; and solver numerical-error tolerance parameters employed in the steady-state FUEGO computations. The resolution level was surmised from past FUEGO modeling projects to be sufficient for the validation purpose here, i.e., to yield simulation results that would change with further resolution refinement only relatively little compared to the effects of other physical modeling uncertainties and bias errors in the validation activity.

Previous work (Black, et al., 2007) simulating a pool fire of similar length and time scales as these simulations demonstrated that the mesh resolution used for the current work is sufficiently resolved, though this cannot be completely substantiated without performing a finer mesh simulation. Nonetheless, it is explained later how the validation framework used in this paper would handle any characterized uncertainty (e.g. by methods presented in Roache, 1998) due to numerical resolution in the model and simulations.

Regarding fire-physics modeling uncertainty, a consensus of Sandia fire modeling expert judgment concludes that the following physics submodel forms and coefficients were generically the largest sources of *intrinsic*[1] modeling uncertainty. The nominal values and associated uncertainties are listed in Table 6.

[1] This term signifies a category of modeling uncertainty that is innately associated with the "traveling" portion of the model being validated. Only the traveling portion goes on to new predictions beyond the validation exercise. That is, certain elements or aspects of the model will be carried forward ("travel") to new predictions, and certain aspects are specific only to the validation setting. The intrinsic uncertainties in Table 1 all exist in the validation setting, but also travel to new predictions, as uncertainties that are propagated to simulations results in the new prediction settings as well. Other uncertainties in the experiment, such as emissivity of the calorimeter and enclosure walls in the modeled experiment, are confined to the validation experiments; in general we will simulate new environments and enclosures with different emissive properties and uncertainties than the specially prepared Pyromark painted surfaces in the validation experiments. Thus, these emissivity uncertainties will not travel to new predictions—they are not intrinsic to the FUEGO fire dynamics model. As explained in Romero, 2009 and demonstrated in this report, the validation framework handles traveling uncertainties differently from non-traveling uncertainties.

Table 6. Intrinsic Sources of Uncertainty in the Fire Dynamics Model

Parameter	Range of Values
heat of combustion (HOC)	44.66kJ/mol ± 10%
soot extinction coefficient (SEC)	7 ± 10%
convection coefficient (CC) at object surface	calculated value -50% to +100%
flame volume coefficient: (FVC):	2.13 ± 30%
flame loading coefficient: (FLC)	0.41 ± 30%
turbulence model form	TFNS (nominal) versus BVG

To estimate the modeling uncertainty contributed by the above 6 factors, using only the budget of 5 or 6 steady-state FUEGO simulations that could be afforded, information from previous uncertainty/sensitivity studies over these modeling factors was drawn from. The plan was to get reasonable upper and lower bounds on the FUEGO predicted heating of the calorimeter by running a simulation at the combination of parameter values within the preceding parameter space (joint "uncertainty space") that gives the highest heating to the calorimeter, and then at a combination of parameter values within the uncertainty space that gives the lowest heating to the calorimeter.

The sought parameter combinations were identified to the best possible extent under all the presiding constraints and available information as follows. Romero, et al., 2003, presents a blocked experimental design of 16 simulations that explore the above six-factor uncertainty space plus spatial discretization and computational solver resolution effects. Sixteen simulations were run for "Airplane Fire" and sixteen more for "Truck Fire" wind-driven fires. The sensitivity of heating to the six uncertainties was analyzed. A summary of the findings is presented in the archived memo (Romero, et al., 2004). From the sensitivity results, the parameter combinations for high and low heating[2] in each scenario were inferred.

The parameter-set for high heating was effectively the same (consistent) for the Airplane Fire and Truck Fire scenarios, and is listed below for upper-bound predicted heating in the XTF experiment. The parameter-set for low heating was also reasonably consistent between scenarios, except for the value of the Flame Volume Coefficient (FVC). In the Truck Fire scenario, lower heating was associated with the high level of FVC (nominal + 30%), but for the Airplane Fire scenario, lower heating was associated with the low level of FVC (nominal - 30%). Hence, in Romero, et al., 2004, which was written to prescribe bounding parameter sets for high and low heating in a different accident scenario (Case 13 in Black, 2004), specified that simulations should be run at both low and high levels of FVC, with all other parameter values being set as listed below to give lower-bound heating. The ensuing two simulations determined that the low level of FVC yielded the lowest heating in the Case 13 accident scenario. Since this scenario (inside an enclosure with fire flowing through) is fairly close to the XTF fire experiment conditions, we take those findings as the final word. Thus, FVC is set at its low level in the following for the parameter combination corresponding to lower-bound predicted heating in the XTF experiments.

[2] as a global spatial average over the heated object, but not necessarily locally at all points on its surface

The investigation in Romero, et al., 2004, employed a standard k-epsilon turbulence model and alternatively a Buoyant Vorticity Generation (BVG) turbulence model to bound model-form effects of turbulence modeling error in the Reynolds-Averaged Navier-Stokes (RANS) computational fluid dynamics (CFD) model. The investigations in Black, et al., 2007 and in our validation exercise propose CFD model-form bounds as the BVG RANS formulation and a Time-Filtered Navier-Stokes (TFNS) RANS formulation.

The formulations generally dictate that the BVG-RANS turbulence model has the potential to result in larger and hotter simulated fires than the TFNS-RANS turbulence model due to the inclusion of a baroclinic torque source-term in the k-equation which enhances mixing and therefore combustion in the BVG formulation. Hence, for model validation purposes we could minimally run just one FUEGO simulation with the BVG model and the inferred "hot fire" extreme combination of values of the other uncertain parameters (Set 4 prescribed below); and another simulation with the TFNS model and the inferred "cool fire" extreme combination of other parameter values (Set 3 prescribed below). A third simulation would be run (analogous to Simulation 6 discussed later) to account for the effects of the highly uncertain emissivity of the Pyromarked surface of the calorimeter and enclosure.

Nevertheless, to more thoroughly examine the effect of turbulence model form on predicted heating in the current physical setting, we ran both model forms with the "hot fire" and "cold fire" extreme parameter combinations listed in the first five bullets of Table 6. Thus, the following simulations were run. Table 7 summarizes the run matrix. Values of the other inputs to the simulations did not change over the runs and are listed in Sections 3.2 - 3.5.

Set 1 (Simulation 1) – Baseline Case, TFNS with nominal parameter values in Table 1

Set 2 (Simulation 2) – High Heating parameter combination with TFNS

Set 3 (Simulation 3) – Low Heating parameter combination with TFNS

Set 4 (Simulation 4) – same as High Set #2 above, except with **BVG** turbulence model

Set 5 (Simulation 5) – same as Low Set #3 above, except with **BVG** turbulence model

Set 6 (Simulation 6) – Same as Set 2, except $\epsilon = 0.96$

Table 7. Fire Model Input Variations for the Six FUEGO Simulations Run

FUEGO run	turbul. model	HOC	SEC	CC	FVC	FLC	ε_Pyromark
Set 1	TFNS	44.66	7	100%	2.13	0.41	0.86
Set 2	TFNS	44.66+10%	7	100%	2.13	0.41 -30%	0.86
Set 3	TFNS	44.66-10%	5	200%	2.13 -30%	0.41 +30%	0.86
Set 4	BVG	[……same as row 2……]					
Set 5	BVG	[……same as row 3……]					
Set 6	[……same as row 2……]						0.96

The uncertainties of other inputs to the validation experiment(s), that are non-intrinsic to the traveling fire dynamics model, such as calorimeter/enclosure/facility geometry, fuel regression rate, air flow rate (wind velocity), and material properties, must also be considered in the model validation procedure. Of the parameters in this non-traveling category, it was surmised that the only uncertainty of first-order significance impacting calorimeter steady-state temperature was emissivity of the calorimeter exterior and of the enclosure interior.

This emissivity uncertainty is accounted for by running a simulation (#6, below) to quantify the effect of a substantial perturbation from the nominal emissivity $\epsilon_{nominal} = 0.86$, with all other model inputs held constant. From this, a first-order finite-difference approximation to the derivative for change in local steady-state temperature at the cone surface with respect to change in surface emissivity, $dT/d\epsilon$, can be formed. Then the linearized relationship $\Delta T \approx [dT/d\epsilon] \bullet (\Delta\epsilon)$ can be used to estimate the steady-state temperature change at a given location on the calorimeter surface for any value of emissivity ϵ different from $\epsilon_{nominal}$.[3] Hence, the local ΔT effect from varying ϵ over its applicable uncertainty range can be investigated analytically with the above relation, where $\Delta\epsilon = \epsilon - \epsilon_{nominal}$. This will be applied later.

The uncertainty range for emissivity of the calorimeter exterior surface and the enclosure interior surfaces (walls, roof, and floor) is taken to be 0.76 to 0.96 based on measured values (Figueroa, 2005; Nakos, et al., 2004; Mehling, et al., 1998; Worner, 1998; Siegel and Howell, 2002) for both heavily oxidized steel surfaces and burned-in Pyromarked steel surfaces like in the present XTF experiments. Whether heavily oxidized (burned-in) steel, or burned-in Pyromarked steel, the corresponding emissivity is thought to lie within the range cited above. Set 6 employs an emissivity perturbation that goes to the high extreme of the emissivity uncertainty range, 0.96.

A less significant but still substantial non-traveling uncertainty in this project is the heat transfer between the bottom of the steel cone and the thermally massive steel floor it was bolted to. Unfortunately, in this project it was not practical to parameterize a contact conductance at this interface into the FUEGO simulations. Instead, a simple adiabatic boundary condition was applied at the bottom of the cone. The consequent error (and uncertainty thereof) remains unquantified in the present effort. Nevertheless, strong arguments are made in Section 4.3.5 that neglecting this factor probably does not change the final validation conclusions.

Geometry uncertainties may also have been possibly significant, but were judged most likely to be of second-order importance (if at all) on calculated steady-state temperatures. Finally, the uncertainties associated with fuel regression rate, air flow rate, and steel and insulation thermal properties of the calorimeter were judged to have relatively little effect on calculated steady-state temperatures, based on applicable sensitivity studies from Black, et al., 2007.

[3] For certain reasons not evident in what is presented in this report, Sim. 6 is a perturbation from parameter set #2. In what follows, the assumption is made that the derivative $dT/d\epsilon$ would be approximately the same for a similar emissivity perturbation from *any* of the simulations # 1 – 5. Although the derivative might actually change non-negligibly if computed by perturbations from the other simulations, this sensitivity was not investigated.

4.3 Experiment and Simulation Results and Uncertainty Processing for Model Validation Comparisons

The transient temperature responses at the eight thermocouple (TC) locations in Fig. 6 are shown in Figures 7 and 8 for experiments 6 and 7.

4.3.1 Presentation of Raw Experimental Results

The temperature rise at all TC locations is very rapid after the fire starts and is blown through the calorimeter-containing enclosure. Nonetheless, the times at which the TC locations reach effective steady-state temperatures can differ by 10 minutes or more. For instance, in Exper. 6 (Fig. 7), TC 3 at the back side of the calorimeter (bottom TC at 180˚ in Fig. 6) doesn't reach effective steady-state temperature until about 20 minutes after inception of the fire. TC 7, on the other hand, reaches effective steady-state temperature in about 10 minutes, even though it is also at the back side of the calorimeter—but much closer to the top. This 10-minute time difference is consistent with other pretest experimental results cited in the next paragraph. In experiment 7 (Fig. 8), TC 3 takes about 30 minutes to reach an effective steady state, while TC 7 again only takes about 10 minutes. The vastly different times to TC 3 steady states in experiments 6 and 7, but reasonably close terminal values within 30K in the two experiments, suggests that the fires in the two experiments eventually stabilized to closely similar states, but appear to have stabilized at considerably different times.

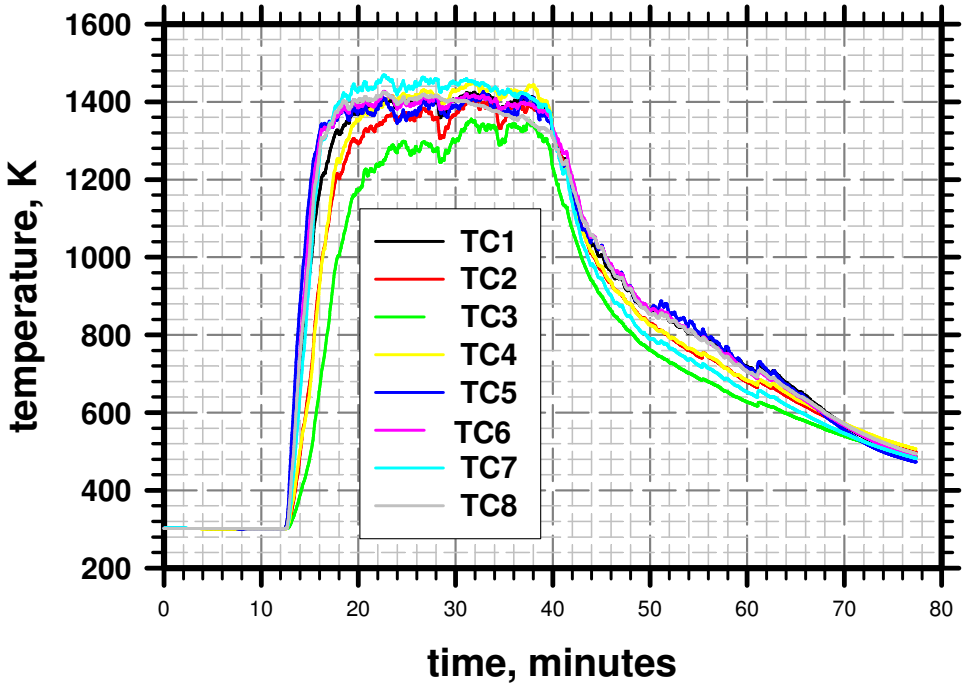

Figure 7:Experimental TC responses for Experiment # 6

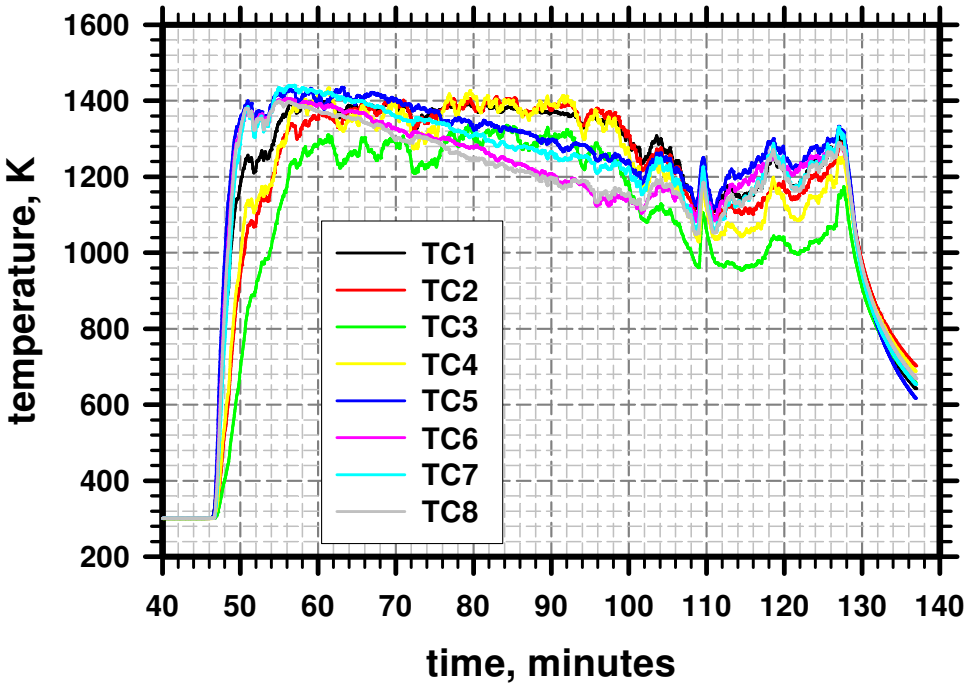

Figure 8: **Experimental TC responses for Experiment # 7**

The presumption here is that the calorimeter heat transfer properties remained nearly the same between the two experiments, such that the response stabilization time for calorimeter shell temperature is similar in the two experiments. A 1-D Heizler chart analysis indicates that the transit time is less than a minute for a change in heat applied to the outside of the calorimeter shell to fully register at the inside surface of the 3/16-inch thick steel shell, where the TCs are mounted. However, the issue of response time is complicated for the lower set of TCs 1 – 4 by the question of whether significant heat transfer coupling exists to the thermally massive steel plate that the calorimeter base is bolted to. Pretest data in Nakos, 2007 for TC Levels 1, 2, and 3 in Fig. 4 of the report shows that at steady-state conditions (effectively stable TC temperatures everywhere on the cone for ~10 minutes or so), Level 3 is up to a few 10s of degrees hotter than Level 2, which is itself up to a few 10s of degrees hotter than Level 1 nearest the base. The temperature gradient implies substantial heat flow down the cone shell to the steel plate that the cone base is bolted to. Thus, significant thermal coupling between cone and plate does appear to exist. Indeed the data indicates that the TC temperatures at these bottom 3 levels take about 10 minutes longer to level out than for the TCs on the top section of the cone. The implication is that 10 minutes is the effective time-period for heat-soaking the thermally massive steel plate, after which the TCs at Levels 1, 2, and 3 assume their ultimate steady-state temperature levels. In any case, since there is no reason to suspect that calorimeter heat transfer properties changed significantly between Experiments 6 and 7, the very different stabilization times for TC 3 in the two experiments is assumed to be caused by different fire development times in the two experiments.

Another observation about the data is that in experiment 7 several of the hottest TCs (highest levels on the cone, Levels 10 - 12) are diagnosed to have partially failed by shunting (see Nakos,

2007). This caused their temperature readings to decline artificially as seen for the Level-10 TCs 5 - 8 in Fig. 8.

4.3.2 Discussion of FUEGO Simulations and Raw Simulation Results

Figures B1 - B6 in Appendix B show the FUEGO results at the eight TC locations, for the six FUEGO runs identified in Table 7. The results in the figures are most revealing when grouped by thermocouple location and then plotted against the experimental data, as shown in Appendix C and discussed below. However, a few comments on Figs. B1 – B6 are in order. Note that only the late-time portion of Sim. 1 (Fig. B1) and Sim. 5 (Fig. B5) were saved for plotting. Also note that results for Simulation 5 are falling rather than rising to a steady state because a mistake in one of the parameter values was noticed and corrected mid-way through the calculation. Furthermore, Figs. B1, B3, and B5 show that the temperature results of Sims. 1, 3, and 5 have not yet completely stabilized to a [noisy] steady-state plateau, like for the other simulations. The simulations could not be run any further due to time limitations in the project. (Each simulation took several weeks on 256 processors.) Consequently, results are visually extrapolated to estimated steady-state values as discussed below. Finally, the FUEGO runs were false-transient simulations to reach steady-state temperatures as quickly as possible. Therefore, the transient times are intentionally not accurate but result from assumptions to increase efficiency. The simulations results are plotted on a scale of seconds to reach steady state. Note the different abscissa time-scale labels present in figures where simulation results are plotted in the same graph with experimental responses—the latter reaching steady state on a scale of minutes and being plotted against abscissa labels of minutes.

4.3.3 Characterization of Raw Experimental and Simulation Results for TC5 as a Representative Case

Here we focus on TC5 as a representative case to illustrate uncertainty and validation considerations, methodology, and procedures that apply in this particular model validation activity. Matters are similar for the other seven TCs. Results for all TCs reside in the appendices and are pointed to in the following discussion. All results are summarized and considered in Sections 5 and 6 of the report.

TC5 is about 1/5th of the way down from the top of the calorimeter, and facing the oncoming wind-driven fire. Figure 9 shows experimental and predicted temperature response curves for TC5. Such figures for all eight TCs are found in Appendix C.

As discussed previously, the data from experiments #6 and #7 are considered to be from two nominal repeat experiments. As described in Nakos, 2007 the five preceding experiments were partial trial experiments needed to refine the geometry configuration and experimental conditions, and to “burn in” the Pyromark-painted radiating surfaces.

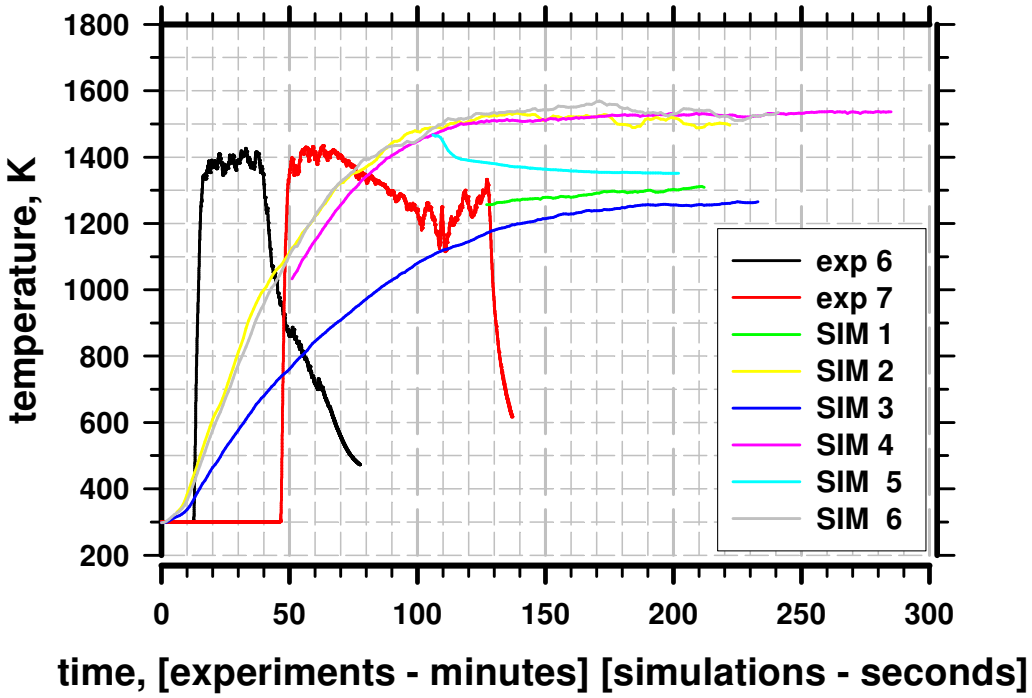

Figure 9: Calorimeter Temperature at TC #5, top - 0 facing the fire

Experimental Results: For the experimental results in Figure 9 it is obvious that it is important to use appropriate time windows over which to average TC5 temperature responses in order to get representative steady-state values for model validation comparisons. The time windows used are depicted graphically in Figure 10. These correspond to a six-minute window from 32 - 38 minutes in Exp. 6 and a 13-minute window from 54 – 67 minutes in Exp. 7. For reference, the averaging time-windows for all eight TCs are presented in Table A and are depicted in the odd-numbered figures in Appendix D, which are analogous to Fig. 10 here.

Table 8. Time windows for time-averaging of experimental TC readings into representative steady-state temperatures.

	experiment 6	experiment 7
TC 1	32 - 38 min	60 - 80 min
TC 2	32 - 38 min	70 - 90 min
TC 3	32 - 38 min	80 - 90 min
TC 4	32 - 38 min	80 - 90 min
TC 5	32 - 38 min	54 - 67 min
TC 6	32 - 38 min	55 - 56 min
TC 7	20 - 30 min	55 - 56 min
TC 8	20 - 30 min	55 - 56 min

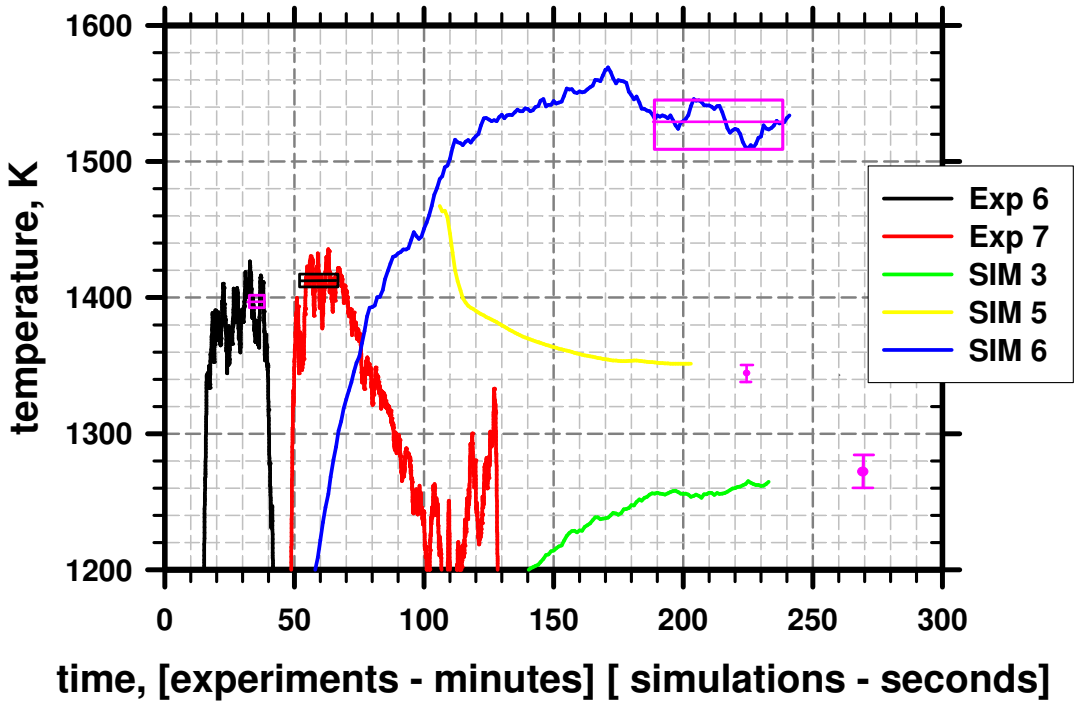

Figure 10: Uncertainty on steady-state experimental and simulation results at TC 5.

The time-window boxes in Figure 10 (and analogous figures in Appendix D) have a middle horizontal line that represents the arithmetic mean of the data within the time window, where readings were recorded at 1-second intervals. The means for TC5 are listed in Table 9. Experimental means for all TCs are highlighted in Table E.1 (Appendix E). The upper and lower horizontal lines that define the top/bottom of the time boxes are given respectively by the mean +/– 5K. The rationale is that other time-windows than those employed here, with different width and/or shifted later or sooner in time, could be just as appropriate or representative. A few such physically-reasonable perturbations were examined (see Romero et al., 2009). These resulted in changes in time-window means of a few degrees K or less. Accordingly, a deemed-reasonable uncertainty band of +/– 5K was assigned to the mean temperatures (representative experimental steady-state point values) in Table 9.

As additional information for later use, Table 9 also lists maximum and minimum *instantaneous* temperatures over the time windows, but these should not be mistaken to represent reasonable uncertainty bounds on the steady-state *means* over the time windows. Analogous results for all TCs are listed in Table E.1 (Appendix E).

Table 9. Mean, Max., and Min. Temperatures over Time Windows in Figure 10

	Time-window mean, μ	Maximum over time-window	Minimum over time-window
Exper. 6	1394 K or 1121℃	μ6 + 33 K or ℃	μ6 - 31 K or ℃
Exper. 7	1412 K or 1139℃	μ7 + 24 K or ℃	μ7 - 34 K or ℃

Simulation Results: For the simulation results, representative steady-state values are actually *less* definite than experimental values in many instances. In particular, Figures 9 shows that the temperature results corresponding to Simulations 1, 3, and 5 have not yet stabilized sufficiently. Consequently, results were here visually extrapolated to estimated steady-state values. (See Romero et al., 2009, for a more quantitative approach to the steady-state characterization. In any event, no change occurs to the validation conclusions found in this report.) The procedure involved visually extrapolating a TC curve to form reasonable uncertainty bands of plausible upper and lower bounds on the asymptotic steady-state value, and then taking the midpoint of the bounds as the single most representative point-estimate for steady-state temperature. For example, for Sim. 3 it is visually judged that the steady-state asymptote of the temperature curve is within an uncertainty bar plotted in Fig. 11 that runs from 5K below the last plotted temperature from the simulation, to 20K above the last plotted temperature. This information is recorded in Table 10. These values of -5K and +20K are added to Sim. 3's last plotted temperature in Table 11 to get the min. and max. values listed for Sim. 3 in Table 11. The min. and max. values correspond to the lower and upper extents of Sim. 3's uncertainty bar shown in Fig. 11. The depicted midpoint of the uncertainty bar for Sim. 3 coincides with the 'midway' temperature listed for Sim. 3 in Table 11.

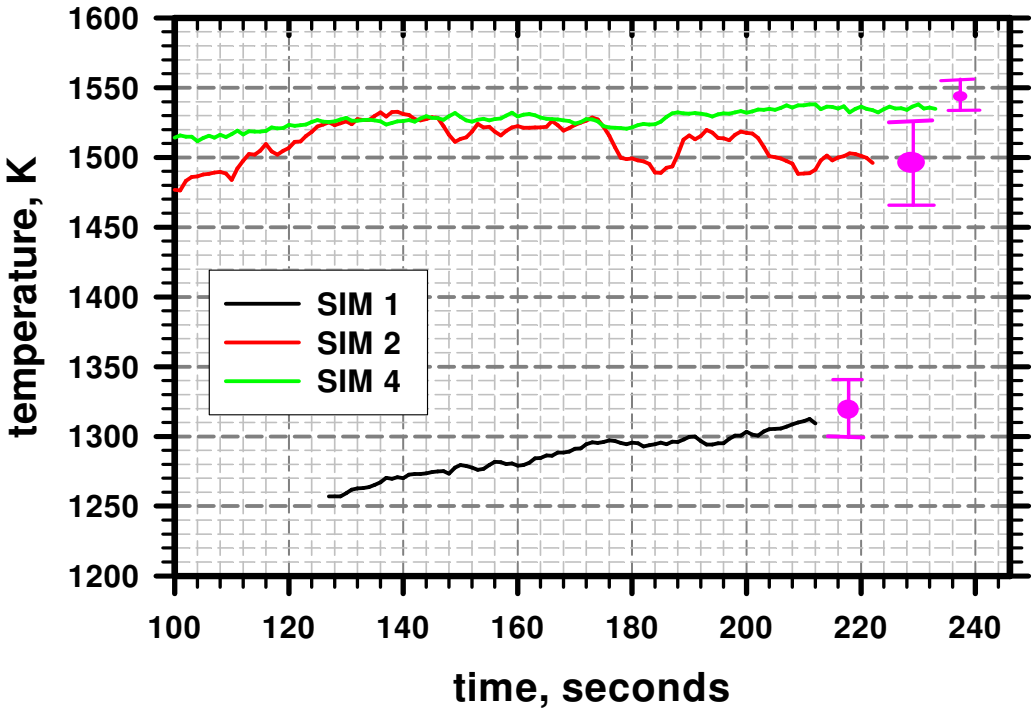

Figure 11: Uncertainty on steady-state simulation results at TC 5.

Table 10. Values in brackets [] are visually projected limits to anticipated change from end-of-simulation temperatures to asymptotic steady-state values. For Simulation 6 the averaging time-window is listed from which a mean estimate for steady-state temperature is determined.

Sim. 1	Sim. 2	Sim. 3	Sim. 4	Sim. 5	Sim. 6
[-10,+30] K	[-30,+30] K	[-5,+20] K	[-5,+20] K	[-15,0] K	190 - 241 sec

Table 11. End-of-simulation temperatures at TC5 location, with mean or extrapolated-asymptotic steady-state values and uncertainty bounds

FUEGO run	ending T (K)	Max. (K)	Min. (K)	Central estimate (K)
Sim. 1	1309	1339	1299	1319 (midway)
Sim. 2	1496	1526	1466	1496 (midway)
Sim. 3	1265	1285	1260	1273 (midway)
Sim. 4	1537	1557	1532	1545 (midway)
Sim. 5	1352	1352	1337	1345 (midway)
Sim. 6	1534	1546	1510	1529 (mean)

For Simulations 2, 4, and 6, temperature results did plateau to quasi-steady values before the simulations were terminated. Considering Sim. 6 first, an estimate of steady-state temperature was obtained by averaging over the time window shown in Fig. 10 and listed in Table 10. However, unlike for the experimental data, no empirical investigation was performed to determine sensitivity of the mean temperature (as the steady-state temperature estimate) to perturbations of the time window by shifting it and/or altering its width. Instead, uncertainty bounds listed in Table 11 are the maximum and minimum instantaneous temperatures over the time window. These are also depicted by the upper and lower extents of the time box in Fig. 10.

This latter approach is an easy way to get uncertainty bounds, but is thought to give considerably exaggerated uncertainty magnitudes for simulation results that have plateaued to a (noisy) steady state. Indeed, the time-window maximum and minimum for the experimental data are found in Table 9 to be roughly 25K to 35K higher or lower than the time-window mean. Yet experimentation with different plausible time windows on the steady-state portion of the experimental data indicated that a more reasonable uncertainty to ascribe to the time-window means is $\pm$ 5K. In comparison, the upward and downward instantaneous differences from the mean for Sim. 6 in Table 11 are roughly 20K—considerably less than the 25 to 35K differences from experimental time-window means. Therefore, if the experimental and simulation results have proportionate sensitivities of their time-window means to different plausible time windows that could reasonably have been chosen, then something less than $\pm$ 5K would be more reasonable to assign for the uncertainty of steady-state temperature for Simulation 6.

Indeed, the different vertical extents of the three time-window boxes in Fig. 10 portray an exaggerated uncertainty attributed to the Sim. 6 results. For Experiments 6 and 7 and for Simulation 6 the scale of temperature oscillation over their time windows in Fig. 10 is roughly the same. Yet, the vertical extents of the time boxes, which represent the uncertainty ascribed to

the time-window means as estimates of steady-state temperature, are clearly of different scale. Hence, it is reasonable to conclude that an easy and conservative approach to bounding the uncertainty on time-window means, as an alternative to the labor intensive approach of sampling different reasonable time windows (recall that we had 7 other TCs to process × six simulations), is to use instantaneous maximum and minimum temperature over the time window. (Unfortunately, this likely exaggerates by a considerable amount the uncertainty that should reasonably be attributed to steady-state point estimates given by time-window means.)

Because of this, it was concluded that little advantage accrues from the processes of determining a representative time window and then computing a mean, versus the much simpler approach of treating plateaued simulation results with the same visual procedure that is applied to the non-plateued results. Accordingly, the latter approach was taken for Sim. 2, 4, and 6 results in many cases (for many TCs). Table 12 indicates which cases involved a time-windowing process and which involved just visual judgment. (Note that data in Table 10 coincides with the row for TC5 in Table 12.) Thus, the TC5 results in Tables 10 and 11 for Simulations 2 and 4 come from the visually estimated uncertainty bounds depicted in Fig. 11.

Table 12. Values in brackets [] are visually projected limits to anticipated change from end-of-simulation temperatures to asymptotic steady-state values. Where time ranges are listed, a temperature mean was calculated over the time window to determine the point estimate for steady-state temperature.

	Sim 1	Sim 2	Sim 3	Sim 4	Sim 5	Sim 6
TC 1	[-10,+10]	[-30,+30]	[-10,+10]	[-5,+10]	[-30,-5]	190-241 sec
TC 2	[-20,+20]	[-30,+30]	[-5,+20]	240-285 sec	[-15,0]	190-241 sec
TC 3	[-10,+50]	[-30,+30]	[+10,+80]	240-285 sec	[-15,0]	190-241 sec
TC 4	[-10,+100]	[-30,+30]	[-5,+20]	240-285 sec	[-15,0]	190-241 sec
TC 5	[-10,+30]	[-30,+30]	[-5,+20]	[-5,+20]	[-15,0]	190-241 sec
TC 6	[-10,+40]	[-30,+30]	[0,+50]	240-285 sec	[-15,0]	190-241 sec
TC 7	[-10,+50]	[-30,+30]	[0,+50]	240-285 sec	[-10,+5]	190-241 sec
TC 8	[-10,+60]	[-30,+30]	[-30,+30]	240-285 sec	[-15,+5]	190-241 sec

Note that the various error bars and time-window boxes for all eight TCs are shown in Figures D1 – D16 (Appendix D) so that readers can judge for themselves whether the subjectively determined uncertainty ranges on steady-state temperatures are reasonable. The error bars and time-window boxes are only accurate to within "hand drawn" accuracy. These give a qualitative sense of the magnitudes of the quantities involved, but for quantitative accuracy the tables should be consulted. Table F (Appendix F) is a version of Table 12 that includes the data for all eight TCs. Figures G3 – G8 (Appendix G) plot the data in Table F. The bar plots show the Min. to Max. "*graphical processing uncertainty*" of the estimated steady-state temperature for each TC and for each simulation.

Figures G1 and G2 show the graphical processing uncertainties for Experiment 6 and 7 results. Again, these uncertainties are only ± 5K, based on some experimentation with different plausible time windows on the steady-state portion of the experimental data curves. By comparing Figs. G1 and G2 to Figs. G3 – G8, it is immediately apparent that the graphical uncertainties for the simulation results are slightly to substantially larger than the experimental results. The bar plots

also reveal that temperatures around and up & down the cone-shaped calorimeter generally vary less in the experiments than in the predictions. Additionally, the good repeatability between experiments 6 and 7 (Figs. G1 and G2) can be seen.

4.3.4 Uncertainty Processing of Experimental Data for Model Validation Comparisons

The experimental data is here processed in a specific manner for model validation comparison to simulation results according to the validation paradigm proposed and illustrated in Romero, 2005, 2007b, 2008, and 2009. There are many other model validation approaches of various flavors that one could pursue (see Romero, 2008 for a sampling of references on this subject). However, the one applied here appears to uniquely have the enabling features and workable simplicity to handle all the difficult attributes of the current validation problem. In fact, the framework has evolved to suit this particular problem and several other challenging validation problems confronted at Sandia over the last several years.

For TC 5 as an illustrative case, Figure 12 presents the perceived dominant experimental uncertainties (from a model validation perspective) concerning its steady-state temperature. The sizes of the error bars in the figure are approximately to scale for the numerical magnitudes denoted in the figure.

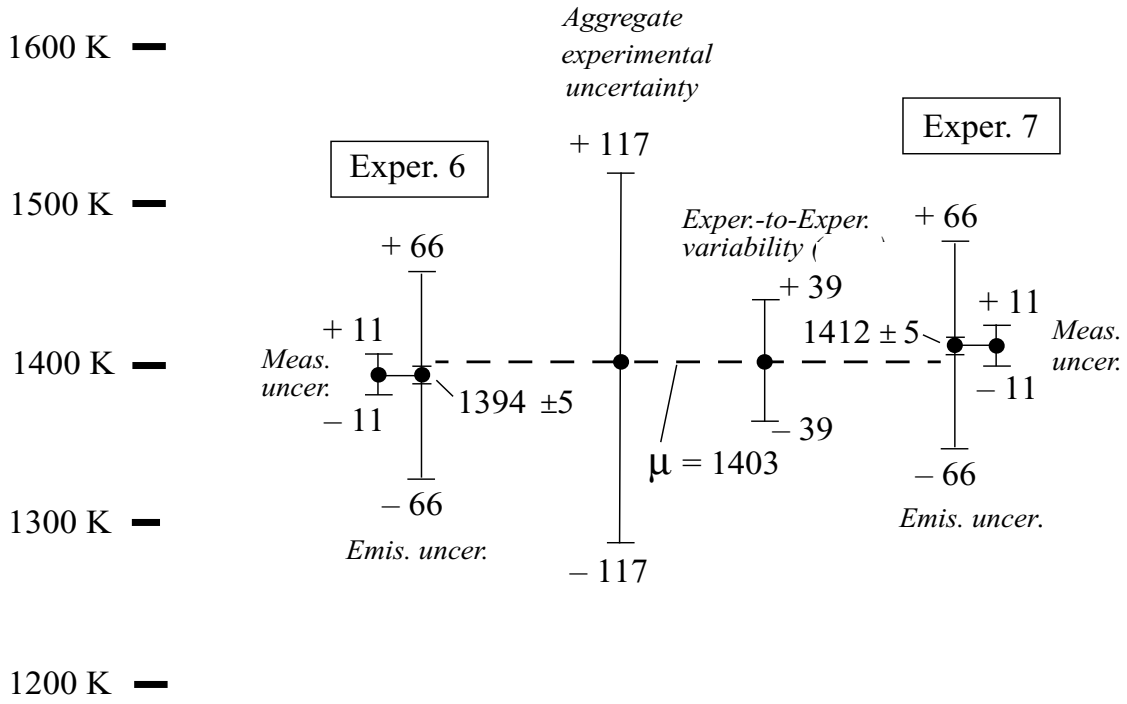

Figure 12: Experimental uncertainties and rollup to aggregate experimental uncertainty at TC5. All temperatures are in degrees K. Results for the other seven thermocouples are plotted in Appendix H.

We first consider Experiment 6. From Table 9 it has a steady-state mean temperature of 1394K over the applicable time window. It was previously established that this mean is subject to a ± 5K graphical uncertainty, thus the designation 1394K ±5K in the figure.

The ± 11K measurement uncertainty indicated in the figure is an amalgamation of several sources. First, manufacturing variability of the 1/16-inch diameter ungrounded-junction MIMS Type-K TCs used in the experiments is specified by the manufacturer to result in a "two-sigma accuracy of 2.2 ℃ or 0.75% of reading in ℃, whichever is greater" (see [21]). This accuracy level is said to exist over a temperature measurement range from 200 ℃ to 1000 ℃. The wording is generally interpreted (e.g. [21]) to imply that, although a given TC's particular transducing error ε ($= T_{indicated} - T_{true}$) is not known, the relative likelihood of what the error might be is governed by a normal distribution with standard deviation σ = ½(2.2 ℃ or 0.75% of reading in ℃, whichever is greater). (See shaded distribution associated with note ② in Figure 13.) Hence, the probability that the absolute value of the error is less than 2σ is given by integrating the shaded portion of the normal distribution that lies within $\pm 2\sigma$ of $T_{indicated}$. This integration yields a value slightly larger than 0.95. Accordingly, >95% probability exists that the given TC's error has a magnitude less than 2σ; $|T_{indicated} - T_{true}| < 2\sigma$. Unfurling this inequality yields: $T_{indicated} - 2\sigma < T_{true} < T_{indicated} + 2\sigma$. Hence, >95% probability exists that the true bead temperature lies with $\pm 2\sigma$ of the indicated bead temperature.

The above characterization is presumably obtained with a measurement system (particular data acquisition system, length of TC leads, length of electrical signal cables, etc.) that is properly calibrated for accuracy. Bias error is then introduced by the different particulars of the Sandia measurement system relative to the manufacturer's system. Characterization of the Sandia measurement TC channels in e.g. [2] and [21] has determined that channel accuracies usually range well within 1 ℃ even for high-temperature calibration signals (standards) emulating 1000 ℃ (1273 K), in the neighborhood of calorimeter temperatures in the present tests. With the error characterization from these activities, individual TC readings in the experiments could be bias-corrected, but usually are not because of the relatively small errors involved. Instead, a "blanket" uncertainty is assigned to the reported data to cover any error due to the Sandia measurement system. We here assign an interval uncertainty of ± 0.25% of ℃ reading. This equates to greater than ± 2.5 ℃ in the present case, representing a reasonable upper bound on measurement system errors traditionally seen in assessments against calibration standards at these elevated temperatures.

Hence, two significant sources of uncertainty are surmised to exist with regard to face-value temperature readings in the present experiments. Figure 13 helps illustrate the uncertainty sources and their implications. The probability density functions (PDFs) in the figure represent the uncertainty in true temperature due to TC-to-TC variable error (*aleatory* uncertainty) characterized by the manufacturer, assuming channel bias in their measurement system is corrected using a reliable calibration standard. The depicted potential shifts in the PDF (and therefore where the true temperature is expected to lie) are caused by potential differences between the manufacturer and Sandia measurement systems. Uncertainty in the magnitude of the systematic differences is here taken to be an interval (*epistemic*) uncertainty of ± 0.25% of reading in ℃.

Accordingly, if no Sandia measurement-system bias exists, the true TC bead temperature would be expected with >95% probability to lie within the range marked by the smaller error bar in the figure. However, when Sandia measurement-system bias does exist, and its value is

characterized to lie e.g. within an uncertainty range of $-\Delta^-$ to $+\Delta^+$ as depicted in Figure 13, then the said PDF uncertainty (and therefore where the true temperature is expected to lie) might be shifted up or down by any value within the extremes shown.[4]

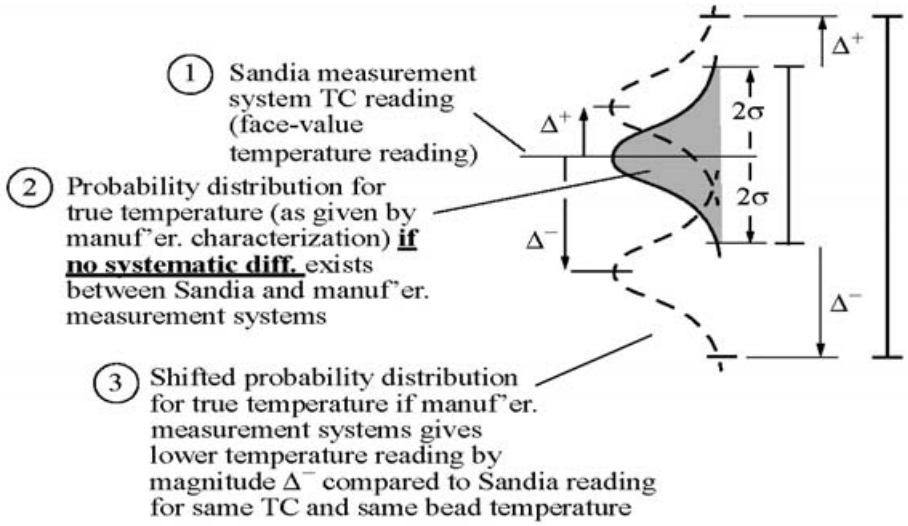

Figure 13: Uncertainty of TC reading error is governed by probabilistic uncertainty (PDF) and potential systematic shifts in the PDF. Aggregate uncertainty interval shown at right is given by shifting either PDF or its interval representation shown, through the uncertainty range $[-\Delta^-, +\Delta^+]$ of the potential error of Sandia meas. system relative to TC manuf. meas. system (that manuf. supplied PDF is referenced to).

Thus, the region within which the true temperature is expected to lie (at the 95% probability level) is given by the large error bar at right in Figure 13. The lower and upper extremes of the large error bar are formed by simply adding the respective extremes of the PDF and interval source uncertainties: $[L,U] = [(-\Delta^- + -2\sigma), (\Delta^+ + 2\sigma)]$.

For the present case we get [L,U] = [(-0.25% + -0.75%), (0.25% + 0.75%)] of ℃ reading = [-1%, 1%] of ℃ reading. This uncertainty range can also be expressed conventionally as ± 1% of ℃ reading. Consulting Table 9 for ℃ reading for Experiments 6 and 7, ± 1% yields the numerically rounded [–11K, +11K] error bars in Figure 12 (analogous to the large error bar in Figure 13). Table E.1 contains the values of 1% of ℃ reading for the other TCs.

[4] Under such shifts, the superposition spoken of here is a simplifying approximation, but is reasonable for the present circumstances and validation assessment. True superposition requires that the PDF in Figure 13 is independent of the second uncertainty that precipitates the shifting, and that the distribution remain unchanged or invariant as it shifts. The independence condition is met here and in many other real settings. However, the invariance condition is not strictly met here, and is probably difficult to strictly meet in general. Here, the standard deviation (thus width) of the distribution is posed as a percentage of temperature reading. Since temperature magnitude changes as the distribution shifts vertically over the $[-\Delta^-, +\Delta^+]$ range in Figure 13, the width of the distribution would change as well, violating the strict superposition conditions. However, this non-invariance effect is not large enough to be material to the validation conclusions here. If the non-invariance effect *is* significant and therefore important to capture, a Monte Carlo procedure like that demonstrated in Romero, et al., 2005 can be employed.

Usually, a third—and dominant—source of temperature indication error exists, due to TC attachment effects. That is, the TC bead is not usually at the same temperature as the surface it is attached to because of contact resistance effects and heat transfer to or from the bead. See Figueroa (2006) for a detailed presentation of the issues, and quantification of the effects via finite-element modeling. Since it is really the surface temperature that is desired from the measurement, and not actually the bead temperature, any difference between the two is usually considered to be an error in the measurement. Such error has been indicated in Sandia investigations (e.g. Figueroa, 2005; Nakos, 2004) to be as much of 6% of ℃ reading under certain conditions. Such temperature differences or lags are not considered in the present activity because steady-state temperature is the quantity of interest. For this quantity, positive and negative temperature lags are presumed to cancel out in the calculation of mean temperature as the instantaneous temperature oscillates noisily about the steady-state mean. Depending on the actual oscillation history, non-symmetric time-weighting of positive and negative lags could lead to non-complete cancellation, but any such effect is likely to be small to negligible. It seems reasonable to assume here that any such effects are small enough to be covered by the significant margin of conservatism in the assigned 0.25% uncertainty discussed previously.

Another source of validation uncertainty in the indicated experimental steady-state temperature is represented by the [–66K, +66K] error bars labeled "*Emis. uncer.*" in Figure 12. It is evident that these are dominant uncertainties in the individual experiments. These arise from an uncertain *input* to the experiments (calorimeter and enclosure emissivity) as opposed to the aforementioned uncertainties in the measurement and processing of the experimental *output* (temperature).

By far, emissivity of the calorimeter exterior and enclosure interior is thought to be the factor that yields the highest sensitivity of calorimeter steady-state temperature to experimental input-factor uncertainty. As previously explained, Simulation 6 at $\epsilon = 0.96$ is a perturbation from Sim. 2 at $\epsilon_{nominal} = 0.86$, all other simulation parameters being the same. From Sim. 6 and Sim. 2 results, a first-order finite-difference approximation to $dT/d\epsilon$ at every point on the cone surface can be formed. Then the linear projection equation $\Delta T \approx [dT/d\epsilon] \bullet \Delta\epsilon$ can be used to estimate the steady-state temperature change ΔT from Sim. 2 steady-state temperature at a given point on the calorimeter surface, for any value of emissivity ϵ different from $\epsilon_{nominal}$ (where $\Delta\epsilon = \epsilon - \epsilon_{nominal}$).

The uncertainty range for emissivity of the calorimeter exterior surface and the enclosure interior surfaces (walls, roof, and floor) is indicated to be $\epsilon = 0.76$ to 0.96 as established earlier. The upward ΔT perturbation at TC5, corresponding to the upper-bound perturbation $\epsilon = 0.96$ from $\epsilon_{nominal} = 0.86$, is given directly by subtracting the central estimate for Sim. 2 steady-state temperature in Table 11 from the central estimate for Sim. 6 steady-state temperature. The result is $\Delta T = +33$K. From the fact that a downward uncertainty perturbation $\epsilon = 0.76$ from the nominal value 0.86 is the same magnitude as the upward perturbation from 0.86 to 0.96, the downward temperature perturbation is −33K by linearity of the projection equation. Therefore, the full uncertainty range of temperature at TC5 due to an emissive uncertainty [0.76, 0.96] is projected to be 66K, given by the uncertainty interval [−33K, +33K].

Indeed, in the next section this interval [−33K, +33K] is an element of the *prediction* uncertainty for steady-state temperature at TC5 (see Fig. 14). Furthermore, since the validation framework applied here assesses how closely the experimental and modeled systems transform experimental inputs to output results, an objective assessment would map any uncertainty of the experimental inputs through the modeled and physical systems, and then compare how output results differ. However, unlike the modeling case, in the physical case we do not have empirical quantification of how the physical system outputs of calorimeter TC temperatures vary as the Pyromark emissivity varies over its uncertainty range. This experimental knowledge deficit, and the fact that the experimental output results correspond to a specific but unknown input emissivity (although it almost certainly lies within the uncertainty range discussed), have several important implications for model validation and model validation methodology (see Romero, 2008; Romero, 2009).

Accordingly, the present circumstances that the uncertain input of interest is non-traveling (see Footnote 1) and is predominantly systematic over the two experiments, dictate a somewhat non-intuitive treatment ("*data-conditioning*" of the experimental data with respect to the uncertain emissivity) to minimize the chances of committing a "Type X" model validation error.[5] Here the uncertainty added to the experimental results turns out to be [−66K, +66K] as shown in Figure 12. This is twice the uncertainty [−33K, +33K] added to the *prediction* results in Fig. 14.[6]

Finally, we address the test-to-test variability of the experimental results. Consider the uncertainty in Figure 12 associated with the nominal point results of the two experiments, 6 and

[5] The model validation methodology employed here is skewed toward preventing a "Type X" model validation error (Romero, 2008) of an incorrect conclusion of 'no significant model bias' when in fact significant bias does exist but is hidden by systematic uncertainty in non-traveling input factors in the experiments. The drawback is that the framework likely exaggerates the uncertainty "resolution level" within which it can be established that the model emulates the real system. (The tradeoff here is analogous to the situation in statistical hypothesis testing, where the more one chooses to skew (decrease) the odds of incorrectly rejecting a true hypothesis (Type I error), the more likely it is that a Type II error will be committed of incorrectly accepting a false hypothesis. As in hypothesis testing, the presence of uncertainty forces one into a position of having to make a choice of which undesirable outcome is the least undesirable.) Thus, the methodology here favors incurring a "Type Y" error of exaggerating the range of possible model bias relative to what it is likely to actually be, and accepts this tradeoff in preference to incurring a Type X error of underestimating the model bias. This choice is argued in Romero, 2008 to best support the objectives of Best Estimate + Uncertainty extrapolative predictions with the model.

[6] This factor of two arises when the model is used as an approximation for the experimental change (slope) in TC5 temperature versus change in the input factor (here emissivity). This is just a nominal estimate for what the data conditioning factor actually should be. The factor is formally two times the ratio r of experimental slope to modeled slope. Thus, the factor is two when $r = 1$, i.e., under the nominal approximation of equal experimental and modeled slopes. However, the sensitivity of validation conclusions to uncertainty in r should be investigated as part of the validation procedure. It is determined that the actual ratio of experimental to modeled slopes can be up to $r = 1.5$ (for a factor of 3) before the experimental uncertainty bar in Fig. 14 extends outside the range of prediction uncertainty and changes the validation conclusions arrived at later. The actual experimental slope is expected to be well within this allowable 50% difference from the modeled slope.

7. First note that the measurement and emissivity-related uncertainties are completely correlated. That is, since the same TC and data acquisition system and channel was used for TC5 in the two experiments, any associated bias errors in reading vs. true temperature are essentially the same in the two experiments. The same is true of the uncertainty due to emissivity in the experiments. Although the emissivity in the experiments is unknown to within a relatively large range of 0.76 to 0.96, it is reasonable to postulate the experiment-to-experiment differences in emissivity are small comparatively. Hence, the associated uncertainty in experiment 6 and 7 results is closely correlated (systematic over the two experiments).

Conversely, the ± 5K graphical uncertainties associated with the steady-state temperature averaging windows for the two experiments can be considered to be independent and uncorrelated among the two experiments. This dictates that this source of uncertainty, for the purposes of characterizing experiment-to-experiment variability, be treated differently than the ones above.

First, however, consider the instructional case of only one experiment (either 6 or 7). The aggregate uncertainty for the single experiment would be constructed as follows. The [–11K, +11K] measurement uncertainty in Figure 12 can be conceived as being subject to vertical shifting over the range [–66K, +66K] due to the emissive uncertainty. Such shifting is already familiar from the previous discussion pertaining to Figure 13. In the way that the uncertainty ranges are added or superposed in accordance with the assumptions in Footnote 4, the results here would yield [(-11K + -66K), (11K + 66K)] = [-77K, +77K]. This uncertainty bar about the nominal measured temperature would in turn be subject to vertical shifting of ± 5K associated with the steady-state temperature graphical processing uncertainty. An aggregate uncertainty of [-82K, +82K] would result. This would be the case for either Experiment 6 or 7 alone.

Now consider Experiments 6 and 7 together. With reference to Figure 12, the nominal results are respectively 1394 K and 1412 K. The 18 K difference between these results cannot be explained by the ± 5K uncorrelated processing uncertainties in each result. (Recall that the other uncertainties are effectively correlated or systematic between the two experiments, so cannot explain or contribute to any relative differences in the two experimental results.) Therefore, some other explanation lies behind the experimental differences. Certainly, things varied between the two experiments that we could not characterize or explicitly treat in this project due to practical limitations.[7]

[7] If we had quantified the input variabilities and could afford to propagate them to the simulation output, just as the experimental system propagated them to the experimental output, then we would have approximately offsetting effects in the validation comparisons to come later. Instead, neglectance of experimental input variabilities on the simulation side may show up as an under-represented uncertainty band in the validation comparison against the aggregate experimental uncertainty. Any consequent "uncertainty shortfall" might then be mapped into selected parameters of the model to add a physical variability effect to it. This so-called "*model conditioning*" (Romero, 2007a; 2007b: 2008; 2009) arguably supports an objective of Best Estimate + Uncertainty modeling for extrapolative prediction. It will be established later that no such model conditioning is indicated to be necessary in the present activity. Indeed, the model-intrinsic uncertainties of Table 6 will be seen to bound the experiment-to-experiment variability in the physical results.

In any case, we can reasonably posit that if many other repeat experiments were run, the results would vary according to a Normal distribution, as is often the case with complex experimental systems. We can get estimates of what the mean and variance of the Normal distribution would be by calculating these from the 1394 K and 1412 K nominal experimental results. The mean of these is 1403 K as denoted in the figure. The standard deviation S, times two, is 2S = 25 K. It must be kept in mind that this two-sigma magnitude of 25 K only *nominally* corresponds to 95% included probability in the postulated normal distribution of experiment-to-experiment steady-state temperature at TC5.[8]

The nominal treatment also ignores the ± 5K graphical processing uncertainties in the two steady-state temperatures. Because this uncertainty is uncorrelated over the two experiments, a worst-case (largest variance) treatment of this uncertainty involves decreasing the lower nominal result, 1394 K, by the maximum possibility over the applicable ± 5K uncertainty range; and increasing the upper nominal result, 1412 K, by the maximum possibility over its independent ± 5K uncertainty range. This yields adjusted results of 1394K –5K = 1389 K, and 1412K + 5K = 1417 K. The accompanying two-sigma magnitude is S_high = 39.1. This compares to the two-sigma value of 25 obtained in the previous paragraph when the uncorrelated ± 5K window processing uncertainties were not accounted for. A rounded value of 39 (shown in Figure 12) is used in the following.

The effect of the correlation treatment is very significant here. If the ± 5K uncertainties were perfectly correlated among the two experiments, then these would constitute a systematic uncertainty over the two experiments. Then, consistent with Figure 13, the aggregate uncertainty from these two factors (graphical processing and experiment-to-experiment variability) would be to shift the (two-sigma = 25K) normal distribution over a ± 5K range. The result would be [(-5K + -25K), (5K + 25K)] = [-30K, +30K] by the linear superposition approximation (Footnote 4).

Instead, if the ± 5K graphical processing uncertainties are treated as independent and uncorrelated over the two experiments, the result is [-2S_high, +2S_high] = [-39K, +39K] as already determined. Therefore, the added effect of the uncorrelated ±5K processing uncertainties

---

[8] The actual standard deviation of a large number of experimental repeats could be very different from the S = 25K/2 calculated from just the two experiments. The small-sample uncertainty in the standard deviation value, and also in the mean value, is not accounted for in this paper. Hence, we cannot state with reasonable statistical confidence that the mean±2S = 1403K ±25K defines an interval that encompasses 95% of the postulated normal distribution for experiment-to-experiment steady-state temperature variability. We can only state that this interval gives a nominal quantification of the physical variability. In fact, if the small-sample uncertainty on the apparent experimental variability is taken into account, this "uncertainty on the variability" or "epistemic uncertainty on the aleatory uncertainty" is large enough that it can potentially overturn our validation affirmations at some of the eight TC locations. Nonetheless, within the sampling uncertainty, it is also possible that an even stronger affirmation of model validity could occur, depending on the direction of the actual errors in the calculated values $\bar{x}$=1403K and S = 25K/2.

is a ±14K increment to the standing ±2S = ±25.0 nominal uncertainty from experimental variability. The ±14K is nearly three times the added effect if the ± 5K processing uncertainties are treated as perfectly correlated (systematic) over the two experiments.

To close out this subsection, we combine the experimental measurement and emissivity-related interval uncertainties with the normal PDF for experiment-to-experiment variability (mean 1403K and standard deviation S_high = 39K/2). Following the paradigm of Figure 13, the [–11K, +11K] measurement uncertainty (interval) is superposed/added with the PDF uncertainty to get: [(-11K + -39K), (11K + 39K)] = [-50K, +50K]. The interval uncertainty [–66K, +66K] due to uncertain emissivity is combined in by further superposition to get: [(-66K + -50K), (66K +50K)] = [-116K, +116K]. By using the numbers from each term with more decimal-place precision, we get the more accurate result [-117K, +117K] depicted by the uncertainty bar labeled 'Aggregate experimental uncertainty' in Figure 12.

Analogous quantities and results to those presented in Figure 12 for TC5 are presented in Table E.1 (Appendix E) and Appendix H for the other TCs.

4.3.5 Uncertainty Processing of Simulation Results for Model Validation Comparisons

Figure 14 shows FUEGO simulation results at TC5 location for Simulations 1 – 5. These were all run with the nominal value of emissivity, $\epsilon_{nominal} = 0.86$. The range of aggregate experimental uncertainty from Fig. 12 is plotted in Figure 14 to lend a sense of scale and location relative to the simulation uncertainty. The central-estimate values of steady-state temperature from Table 11 are printed in the figure beside the plotted filled dots. The maximum and minimum reasonable steady-state temperature bounds from Table 11 are also plotted in Figure 14, as unfilled diamond symbols.

The *nominal* steady-state temperature values indicate that the BVG turbulence model yields greater object heating than the TFNS model—all other simulation parameters being equal. This agrees with expectations.

When the emissivity uncertainty is accounted for, the expectations still hold up. For instance, consider the TFNS-High simulation (#2) and the BVG-High simulation (#4). The emissivity-related [−33K, +33K] uncertainty bars of these two simulations overlap some in Fig. 14. However, recall that these uncertainty bars represent *correlated* or systematic uncertainty over the set of simulations. That is, whatever the true value of emissivity is, it is the same for all simulations. If the true value (or any value) were input to the simulations, it would not yield e.g. a value on the upper portion of the uncertainty bar of Sim. 2 and a value on the lower portion of the uncertainty bar of Sim. 4. Rather, the results would be correlated such they would both lie at closely the same vertical position within each error bar. Therefore, although the error bars of Sim. 2 and Sim. 4 overlap some, giving the *appearance* that it is possible to get a temperature realization from BVG-High Sim. 4 that is lower than a corresponding realization from TFNS-High Sim. 2, this is not really the situation here.

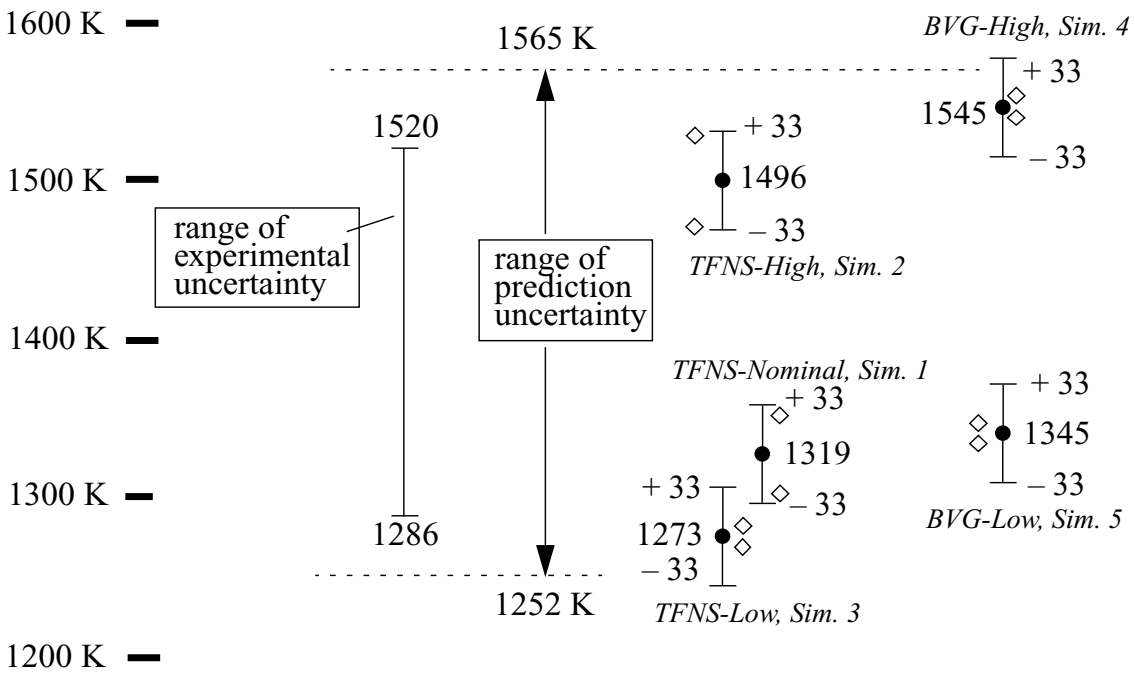

Figure 14: Simulation results and uncertainties at TC5, with range of prediction uncertainty compared against range of aggregate experimental uncertainty. All temperatures in degrees K. Results for the other seven thermocouples are plotted in Appendix H.

The expected ordering holds even up when the graphical processing uncertainty is accounted for. In contrast to the emissivity related uncertainty, the graphical processing uncertainties (min and max bounds in Table 11) are *uncorrelated* across the various simulation results, and *can* significantly shift simulation results relative to each other. For example, in the extreme worst combination the graphical uncertainty could allow: *a*) a shift of Sim. 4's uncertainty bar downward until its midpoint (filled dot) aligns with the local lower diamond; and *b*) a shift of Sim. 2's uncertainty bar upward until its midpoint aligns with the local upper diamond. Even in this worst case the BVG-High Sim. 4 uncertainty bar remains higher in vertical position than the TFNS-High Sim. 2 bar. This implies a higher simulated temperature for BVG-High than for TFNS-High. Recall also that this is under a worst-case realization of the uncorrelated graphical uncertainties, and that the graphical uncertainty magnitudes are likely highly exaggerated for the simulation results, as discussed earlier.

It is otherwise observed that, for a given turbulence model form (TFNS or BVG), the prescribed parameter sets for Low, Nominal, and High heating give consecutively hotter fires, or at least consecutively greater heating of the calorimeter as indicated at TC5 and the other seven TC locations. This ordering is retained at all TC locations under all possible realizations of the graphical and emissivity uncertainties.

These results support the proposition that, for the model validation purposes here (and for extrapolative predictions in general) it is not necessary to expend simulations at the BVG-Low and TFNS-High and Medium parameter sets. These parameter sets (#5, 2, and 1 respectively)

routinely yield results that lie between the heating extremes of parameter sets #3 (TFNS-Low) and #4 (BVG-High).

Thus, the effects of the six dominant sources of intrinsic modeling uncertainty in the fire dynamics model (Table 6) can be effectively bounded by running FUEGO simulations at just the two "extreme" parameter sets #3 and #4. Of course, other simulations have to be run to assess the effects of other sources of uncertainty (like uncertain emissivity, numerical discretization, etc.) in a given prediction.

We now turn to the model validation objective of our analysis. Ultimately the aggregate experimental uncertainty in Figure 14 will be compared against an aggregate simulation uncertainty that is appropriate to a validation assessment. The criterion for the model to be affirmed is that the model predictions, with uncertainties properly accounted for, yield an uncertainty band that encompasses the aggregate experimental uncertainty.

Otherwise, the processed experimental uncertainty, as presumably the best empirical evidence of where "reality" lies and where the next experimental result(s) would occur, lies outside the range predicted by the modeling. Thus, the predictions would fall short of spanning and capturing the empirical evidence—whether through improper model form or via misrepresented parameter uncertainties, or both. In any case, it could not be asserted that the model was fully 'valid'. Again, this is the criterion of the present validation framework, but other validation criteria and frameworks are actively being discussed in the literature. No over-riding consensus has emerged yet, but the current framework arguably directly supports a goal of Best Estimate + Uncertainty extrapolative prediction. See Romero (2007a) for further discussion.

In the present framework, the preliminary aggregate prediction uncertainty in Fig. 14—before accounting for graphical uncertainties—ranges from the low end of the lowest uncertainty bar (given by TFNS-Low Sim. 3), to the high end of the highest uncertainty bar (from BVG-High Sim. 4). That is, the emissivity uncertainty and the six uncertainties in Table 6 have possible combinations or realizations over their joint uncertainty space (where these seven factors are justifiably assumed to be independent of each other) that can yield model predictions which vary from the low end to the high end of the said uncertainty range. This preliminary range of prediction uncertainty is impacted by the graphical uncertainties as explained next.

The graphical processing uncertainty for the BVG-High Sim. 4 results is given by the min and max bounds in Table 11. The graphical uncertainty allows that Sim. 4's uncertainty bar in Fig. 14 can really lie anywhere within an upward or downward shift where its midpoint (filled dot) remains between the upper and lower unfilled diamonds to the side of the uncertainty bar. Analogous freedoms are allowed for the Sim. 3 uncertainty bar to be shifted between the upper and lower diamonds at its side. Recall that the graphical uncertainties are not correlated with each other, so the allowable shifting of Sim. 4's uncertainty bar is independent of Sim. 3's.

At the upper end of the simulated temperature range, treatment of the graphical uncertainty for Sim. 4 impacts the validation determination relative to the high end (1520 K) of the experimental temperature uncertainty range shown in Fig. 14. Analogous considerations hold for the graphical uncertainty for Sim. 3 and the validation determination at the low end (1286 K) of the

experimental uncertainty range. Within the graphical uncertainty, the Sim. 4 uncertainty bar could be translated upward, and the Sim. 3 results could be translated downward, such that validation margins are greater at both the upper and lower ends. The opposite extreme possible combination is a downward shift in Sim. 4 results and an upward shift in Sim. 3 results, such that validation margins decrease at both the upper and lower ends.

A treatment which increases validation margins here, or which tends to create a closer comparison when positive margins like those in Fig. 14 do not exist, is said to be *non-conservative*.[9] This type of treatment could enable the validation criterion to be (falsely) met or approached closer, while the actual value of the factor (for no graphical processing error) might correspond to a more biased model than the validation assessment leads one to believe. Hence, this is one possible way to commit Type X model validation error. Type X error can arise from many other sources, such as model discretization uncertainties, systematic uncertainties of non-traveling experimental inputs (here, emissivity as already discussed), and other sources catalogued in Romero, 2009.

To guard against the potential for Type X error that the graphical uncertainties pose, the framework takes a *conservative* approach of attempting to eliminate the risk entirely. To do this, the most extreme possible combination is invoked of shifting the Sim. 4 uncertainty bar downward the full allowable amount until its midpoint (filled dot) is beside the lower diamond at its side, and shifting the Sim. 3 uncertainty bar upward the full amount until its midpoint is beside the upper diamond at its side. This maximally decreases the validation margins at both the upper and lower ends of the data range. Hence, this likely causes a Type Y model validation error of the framework exaggerating the perceived extent of potential model bias. Unfortunately, eliminating the risk of Type X validation error comes with a tradeoff of committing a Type Y error. An alternative is to just simply ignore the graphical processing uncertainties. However, this incurs a substantial risk of Type X error in the validation conclusions.

Hence, the "validation conservative" lower temperature limit of prediction uncertainty is obtained as follows. The Sim. 3 uncertainty bar in Fig. 14 is centered on the upper diamond to its right, which has a temperature of 1285 K (= 'max' value for Sim. 3 in Table 11). The temperature at the bottom of this uncertainty bar is therefore 1285 K – 33K = 1252K. This temperature is marked by the lower horizontal dashed line in the figure.

[9] Accounting for simulation uncertainty of the intrinsic modeling factors of Table 6 and for the emissivity uncertainty have the effect of expanding the prediction uncertainty as well. Yet, this expansion is not considered to be non-conservative in the validation formulation. As Romero, 2009 explains, from a model validation perspective (in the context of extrapolative predictions and hierarchical modeling) these factors are different in nature from the graphical uncertainty, so are handled differently. The intrinsic modeling factors of Table 6 proceed to any new predictions with the (validated) model, so their uncertainty is transported inherently to new prediction results. This is not the case with the graphical uncertainties being discussed here. New graphical uncertainties/magnitudes will be present in new simulation results. For example, if the new simulations are terminated after arriving at a smooth, flat asymptotic steady-state, no graphical uncertainty will be present at all. In terms of the emissivity uncertainty, like the uncertainties in Table 6 this is an uncertain *input* to the model, not a (graphical) uncertainty from processing of the *outputs* of the model. Furthermore, the emissivity uncertainty is propagated into both the simulation and experimental results. This is not the case with the graphical uncertainties discussed here. They are relevant to only the simulation results.

The validation-conservative upper temperature limit is obtained by a mirrored procedure. The Sim. 4 nominal 1545K result is shifted downward to the lower diamond at its right, at 1532K (= 'min' value for Sim. 4 in Table 11). The temperature at the top of this uncertainty bar is therefore 1532K + 33K = 1565K. This temperature is marked by the upper horizontal dashed line in the figure. Accordingly, the final aggregate range of prediction uncertainty is 1252K to 1565K. Analogous quantities and results to those plotted in Figure 14 for TC 5 are presented in Appendix H for the other TC locations.

5 Validation Comparisons of Processed Experimental and Simulation Results at all Eight TCs—Analysis and Discussion

Summary results (validation comparisons) for all eight TC locations are plotted in Figure 15. The results for the other TCs are based on processing in the same manner as for TC 5.

Commenting first on the robustness of the model affirmation or validation conclusion at the TC 5 location, there is considerable margin for error in the uncertainty estimates and processing of experimental and simulation results before the model affirmation would be overturned. The upper and lower simulation bounds in Figure 14 are seen to fairly spaciously encompass the range of the aggregate experimental uncertainty within which steady-state experimental temperatures are provisionally expected to lie. Errors would have to "conspire" (i.e., coordinate in enough antagonistic directions and magnitudes) to overcome the existing margin for error of 45K (= 1565K – 1520K) at the top. At the bottom, a margin of 34K (= 1286K – 1252K) exists against errors that might conspire. The existence of errors is a given. However, it is much less likely that they would be sufficiently large and sufficiently conspiring that the net result would exceed the indicated margins for error.

At the other seven TC locations the margins for error are even greater at 13 of the 14 upper and lower ends in Figure 15. In no case does the range of experimental uncertainty extend outside the prediction uncertainty.[10] Therefore, a provisional conclusion of model affirmation is arrived at based on validation analysis and comparisons at the eight diversely spaced TCs on the calorimeter.

[10] The experimental and simulation results at the lower end for TC 6 are effectively equal within the decimal roundoff precision employed here for ease of reporting and labeling in the figures.

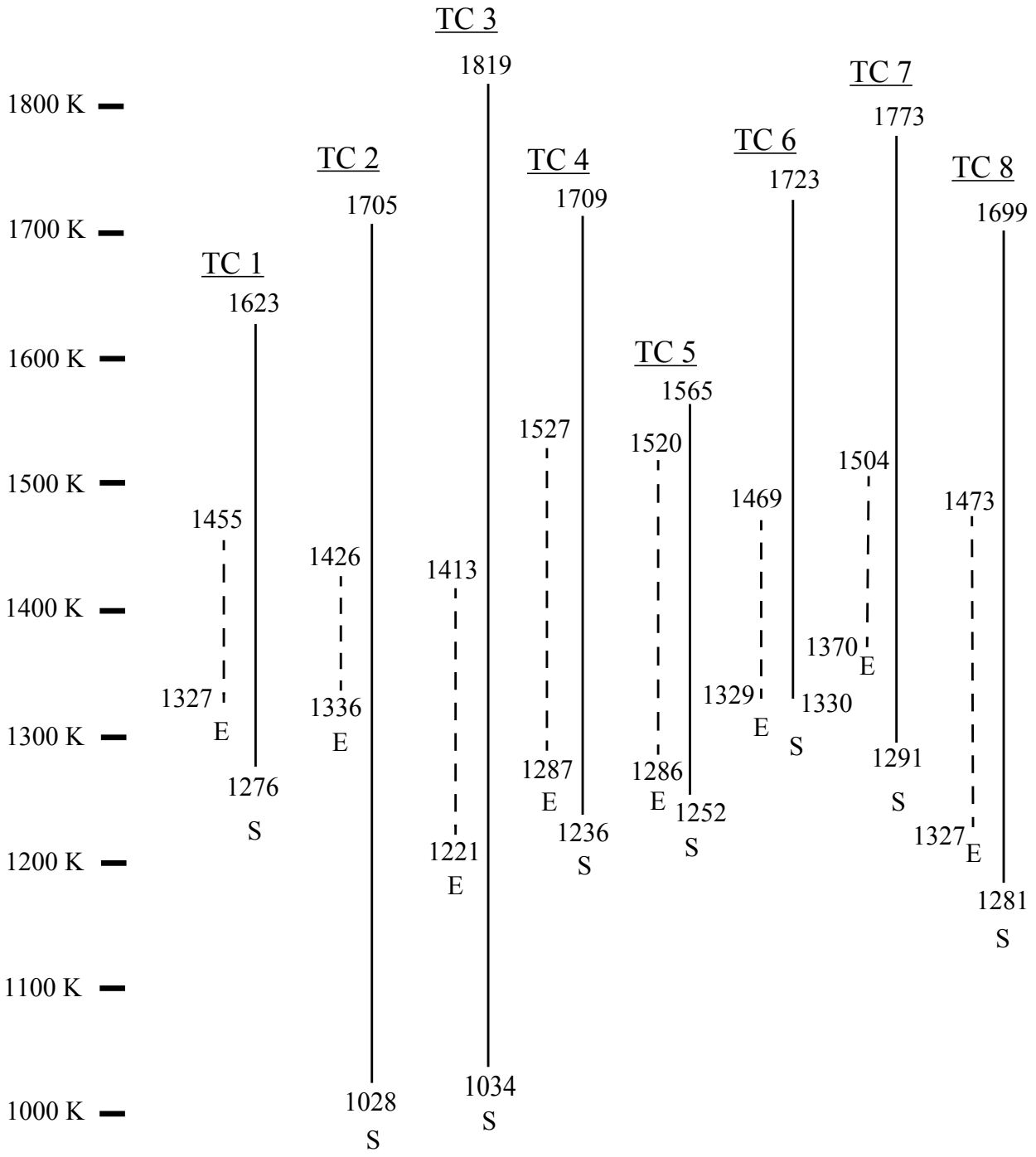

Figure 15: **Validation comparisons of simulation results (S) versus experimental results (E) accounting for relevant uncertainties in both. All temperatures in degrees K. Experimental results are shown to lie within simulation predictions, nominally affirming the model.**

The word ‘provisional’ in the preceding paragraph signifies that large error may exist in our quantification of experiment-to-experiment variability. Nominal mean and standard-deviation results based on only two experimental repeats were used. The uncertainty on these small-sample statistics, and also in the assumption itself of normally distributed variability, could result in errors in an antagonistic direction and large enough to overturn the nominal affirmations at most TC locations. However, note that antagonistic error from this source could be partially offset or even completely overwhelmed by the substantial conservatisms introduced at several points in our experimental and simulation results processing. Moreover, the small-sample errors could go the other way, to more strongly affirm the validation conclusions at any and all TC locations. In any case, uncertainty due to experiment-to-experiment variability is at least nominally accounted for in our validation analysis, results, and conclusions.

Finally, a mitigating factor is pointed out concerning contact resistance between the bottom of the steel cone and the thermally massive steel floor it was bolted to. It was not practical in this project to model the contact resistance at this interface, so an adiabatic boundary condition was applied at the bottom of the cone. This modeling error could be substantial, depending on the particular location considered on the calorimeter. The error causes higher temperatures to be predicted in the calorimeter than would occur if heat transfer from the cone to the steel floor was modeled. The results in Figure 41 show that the experimental uncertainty bars at all TC locations are skewed toward the lower ranges of the prediction bars. That is, modeling the contact conductance at the interface would shift the predicted temperatures downward, especially for the bottom four TCs 1 – 4. This would move things in the “right” direction toward better central agreement between the experimental and predicted temperatures. Indeed, for TC 6 the indicated margin of zero at the lower end is arguably really a small positive margin after a correction for contact conductance is taken into account.

Since the corrections would be expected to be only 10’s of degrees (not hundreds), there is sufficient margin at the top of the simulation uncertainty bars to absorb such corrections and still encompass the experimental data at the upper end. In fact, the lowest upper margin for such a correction is 45K at TC5. All other TCs have a significantly larger upper margin. Also note that TC5 is from the upper set of TCs (Level 10 in Fig. 4), where the effect of the correction would be expected to be fairly small. Indeed, the margin for correction at TC5 and the other TCs in the top row is considered to be far more than adequate. Among the lower set of TCs, the smallest available margin at the upper end for correction is 168K at TC1. This seems to be well in excess of what a correction would reasonably be expected to yield.

All in all, correcting for what is thought to be easily the largest unaccounted-for source of physics modeling error in the validation comparisons would be expected to move things in a direction that strengthens the validation conclusions, but not by a magnitude so large that it goes too far in this direction and overturns the affirmation at the upper end.

Finally, the issue of calculation verification is considered. As previously explained, project constraints required the use of “medium” spatial discretization cell sizes and a “medium” number of discrete-ordinate directions for resolving the participating-media radiation transport. The

solver error-tolerance parameters that control numerical resolution in the steady-state FUEGO computations were also set at “medium” levels. The medium levels used for spatial discretization, radiation transport, and solver computations are representative of what are routinely used for production calculation work by Sandia fire analysts. This is a pragmatic choice to achieve reasonable calculation run times (a few weeks on a thousand processors or less), but is also heuristically supported by comparisons against considerably finer resolution levels also tried on other projects (see e.g. Black, et al., 2007).

In any case, if any discretization-related errors happen to be in the “wrong” (antagonistic) direction that would work against validation margins, the allowable margins for error are 10’s of degrees K as already established. This is significant room for error, but experience indicates that discretization effects *could* be this large or larger. If a quantification of discretization-error uncertainty was available from resolution-refinement studies (e.g. by the methods presented in Roache, 1998), then in the validation analysis these would be handled like the simulation graphical processing uncertainties were. Finally, it is noted that substantial code verification efforts for FUEGO have been undertaken (Domino, et al., 2007), which counts toward the veracity of the validation conclusions here.

6 Conclusion

In view of the arguments just made and the many conservatisms in the validation processing, it is reasonable to state the following. *Based on the validation results at the eight diversely representative TC locations on the calorimeter, FUEGO modeling for wind-driven fire conditions (using the uncertainties in Table 6 for intrinsic modeling uncertainty in the CFD and combustion subgrid scale models) is nominally affirmed to capture the experimental results here (steady-state temperature) according to the pragmatic validation criterion and methodology applied.*

That is, the predicted calorimeter temperatures effectively bound the experimental temperatures at the eight representative locations chosen for comparison on the calorimeter. Furthermore, there is considerable room for errors in the uncertainty estimates and processing of experimental and simulation results before this validation conclusion would be overturned. Moreover, the errors would have to be sufficiently large in magnitude and sufficiently conspiring (combining in antagonistic directions and/or sufficiently avoiding cancelation) to exceed the indicated substantial margins for error. The probability of these joint events occurring may be very low, and cannot reasonably be expected to be high—*but could occur*. In particular, the greatest concerns are: 1) the error associated with using the small-sample (two sample) standard deviation as representative of the standard deviation from a large number of repeat fire tests; and 2) error in the calculated steady-state results due to under-resolution in the discretized model and computation.

Nevertheless, on balance the analysis supports the validation conclusion provisionally arrived at in the present experimental/physical setting. This is a significant result for FUEGO and for Sandia's fire modeling program. In particular, the results post-validate the uncertainty on heating in the QMU analysis [Romero, 2006]. The analysis used fire simulations building off the accident-scenario study [Black, 2004] and used the uncertainty-bounding parameter sets listed in Table 6 that were identified from previous studies [Romero, et al., 2003]. This marks Sandia's first integrated use of fire modeling with validated uncertainty estimates in an abnormal-thermal QMU analysis.

The current work also represents a significant advancement in demonstration of model validation methodology. The versatile model validation analysis framework demonstrated here handles difficulties associated with representing and aggregating aleatory and epistemic uncertainty from multiple correlated and uncorrelated source types, including:

- experimental variability from multiple repeat experiments
- uncertainty of experimental inputs
- experimental output measurement uncertainties
- uncertainties that arise in data processing and inference from raw simulation and experiment outputs
- parameter and model-form uncertainties intrinsic to the model
- numerical solution uncertainty from model discretization effects.

References

Black, A. R., Hobbs, M. L., Dowding, K. J., Blanchat, T. K., 2007, "Uncertainty Quantification and Model Validation of Fire/Thermal Response Predictions", 18th AIAA Computational Fluid Dynamics Conference, Miama, FL, June 25-28, AIAA 2007-4204.

Black, A.R., S.R. Tieszen, J.T. Nakos, V.J. Romero, S.E. Slezak, "Hydrocarbon Fuel Fire Accident Scenario Calculations," Sandia National Laboratories report SAND2004-3195 printed July 2004.

Domino, S.P., G. Wagner, A. Luketa, A. Black, J. Sutherland, "Verification for Multi-Mechanics Applications," 9th AIAA Non-Deterministic Methods Conference, April 23 - 26, 2007, Honolulu, Hawaii.

Domino, S.P., Moen, C.D., Burns, S.P., and Evans, G.H., "SIERRA/Fuego: A Multi-Mechanics Fire Environment Simulation Tool," AIAA Paper 2003-0149, 41st AIAA Aerospace Sciences Meeting, Reno, NV, January 2003.

Figueroa, V., "Effects of Parameter Variations Associated with 1/16" Mineral Insulated Metal Sheathed Thermocouples Installation on the Surface Temperature Measurement of a Uniformly Heated Plate," University of New Mexico School of Mechanical Engineering M.S. Thesis report, April 27, 2006.

Figueroa, V.G., "Emittance of Inconel 600, SS304, 17-4PH Stainless Steel, and Aluminum 7075" Sandia internal memo to Distribution, dated Feb. 20, 2005.

Jones, W.P. and Launder B.E., 1972, *Int. J. Heat Mass Transfer* 15:301-316.

Mehling, H., J. Kuhn, M. Valentin, J. Fricke, "Change of infrared emissivity of metal surfaces during oxidation," *High Temperatures-High Pressures*, 1998, Vol. 30, p. 333-341.

Moen, C. D., G. H. Evans, S. P. Domino, and S. P. Burns, 2002, "A Multi-Mechanics Approach to Computational Heat Transfer," Paper IMECE2002-33098, ASME International Mechanical Engineering Congress and Exposition, New Orleans, LA, November

Nakos, J. T., contact, Sandia National Laboratories

Nakos, J.T., 2004, "Uncertainty Analysis of Thermocouple Measurements Used in Normal and Abnormal Thermal Environment Experiments at Sandia's Radiant Heat Facility and Lurance Canyon Burn Site," Sandia National Laboratories report SAND2004-1023, printed April 2004.

Nicolette, V. F., Tieszen, S. R., Black, A. R., Domino, S. P., and O'Hern, T. J., 2005, "A Turbulence Model for Buoyant Flows Based on Vorticity Generation," Sandia National Laboratories, Albuquerque, NM, SAND2005-6273.

Roache P.J., *Verification and Validation in Computational Science and Engineering*, Hermosa Publishers, Albuquerque, NM, 1998.

Romero, V.J., 2009, “A Pragmatic Framework for Characterizing and Propagating Uncertainty in Hierarchical Modeling: Data and Model Conditioning, Model Verification and Validation, Extrapolative Prediction with Uncertainty,” Sandia National Laboratories report in review.

Romero, V.J., A. Luketa, M. Sherman, 2009, “Application of a Pragmatic Interval-Based "Real Space" Approach to Fire CFD Model Validation Involving Aleatory and Epistemic Uncertainty,” in revision for AIAA *Journal of Thermophysics and Heat Transfer*

Romero, V.J., 2008, “Type X and Y Errors and Data & Model Conditioning for Systematic Uncertainty in Model Calibration, Validation, and Extrapolation,” SAE paper 2008-01-1368 for Society of Automotive Engineers 2008 World Congress, April 14-17, 2008, Detroit, MI.

Romero, V.J., 2007a, "Validated Model? Not So Fast. The Need for Model 'Conditioning' as an Essential Addendum to the Model Validation Process,” 9th AIAA Non-Deterministic Methods Conference, April 23 - 26, 2007, Honolulu, Hawaii.

Romero, V.J., 2007b, “A Paradigm of Model Validation and Validated Models for Best-Estimate-Plus-Uncertainty Predictions in Systems Engineering,” Paper 200-01-1746 for Soc. Automotive Engineers 2007 World Congress April 16–20, Detroit, Michigan.

Romero et al. 2006, “Abnormal-Thermal QMU in Hydrocarbon and Propellant Fire Scenarios,”, ASC Level 2 QMU Milestone Review, Aug. 22, 2006, archived in Sandia ASC V&V Record and Document Management System (RMS), https://rmsprod.sandia.gov

Romero, V.J., M.P. Sherman, J.F. Dempsey, B.L. Bainbridge, V.G. Figueroa, M. Rajan, S.R. Tieszen, D. Dobranich, R.E. Hogan, M.L. Hobbs, W.W. Erikson, K.J. Dowding, J.C. Helton, C.A. Romero, S.S. Yoon, 2005a, “Advances in an Approach to QMU (Quantifying Margins and Uncertainty) applied to Weapon Safety in Abnormal Thermal Environments,” Sandia National Laboratories report SAND2005-1322 (OUO), printed June 2005

Romero, V.J., M.P. Sherman, J.F. Dempsey, J.D. Johnson, L.R. Edwards, K.C. Chen, R.V. Baron, C.F. King, 2005b,“Development and Validation of a Component Failure Model,” paper AIAA-2005-2141 presented at the 46th AIAA/ASME/ASCE/AHS/ASC Structures, Structural Dynamics, and Materials Conference, April 18-21, 2005, Austin, TX. Refined version with corrections available from the author at vjromer@sandia.gov

Romero, V., 2004,“Additional VULCAN runs for boundary condition uncertainty in QMU study” Sandia internal memo to A.R. Black, dated March 24, 2004, archived in Sandia ASCI V&V Record and Document Management System (RMS), https://rmsprod.sandia.gov

Romero, V.J., V.G. Figueroa, S.S. Yoon, J.M. Nelson, S.R. Tieszen, A.R. Black, 2003, “Uncertainty/Sensitivity Analysis of CFD Fire Modeling of Object Heating in Various Accident Scenarios,” draft Sandia National Laboratories report (2003). See also “Verification, Validation, and Uncertainty/Sensitivity Studies of Fire Modeling at Sandia National Laboratories,” V. Romero, A. Black, A. Brown, S. Tieszen, S. Domino, T. Blanchat, J. Nakos, A. Luketa-Hanlin, K. Dowding, V. Nicolette, M. Hobbs, in

proceedings CD of National Institute of Standards (NIST) Building and Fire Research Laboratory Annual Conference, Gaithersburg, MD, March 31 – April 2, 2008.

Siegel, R., and Howell, J., *Thermal Radiation Heat Transfer*, Taylor & Francis, 2002.

Tieszen, S. R., Black, A. R.., Nicolette, V. F., "Design of the W76-1 JT4A-14B1 Abnormal Thermal Qualification Test", Albuquerque, NM, SAND2007-6240.

Tieszen, S. R., Domino, S. P, Black, A. R., 2005, "Validation of a Simple Turbulence Model Suitable for Closure of Temporally-Filtered Navier-Stokes Equations Using a Helium Plume," Sandia National Laboratories, Albuquerque, NM, SAND2005-3210.

Worner, B., and G. Neuer, "Emittance measurements on steel during oxidation, *High Temperatures-High Pressures*, 1998, Vol. 15, p. 455-462.

Appendix A

Table A1: Values of thermal conductivities used in the simulations

Temperature (K)	Thermal Conductivity (W/K m^2)
Insulation	
273	**0.025**
400	**0.035**
600	**0.067**
800	**0.105**
1000	**0.145**
1200	**0.200**
1400	**0.250**
Steel (304)	
273	**13.4**
373	**16.3**
773	**21.8**
973	**26.0**

Appendix B. **Presentation of Raw Simulation Results**

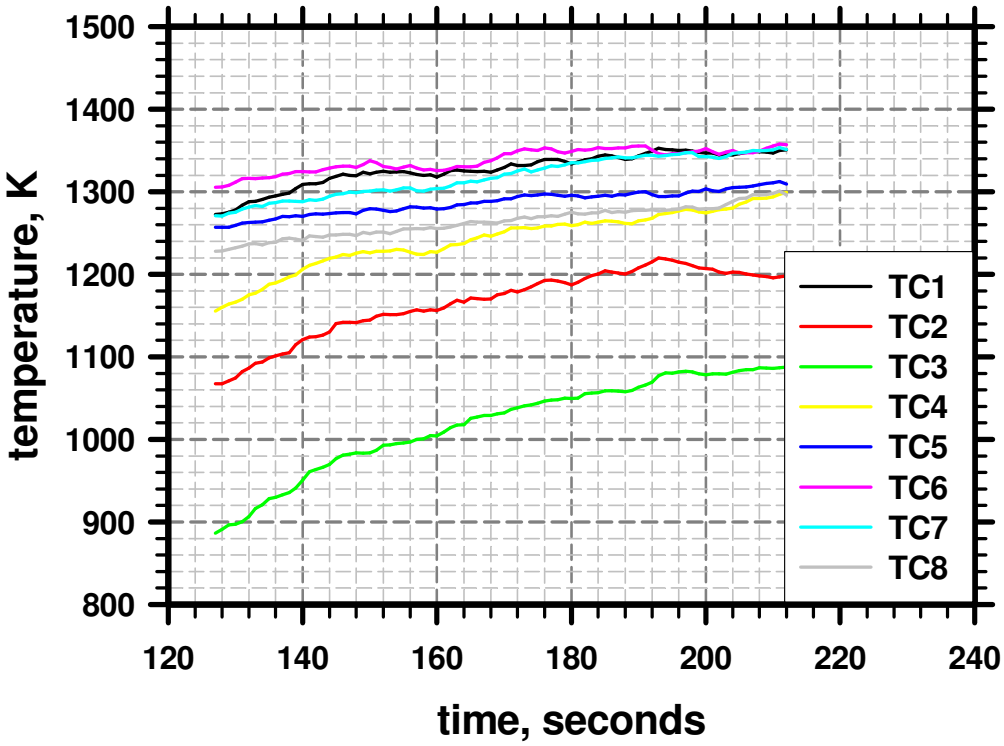

Figure B1: Simulated TC responses for Simulation # 1

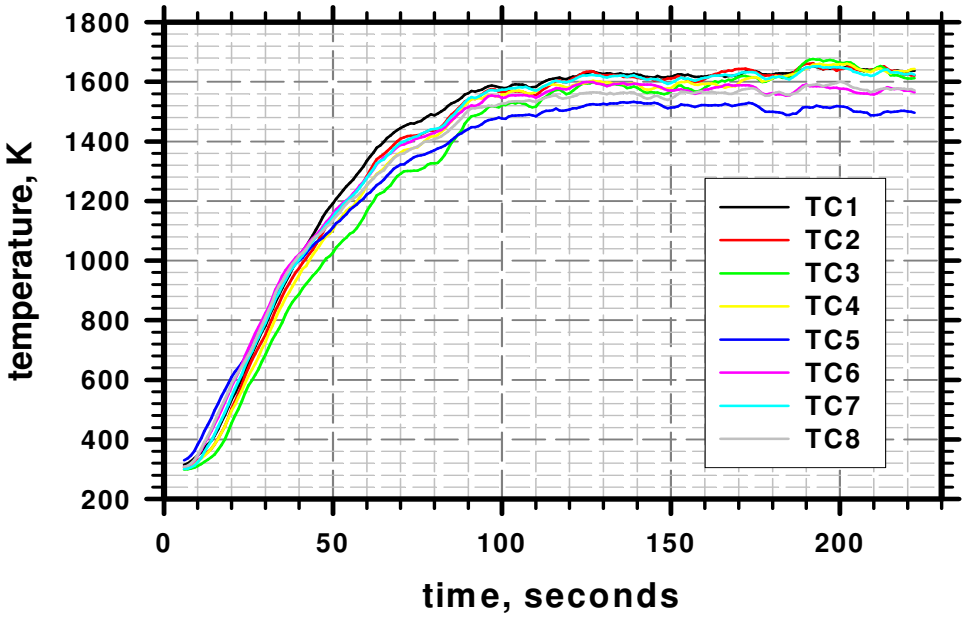

Figure B2: Simulated TC responses for Simulation # 2

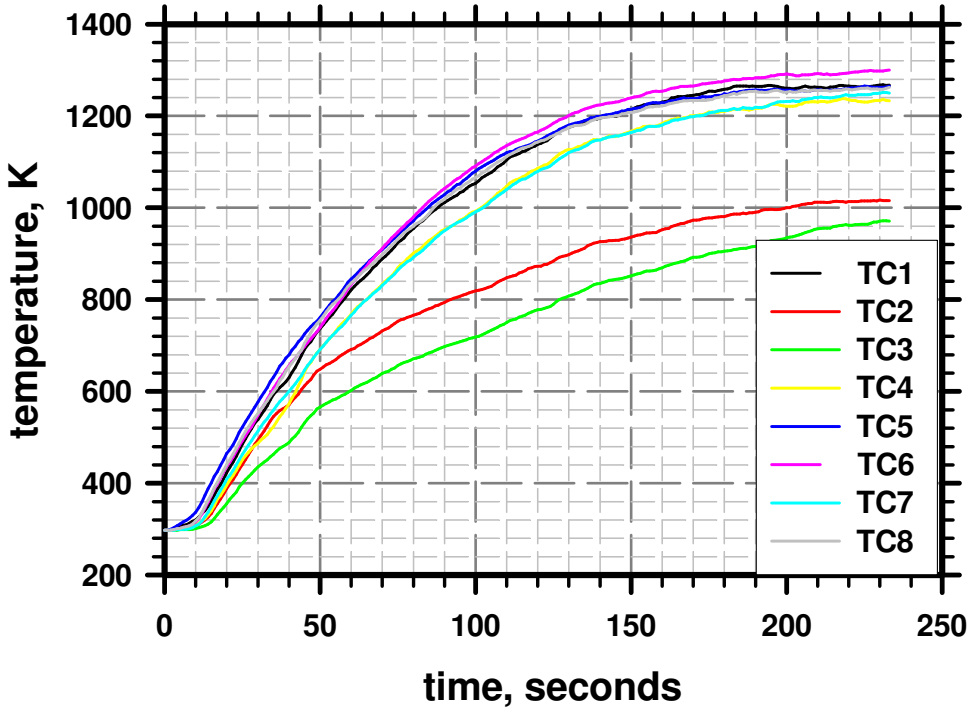

Figure B3:. Simulated TC responses for Simulation # 3

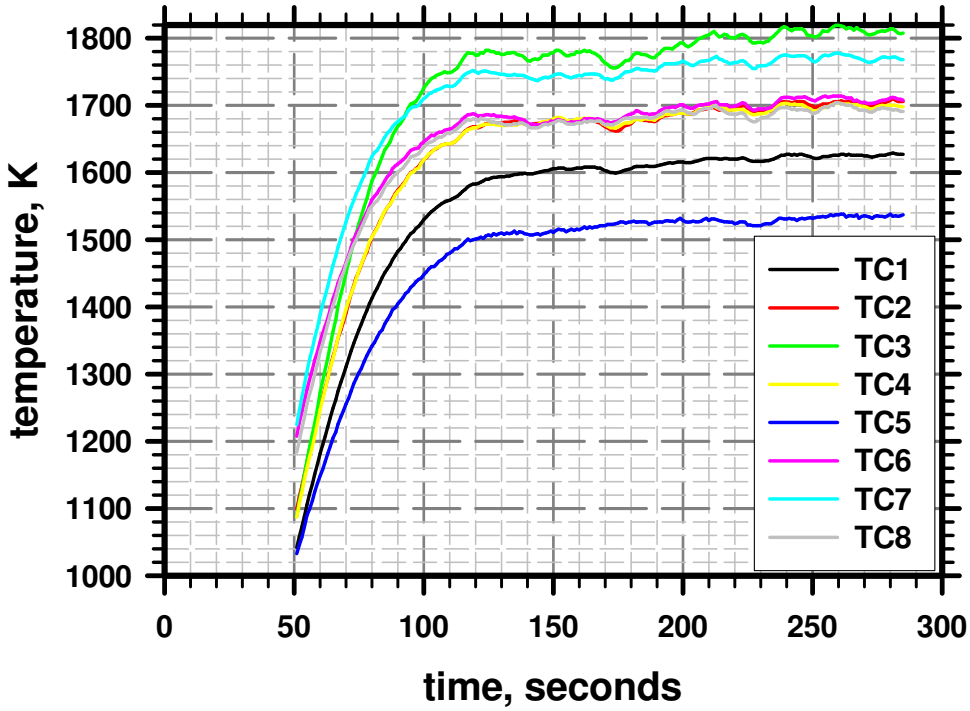

Figure B4: Simulated TC responses for Simulation # 4

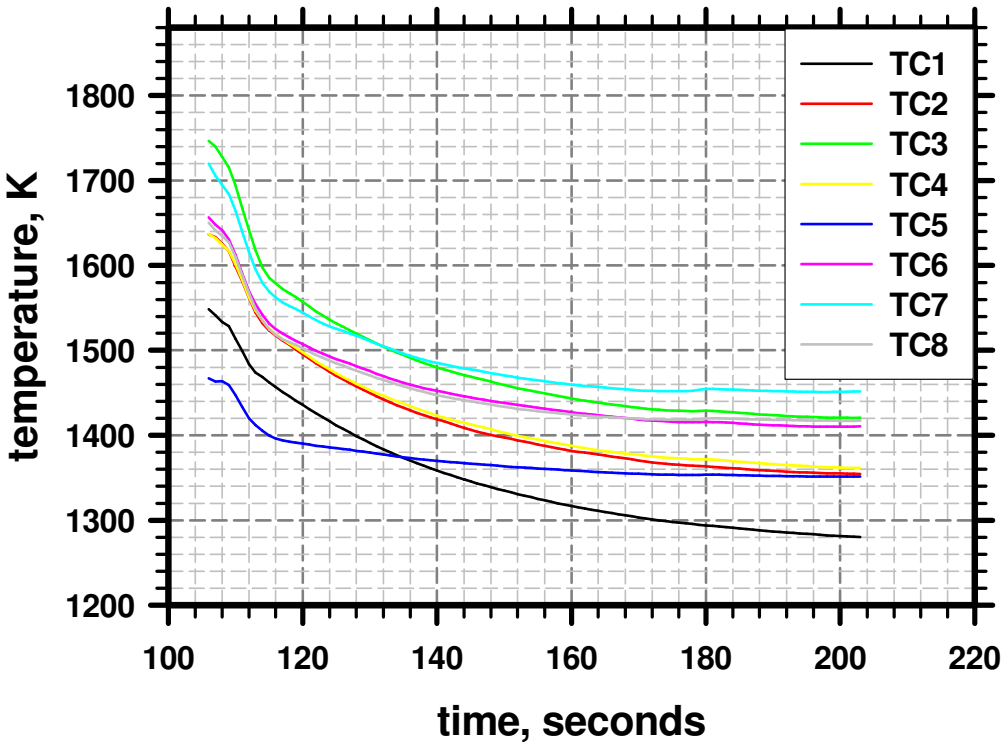

Figure B5: Simulated TC responses for Simulation # 5

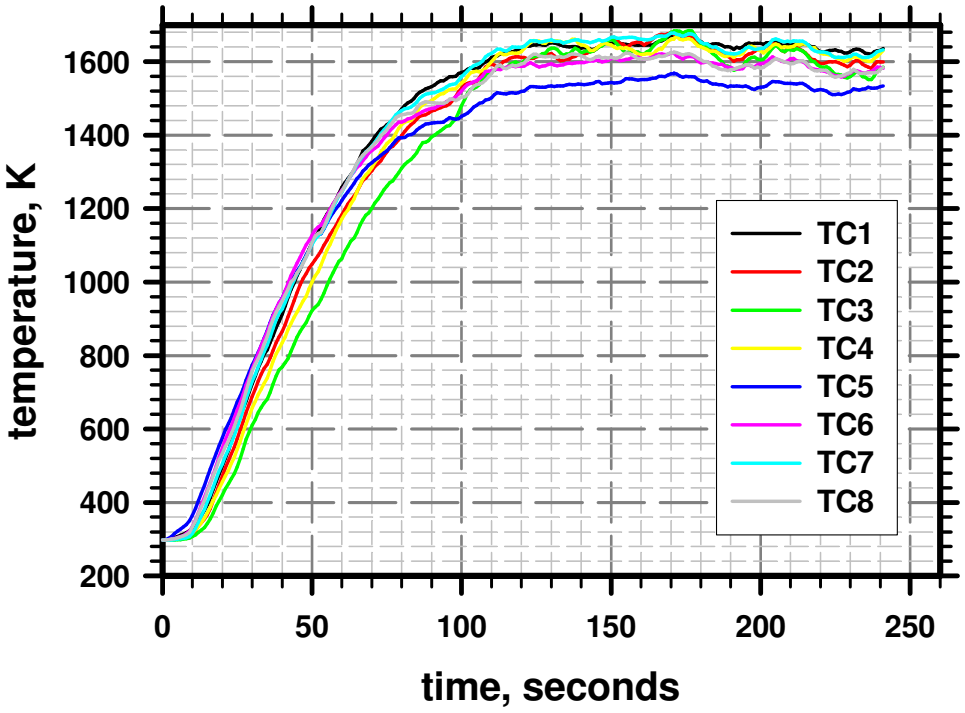

Figure B6: Simulated TC responses for Simulation # 6

Appendix C. Raw Experiment & Sim. Results grouped by TC#

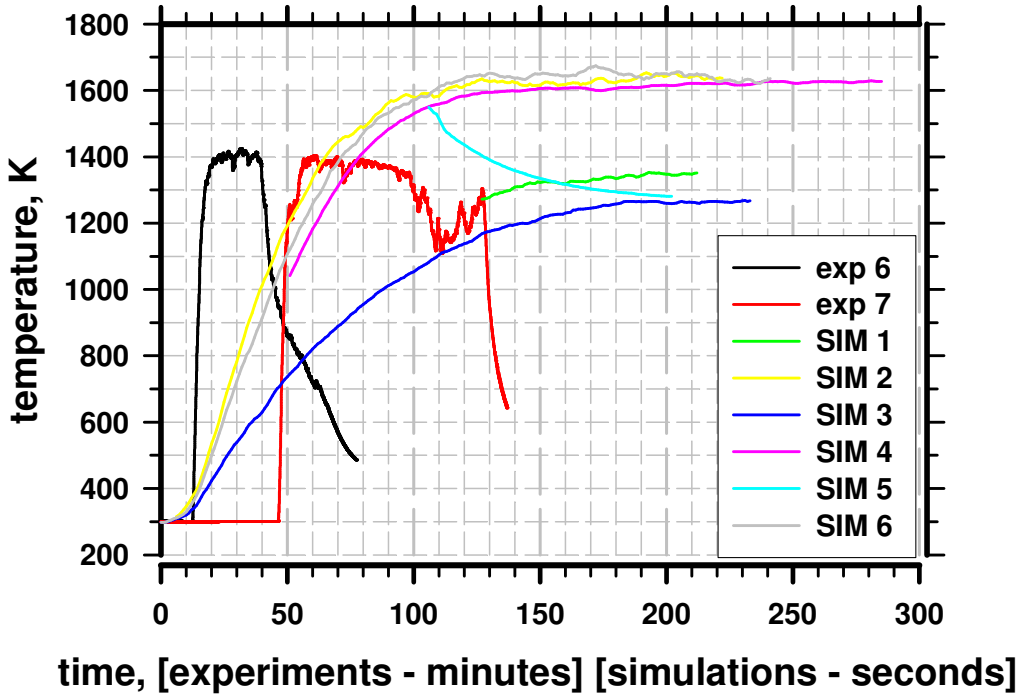

Figure C1: Calorimeter Temperature at TC #1 bottom - 0

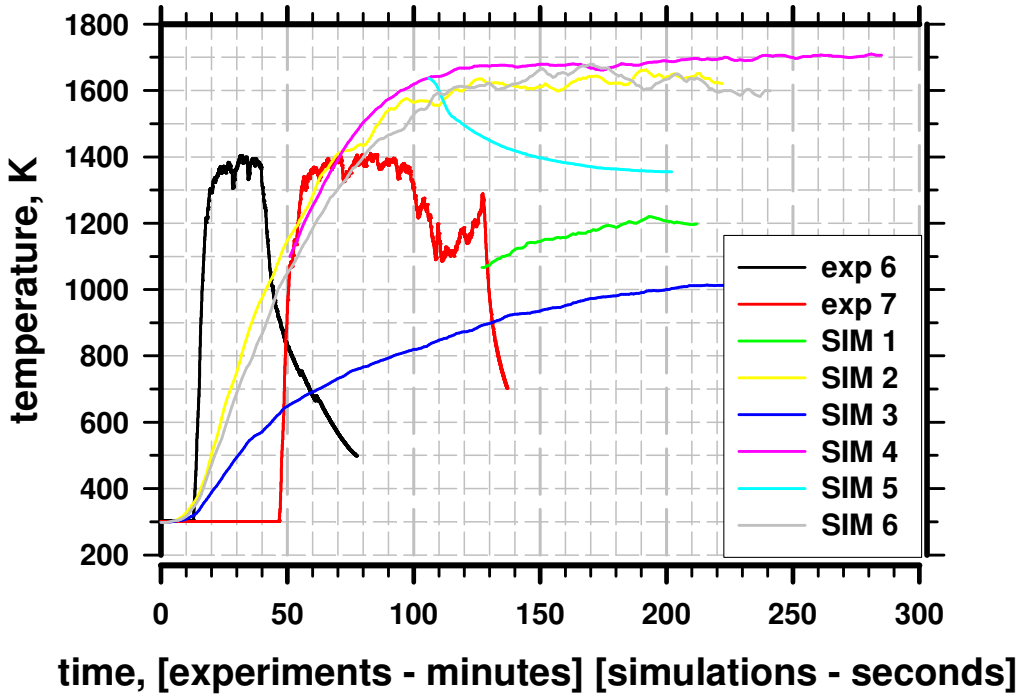

Figure C2: Calorimeter Temperature at TC #2 bottom - 90

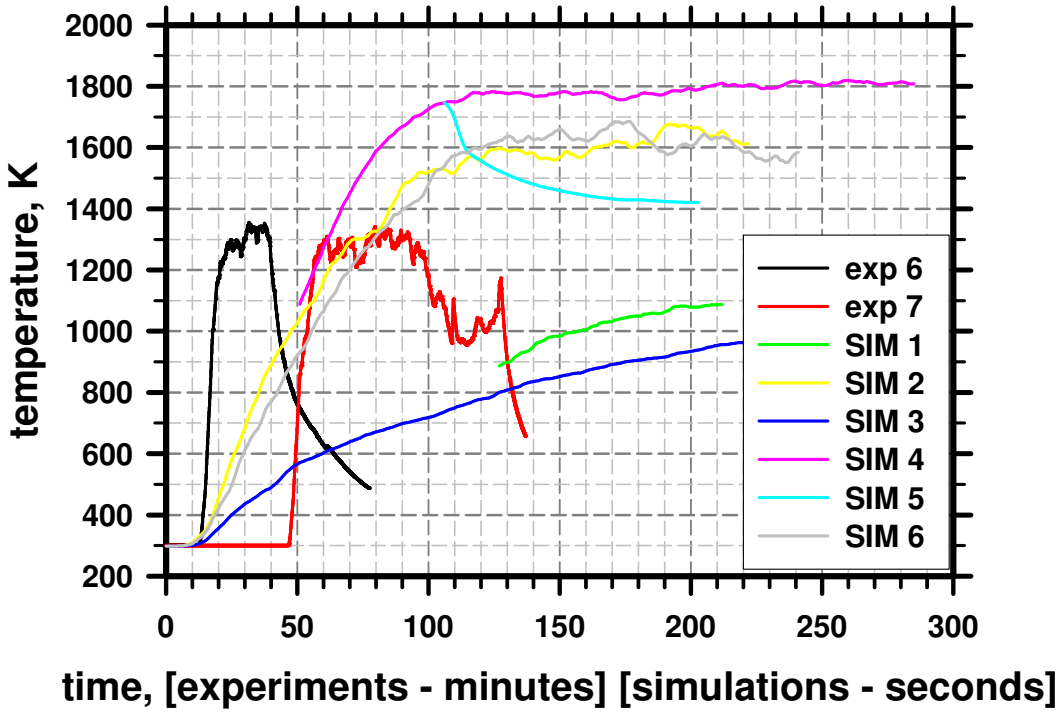

Figure C3: Calorimeter Temperature at TC #3 bottom - 180

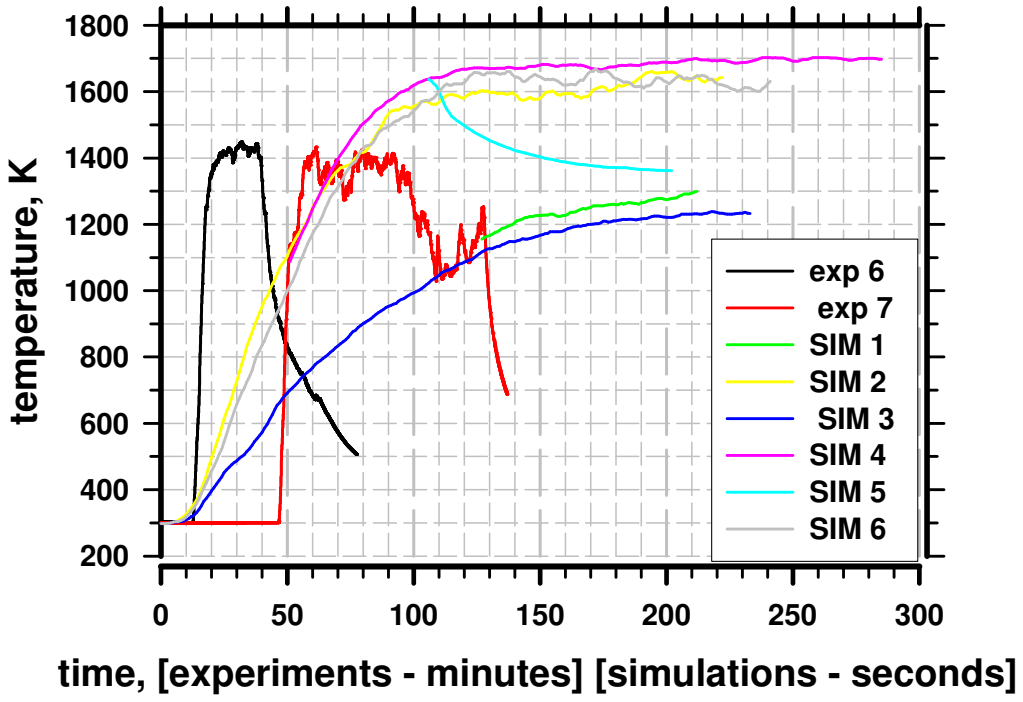

Figure C4: Calorimeter Temperature at TC #4 bottom - 270

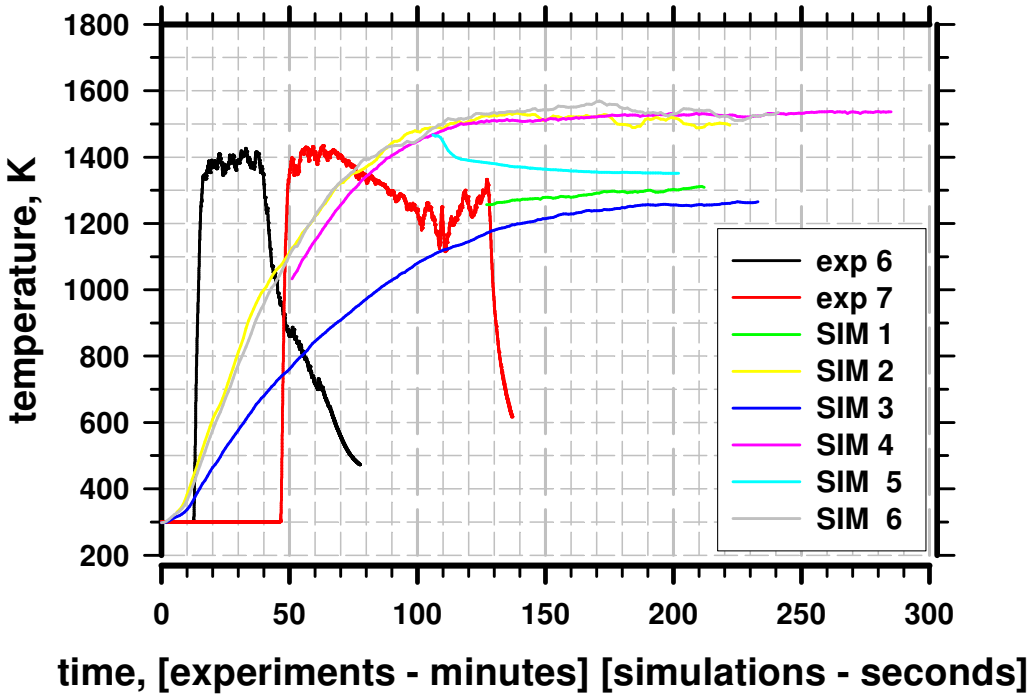

Figure C5: Calorimeter Temperature at TC #5 top - 0

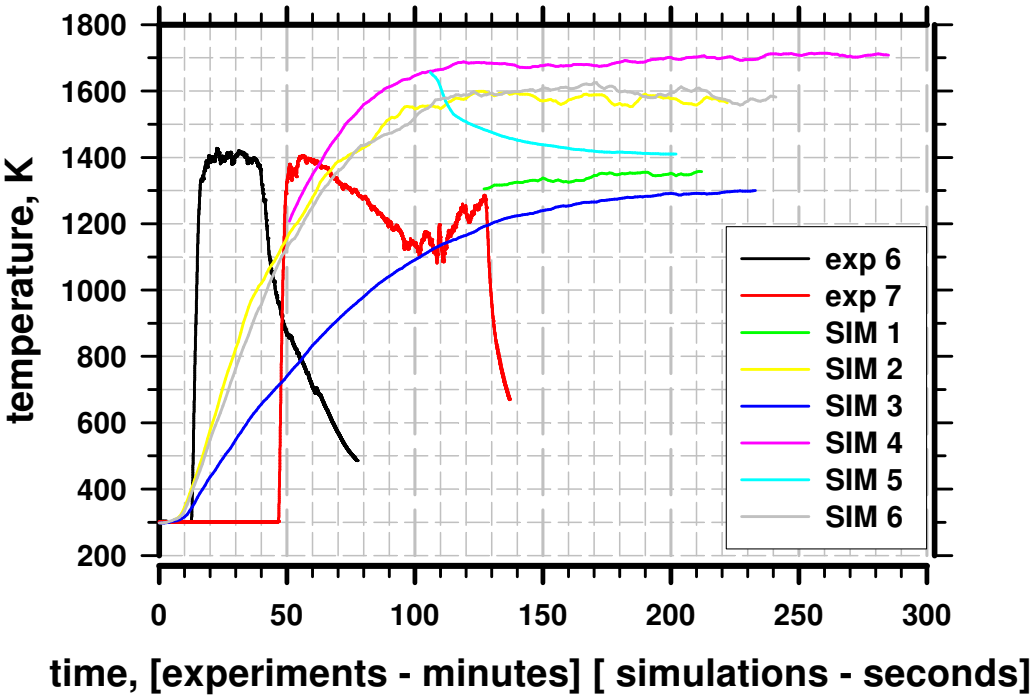

Figure C6: Calorimeter Temperature at TC #6 top - 90

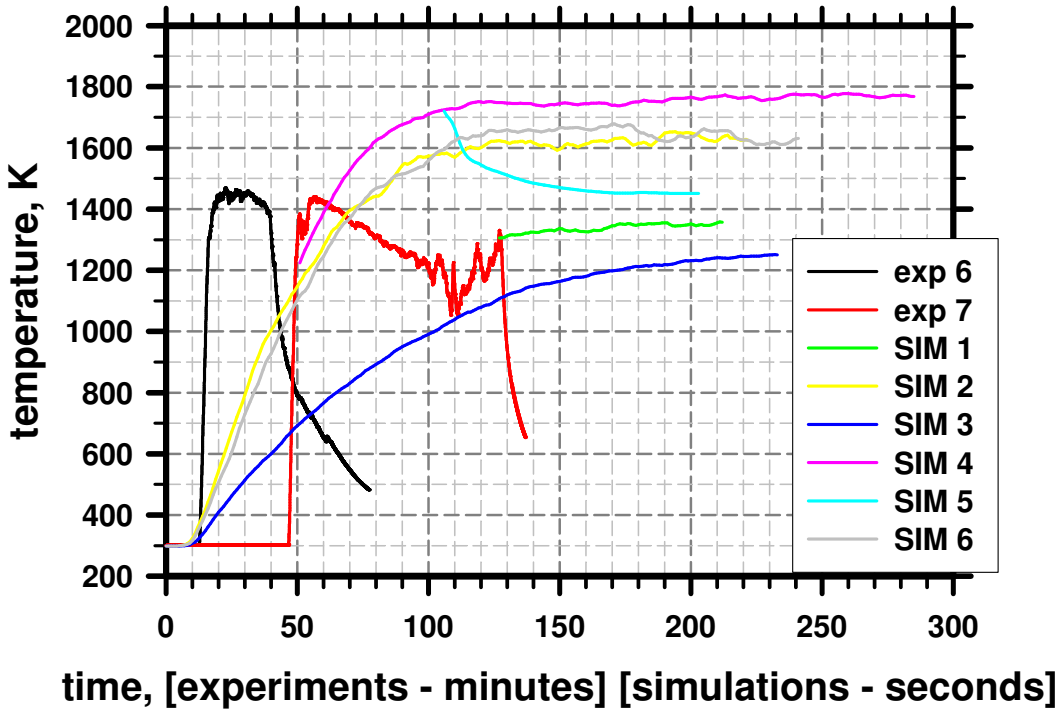

Figure C7: Calorimeter Temperature at TC #7 top - 180

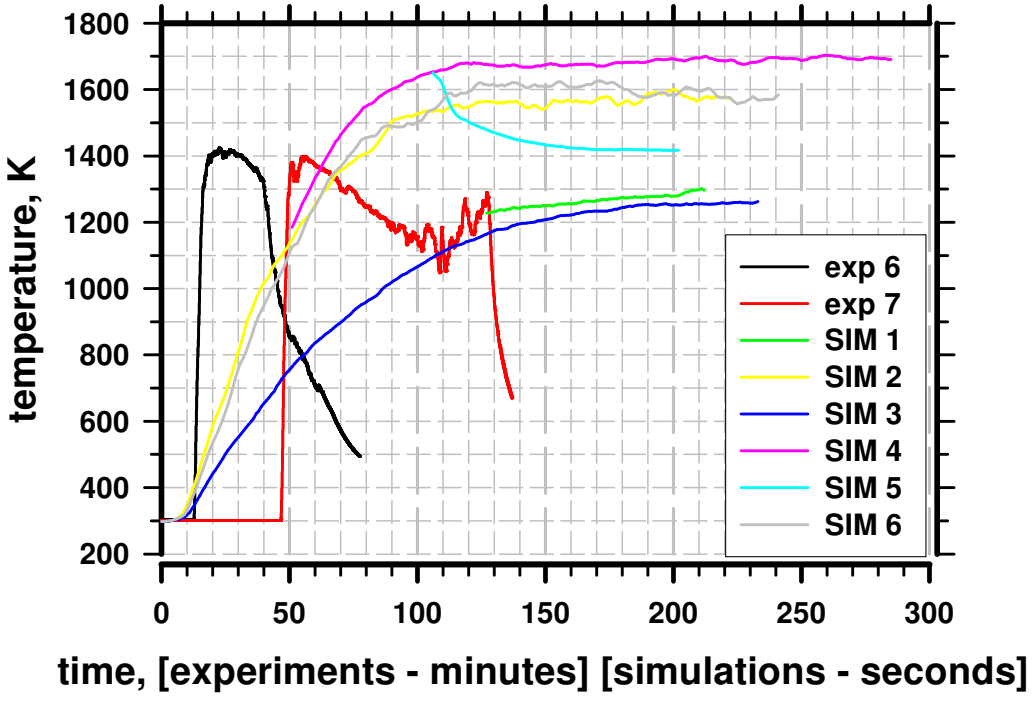

Figure C8: Calorimeter Temperature at TC #8 top - 270

Appendix D. Uncertainty on Experimental & Simulation Steady-State Temperature at each TC

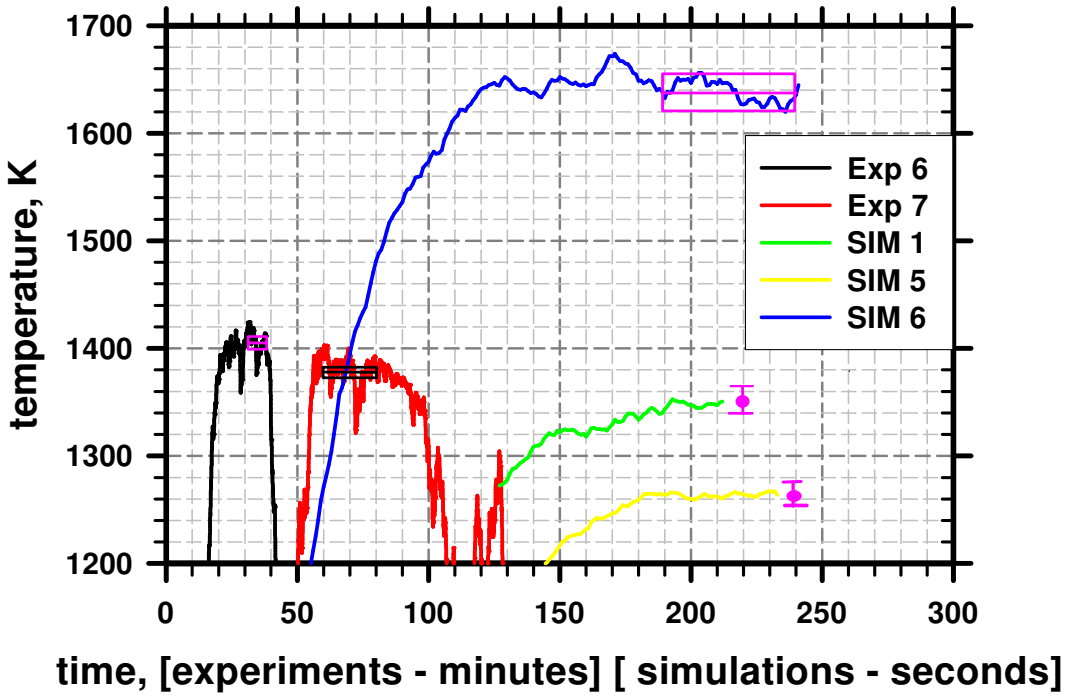

Figure D1: Thermocouple TC1 - uncertainty on steady state values

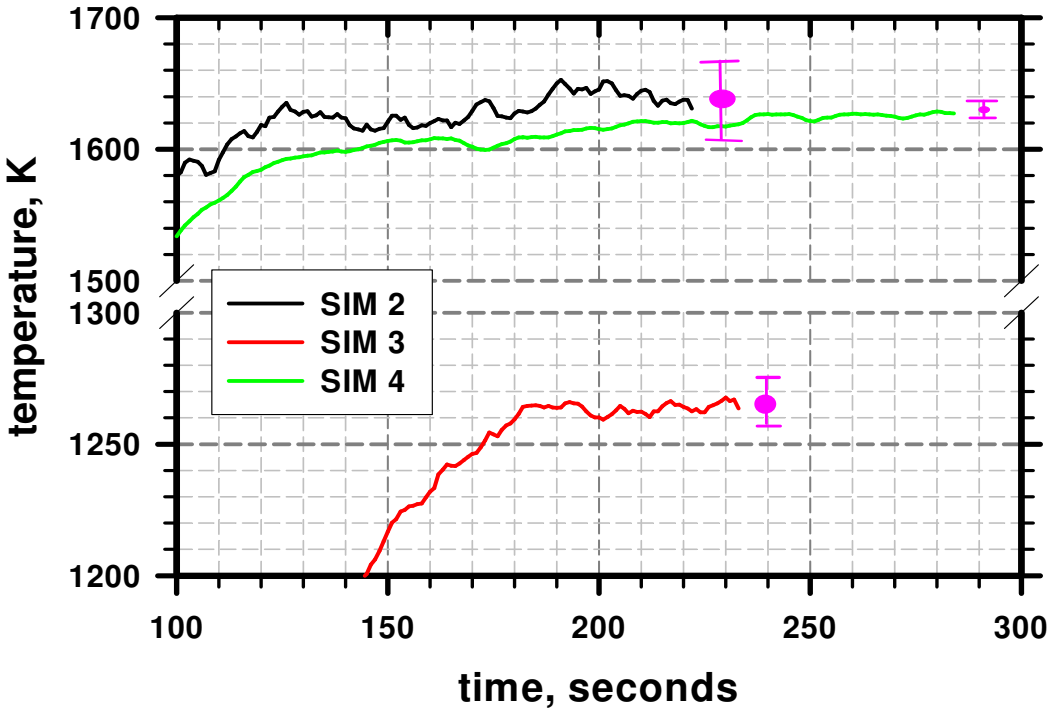

Figure D2: Thermcouple TC1 – uncertainty on steady state values

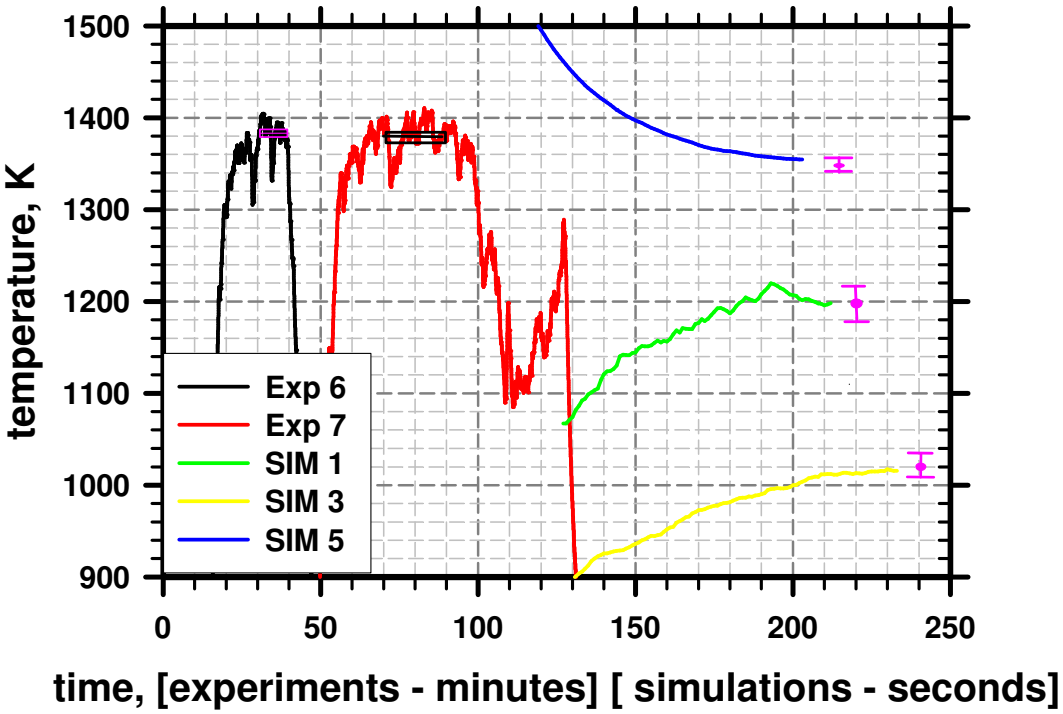

Figure D3: Thermocouple TC2 - uncertainty on steady state values

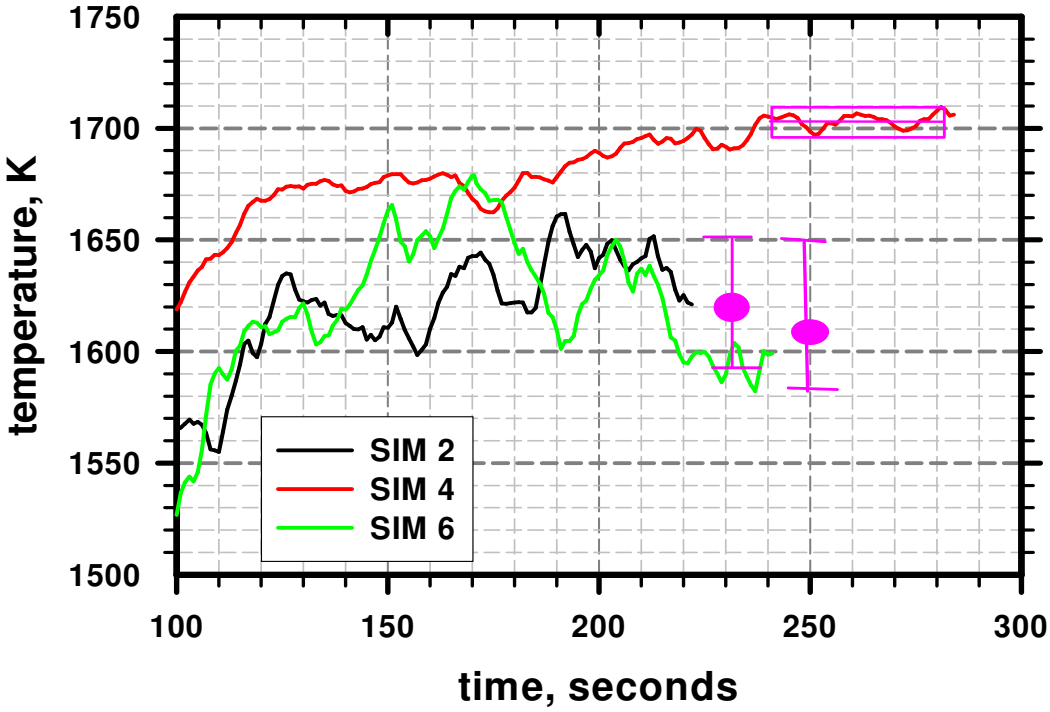

Figure D4: Thermocouple TC2 - uncertainty on steady state values

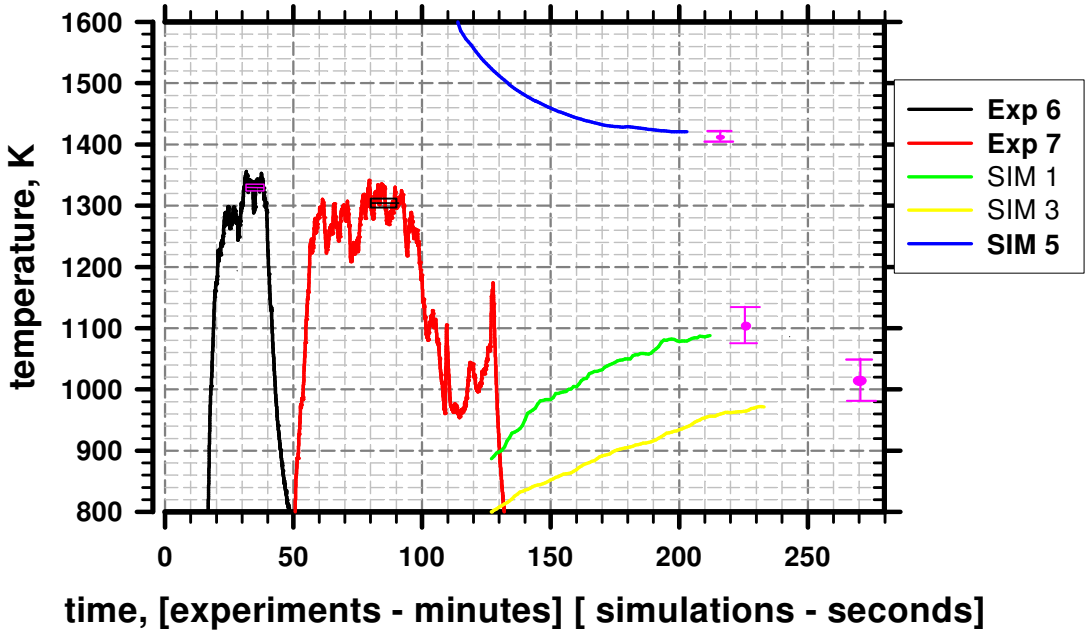

Figure D5: Thermocouple TC3 - uncertainty on steady state values

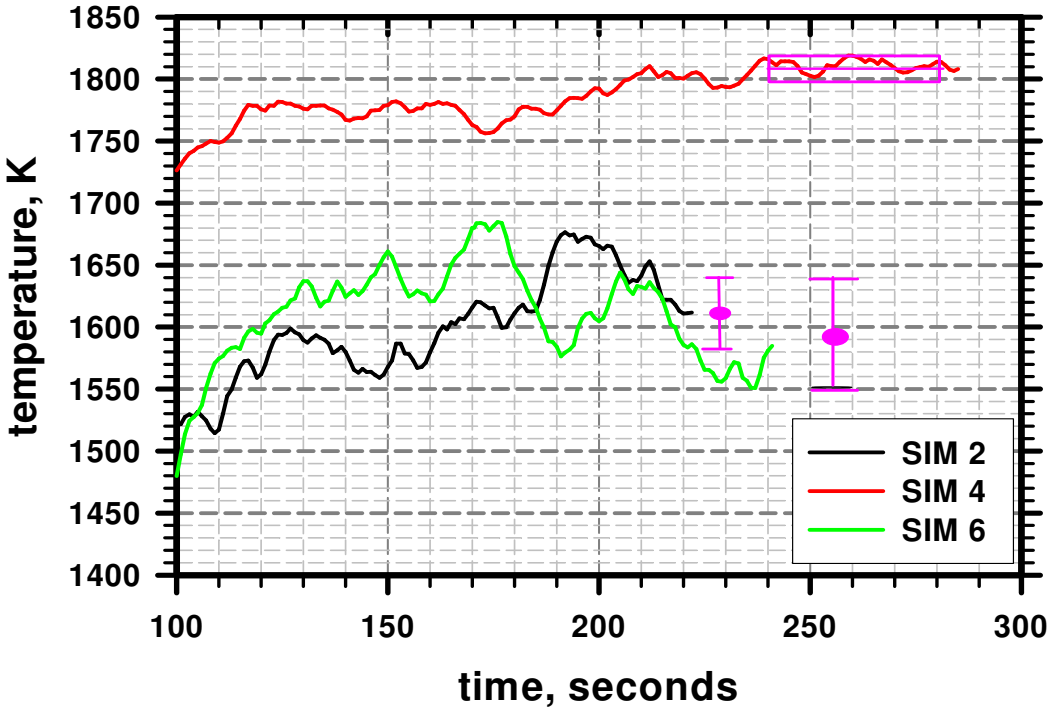

Figure D6: Thermocouple TC3 - uncertainty on steady state values

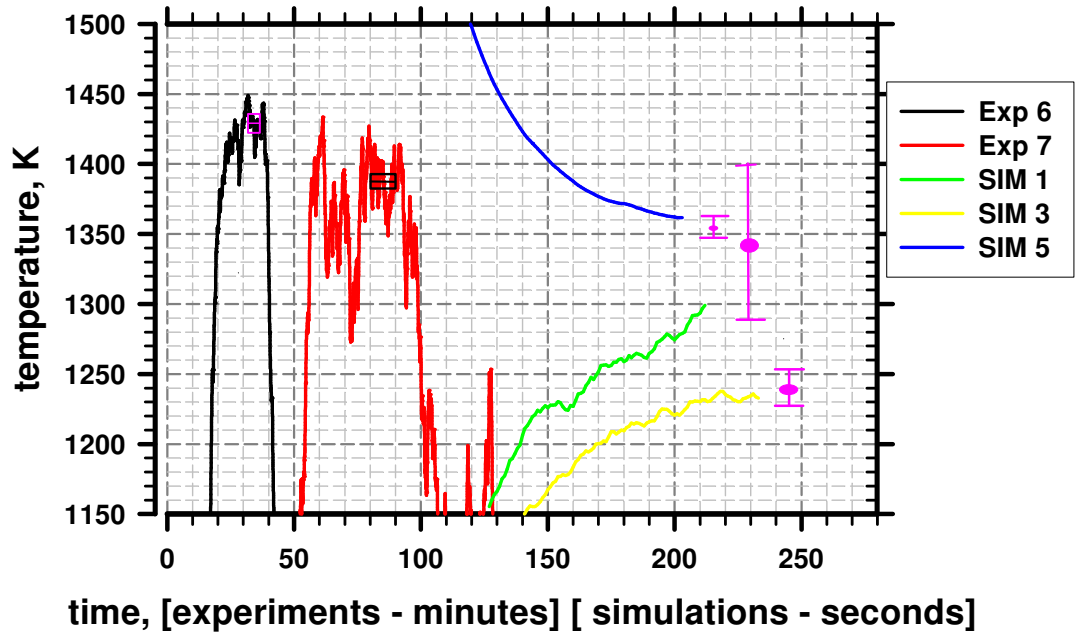

Figure D7: Thermocouple TC4 - uncertainty on steady state values

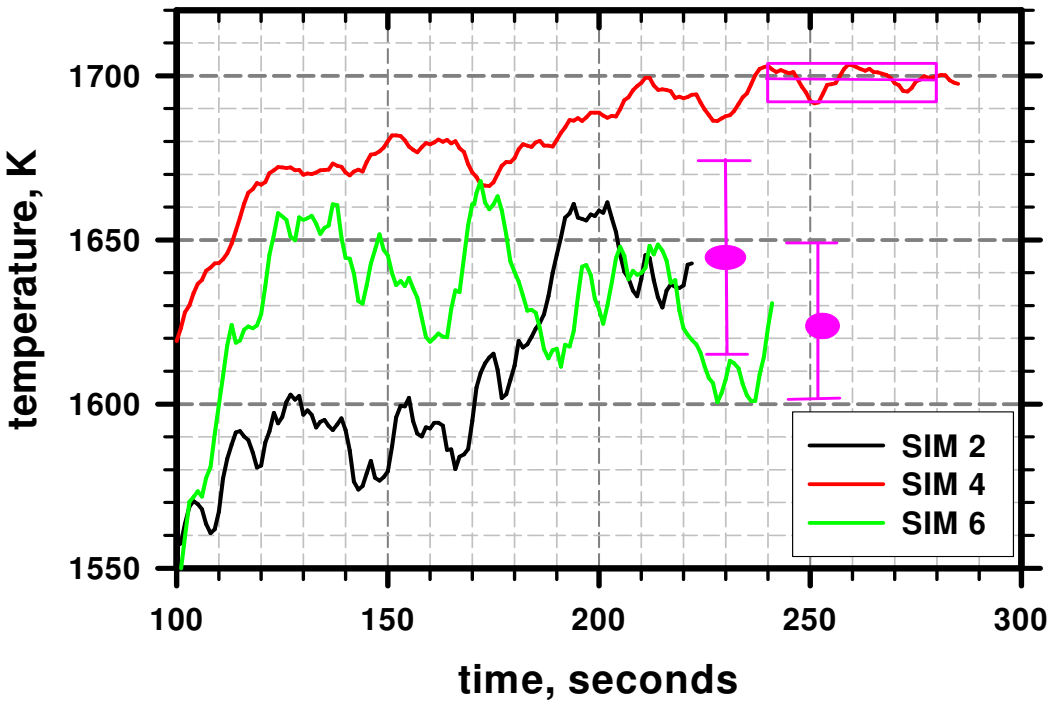

Figure D8: Thermocouple TC4 - uncertainty on steady state values

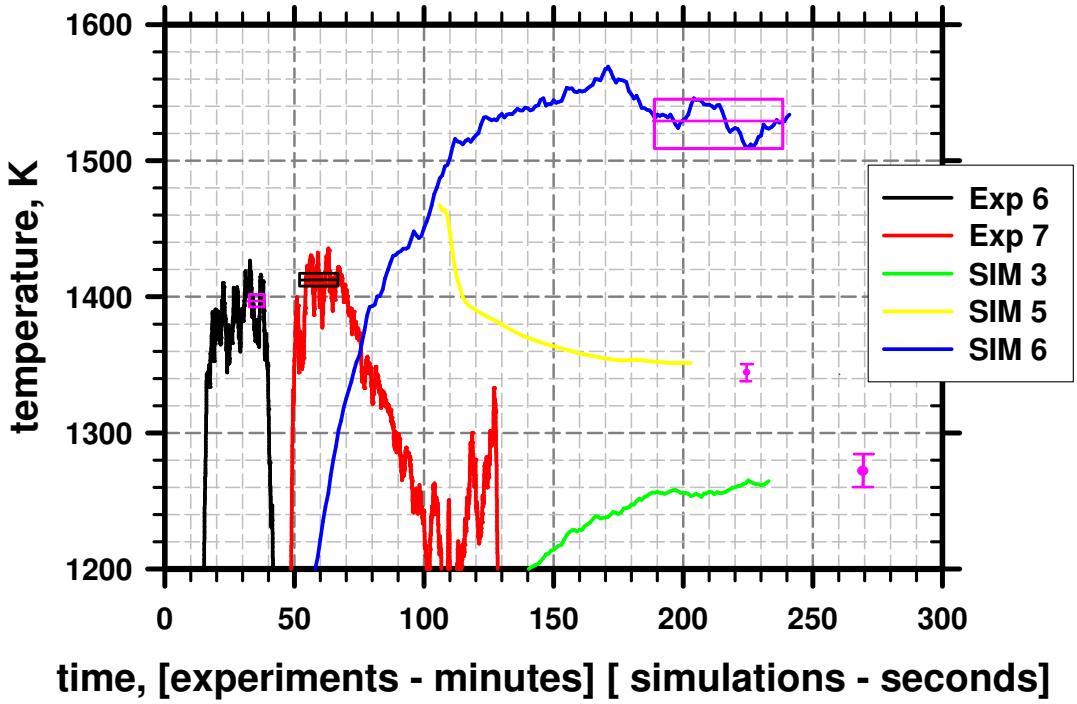

Figure D9: Thermocouple TC5 - uncertainty on steady state values

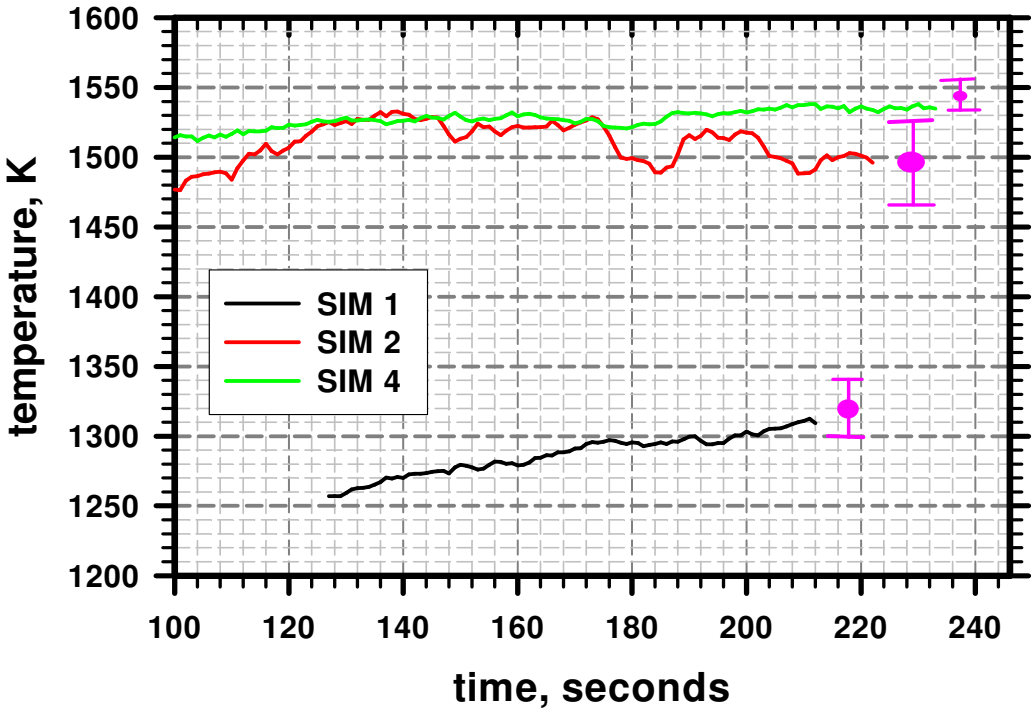

Figure D10: Thermocouple TC5 - uncertainty on steady state values

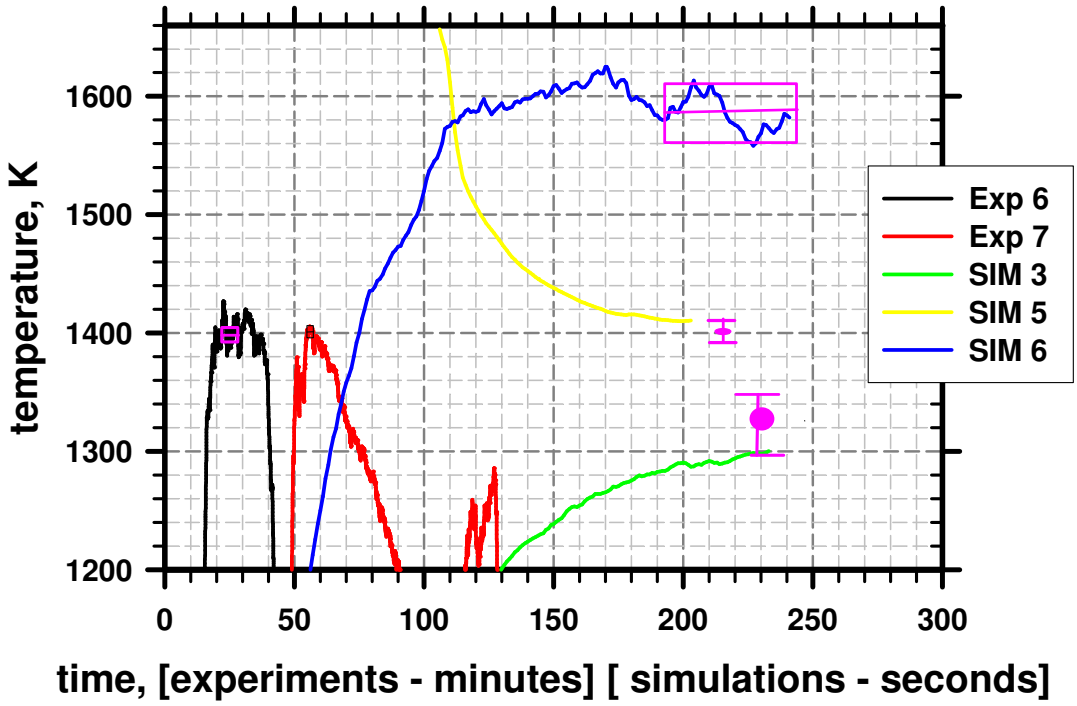

Figure D11: Thermocouple TC6 - uncertainty on steady state values

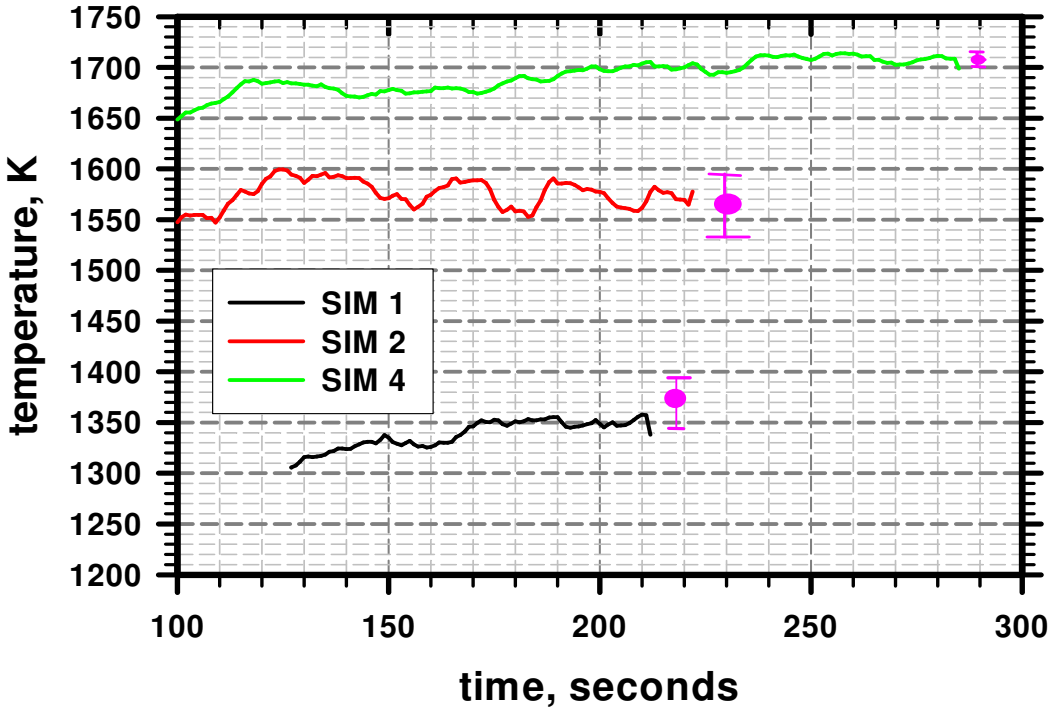

Figure D12: Thermocouple TC6 - uncertainty on steady state values

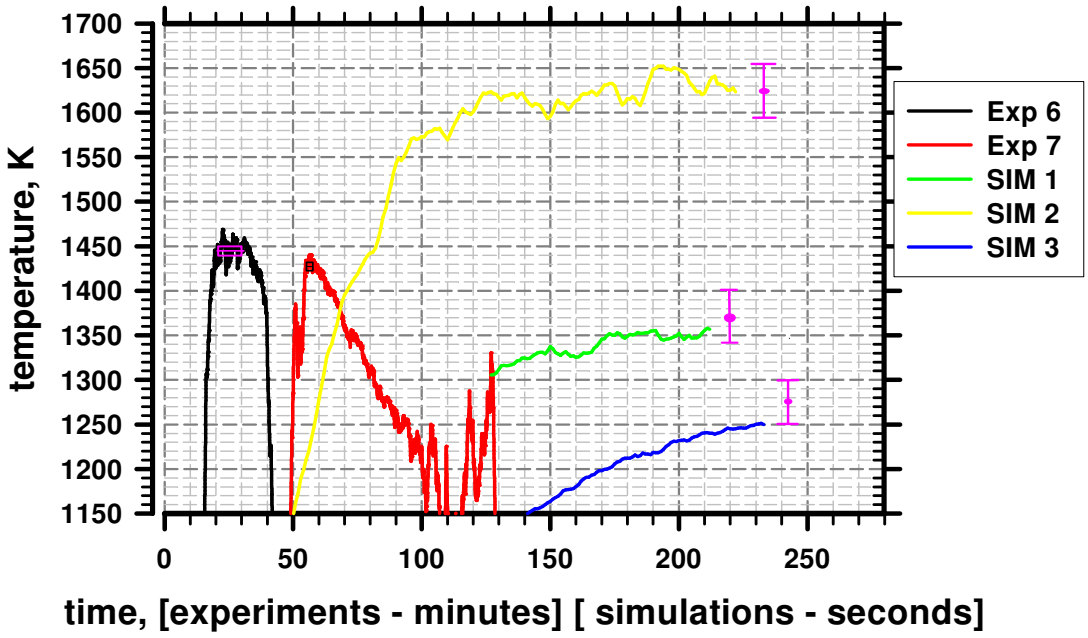

Figure D13: Thermocouple TC7 - uncertainty on steady state values

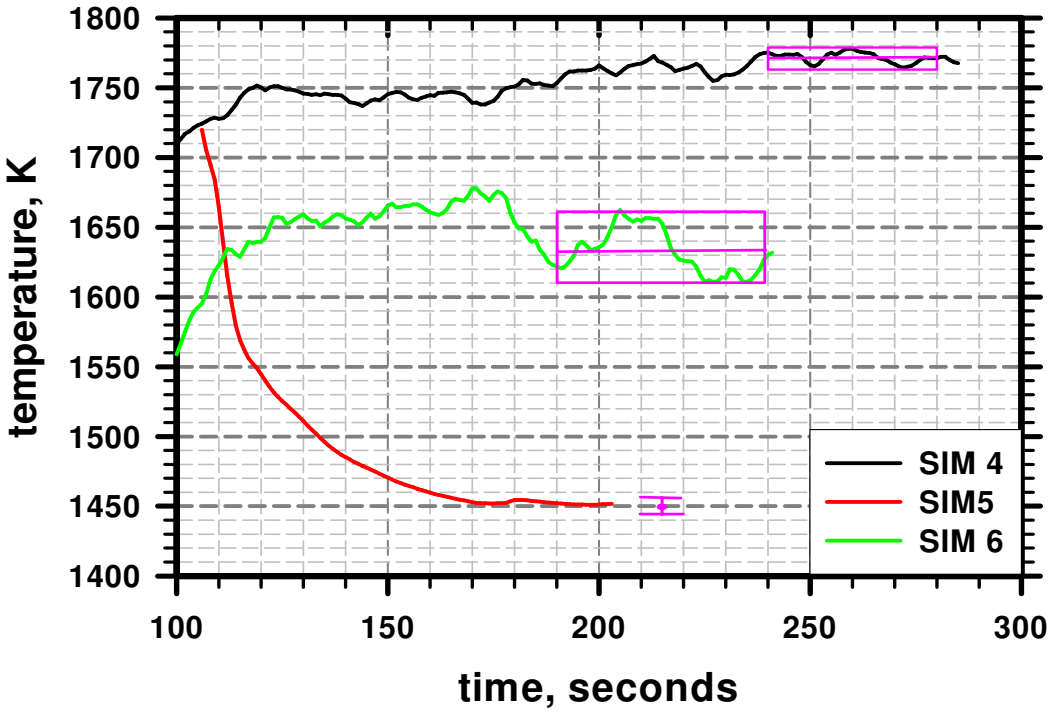

Figure D14: Thermocouple TC7 - uncertainty on steady state values

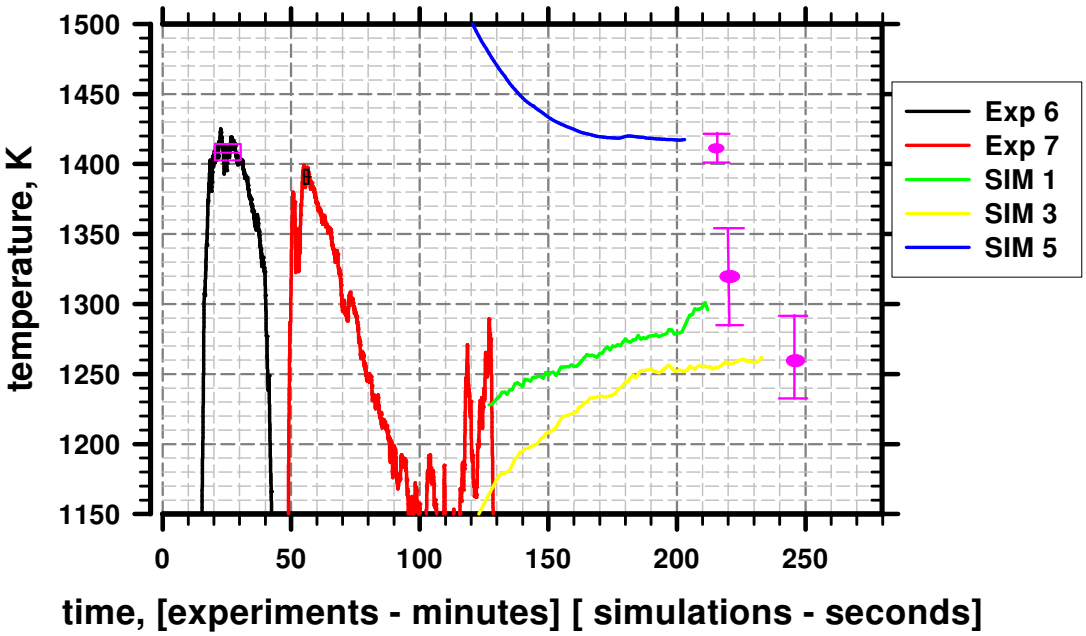

Figure D15: Thermocouple TC8 - uncertainty on steady state values

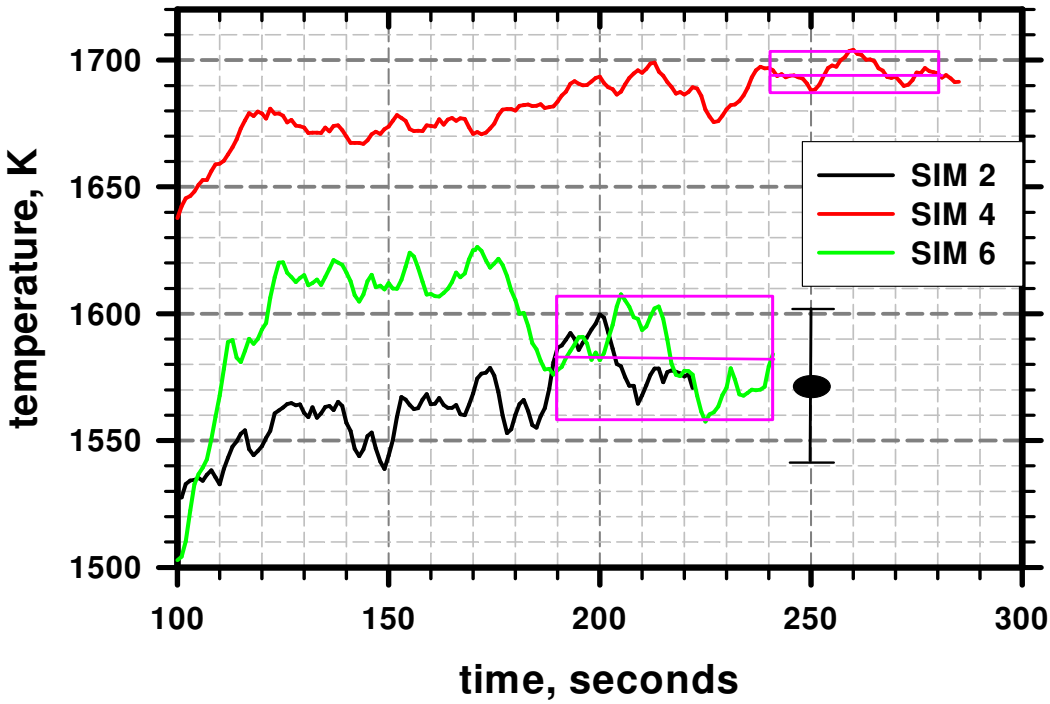

Figure D16: Thermocouple TC8 - uncertainty on steady state values

Appendix E

Table E1. Summary Processing Results for Experimental and Simulation Uncertainty Quantification

Experiment 6	TC1	TC2	TC3	TC4	TC5	TC6	TC7	TC8
Max. over window (K)	1421.79	1402.82	1352.48	1447.38	1426.7	1415.86	1469.12	1425.22
Min. over window (K)	1374.98	1331.37	1288.2	1404.68	1363.23	1380.91	1417.8	1392.61
Mean (K)	1403.5	1381.6	1329.8	1428.0	1394.1	1397.5	1444.8	1408.9
(Mean ℃) x 1%	11.3	11.1	10.6	11.5	11.2	11.2	11.7	11.4

Experiment 7	TC1	TC2	TC3	TC4	TC5	TC6	TC7	TC8
Max. over window (K)	1402.92	1410.52	1335.53	1413.96	1435.58	1405.59	1433.94	1399.01
Min. over window (K)	1321.08	1324.64	1269.08	1348.57	1377.31	1396.89	1420.96	1383.01
Mean (K)	1378.0	1379.4	1303.8	1385.6	1411.8	1401.2	1428.5	1391.2
(Mean ℃) x 1%	11.0	11.1	10.3	11.1	11.4	11.3	11.6	11.2

avgerage and standard deviation of the two steady-states (mean values) for Experiments 6 and 7

	TC1	TC2	TC3	TC4	TC5	TC6	TC7	TC8
avg., mu (K)	1390.8	1380.5	1316.8	1406.8	1402.9	1399.4	1436.6	1400.1
stdev., S (K)	18.04985	1.564696	18.3618	29.95486	12.49365	2.632013	11.56442	12.51394
2S (K)	36.1	3.1	36.7	59.9	25.0	5.3	23.1	25.0
2Shigh (K)	50.2	17.3	50.9	74.1	39.1	19.4	37.3	39.2

Uncertainty due to emis.

SIM 6	TC1	TC2	TC3	TC4	TC5	TC6	TC7	TC8
Mean (K)	1638	1613	1594	1625	1529	1584	1632	1582
SIM 2	TC1	TC2	TC3	TC4	TC5	TC6	TC7	TC8
Midway (K)	1637	1621	1612	1643	1496	1565	1624	1571
mu6 - mu2 (K)	1.1	-8.3	-17.3	-17.4	33.2	19.8	8.8	11.4
2X for exp. data condit.	2.1	-16.6	-34.5	-34.9	66.4	39.6	17.6	22.8
(avoid Type X val. error)								
aggregate experimental	63.5	45.0	95.8	120.3	116.8	70.3	66.5	73.2

Appendix F

Table F1. Last reported values of simulated temperatures, with mean or extrapolated-asymptotic steady-state values and uncertainty bounds

SIM 1	TC1	TC2	TC3	TC4	TC5	TC6	TC7	TC8
last	1351	1198	1088	1299	1309	1357	1351	1296
max	1361	1218	1138	1399	1339	1397	1401	1356
min	1341	1178	1078	1289	1299	1347	1341	1286
midway	1351	1198	1108	1344	1319	1372	1371	1321

SIM 2	TC1	TC2	TC3	TC4	TC5	TC6	TC7	TC8
last	1637	1621	1612	1643	1496	1565	1624	1571
max	1667	1651	1642	1673	1526	1595	1654	1601
min	1607	1591	1582	1613	1466	1535	1594	1541
midway	1637	1621	1612	1643	1496	1565	1624	1571

SIM 3	TC1	TC2	TC3	TC4	TC5	TC6	TC7	TC8
last	1267	1016	971	1233	1265	1300	1250	1262
max	1277	1036	1051	1253	1285	1350	1300	1292
min	1257	1011	981	1228	1260	1300	1250	1232
midway	1267	1023	1016	1240	1273	1325	1275	1262

SIM 4	TC1	TC2	TC3	TC4	TC5	TC6	TC7	TC8
last	1627	1706	1808	1698	1537	1708	1768	1691
max	1637	1708	1819	1703	1557	1714	1778	1704
min	1622	1697	1802	1692	1532	1703	1764	1688
mean/midway	1630	1703	1811	1699	1545	1710	1772	1695

SIM 5	TC1	TC2	TC3	TC4	TC5	TC6	TC7	TC8
last	1280	1355	1421	1362	1352	1410	1452	1417
max	1275	1355	1421	1362	1352	1410	1457	1422
min	1250	1340	1406	1347	1337	1395	1442	1402
midway	1263	1347	1413	1354	1345	1403	1449	1412

SIM 6	TC1	TC2	TC3	TC4	TC5	TC6	TC7	TC8
last	1636	1599	1585	1631	1534	1582	1632	1584
maximum	1656	1650	1644	1649	1546	1613	1662	1608
minimum	1620	1582	1551	1601	1510	1558	1611	1557
mean	1638	1613	1594	1625	1529	1584	1632	1582

Appendix G. Graphically Processed Steady-State Temperatures and Associated Uncertainty—Min., Max., and Mean or Midpoint Results

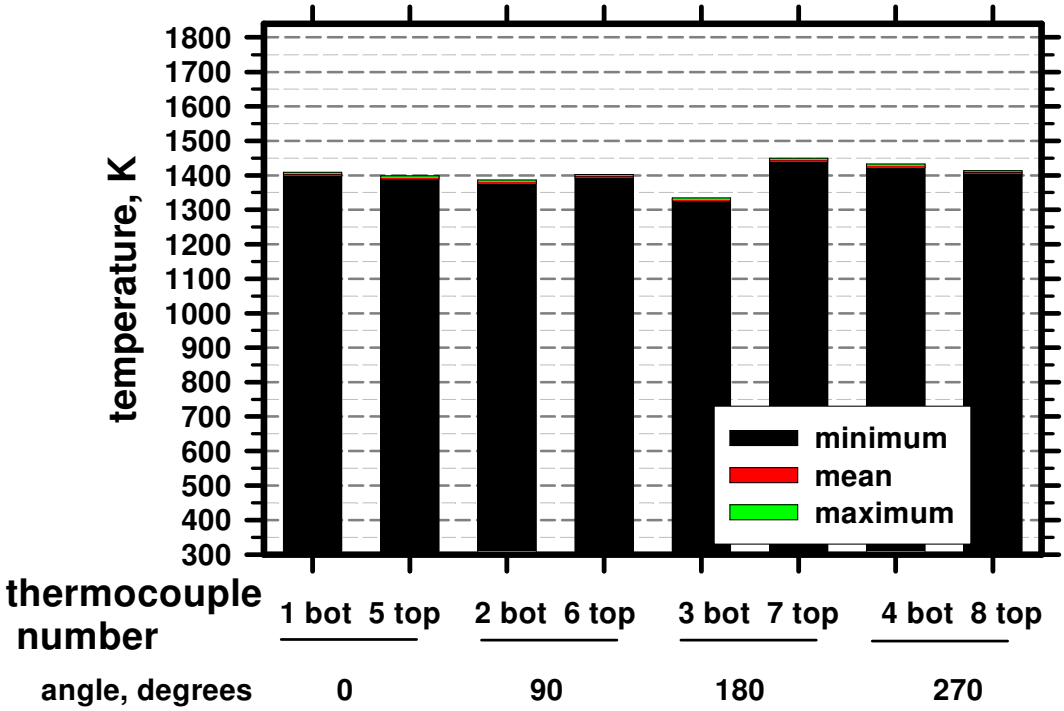

Figure G1: Min., midpoint, and max. steady state temperatures for Exp. 6

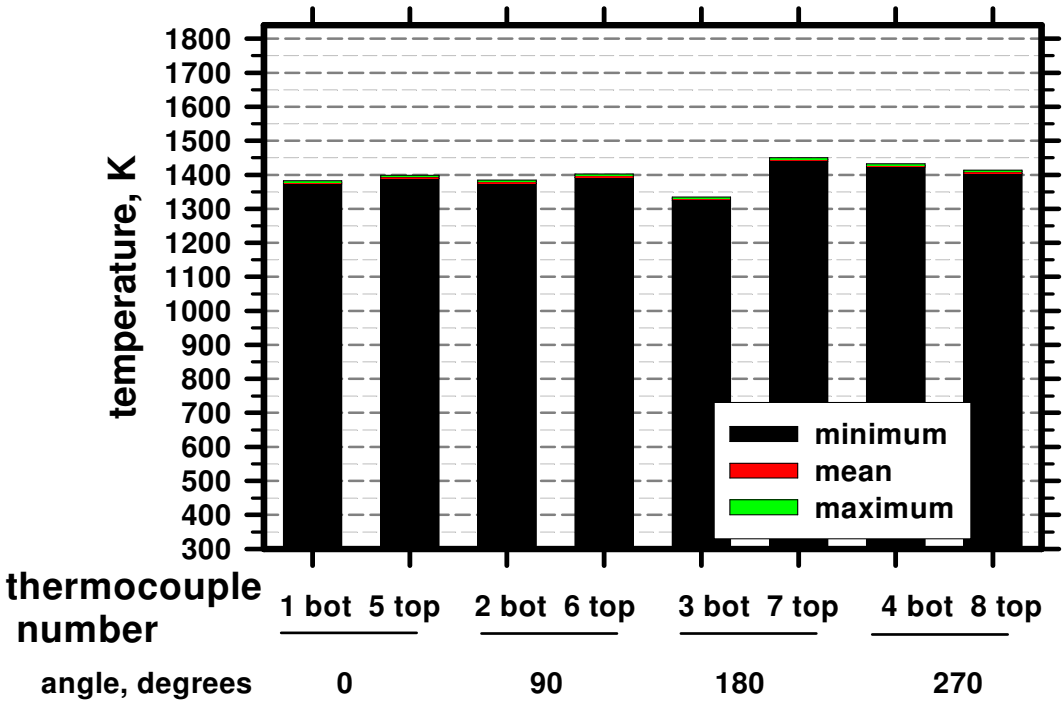

Figure G2: Min., midpoint, and max. steady state temperatures for Exp. 7.

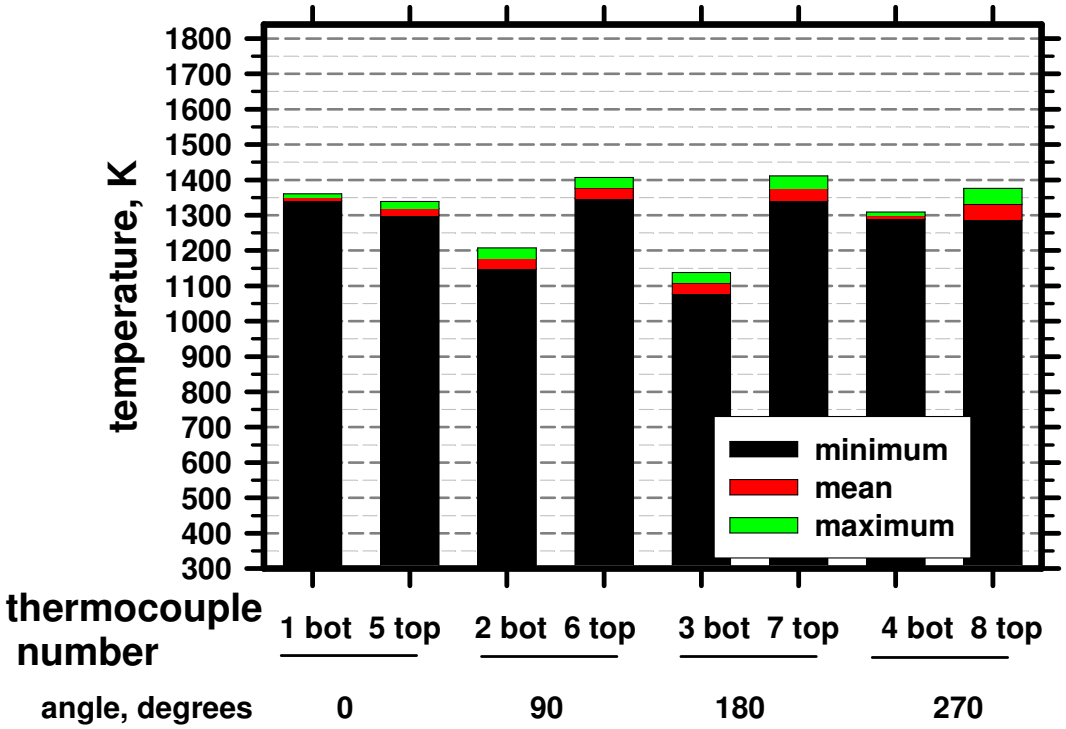

Figure G3: Minimum, midpoint, and maximum steady state temperatures for simulation #1.

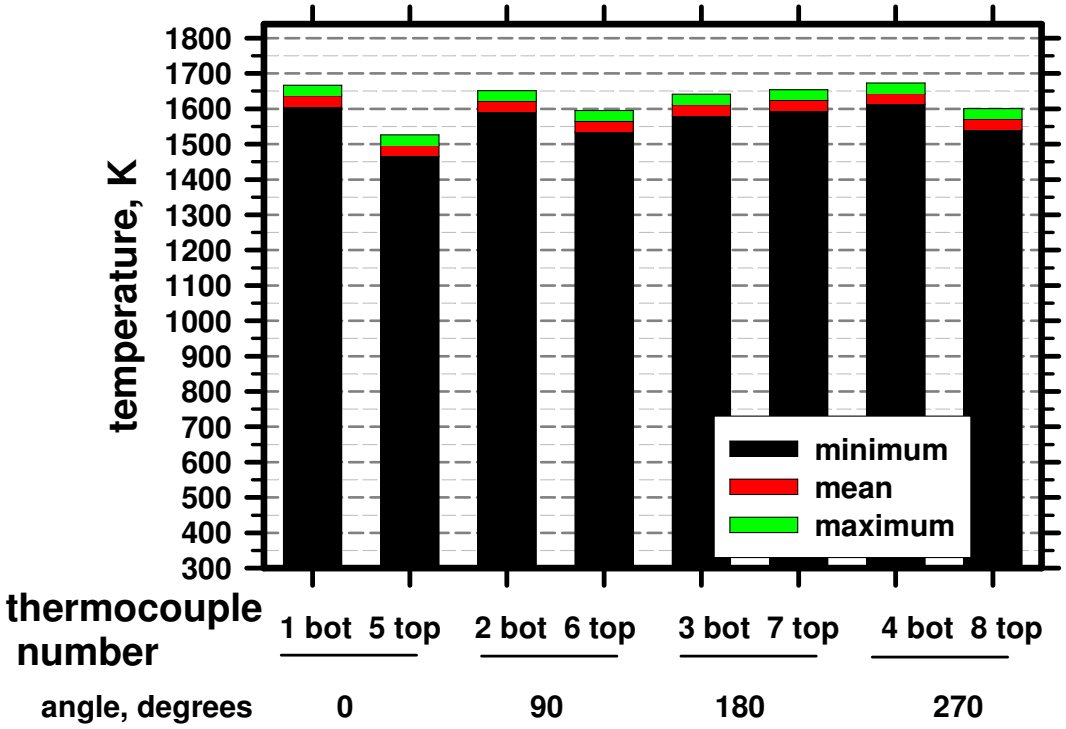

Figure G4: Minimum, midpoint, and maximum steady state temperatures for simulation #2.

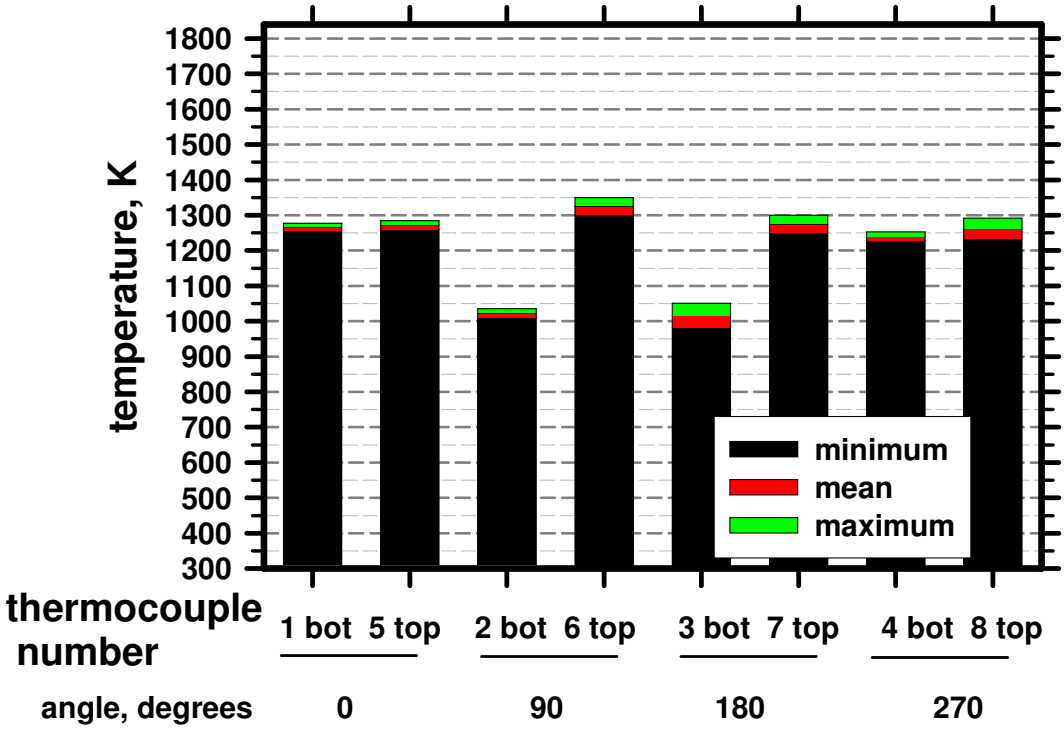

Figure G5: Minimum, midpoint, and maximum steady state temperatures for simulation #3.

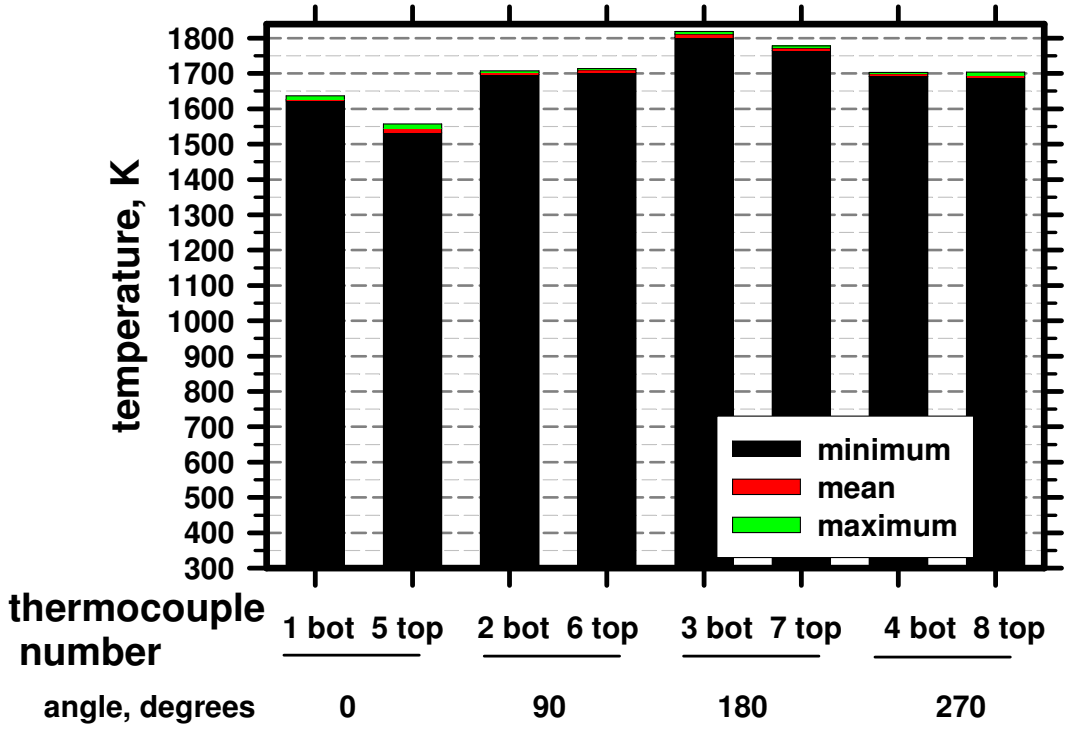

Figure G6: Minimum, midpoint, and maximum steady state temperatures for simulation #4.

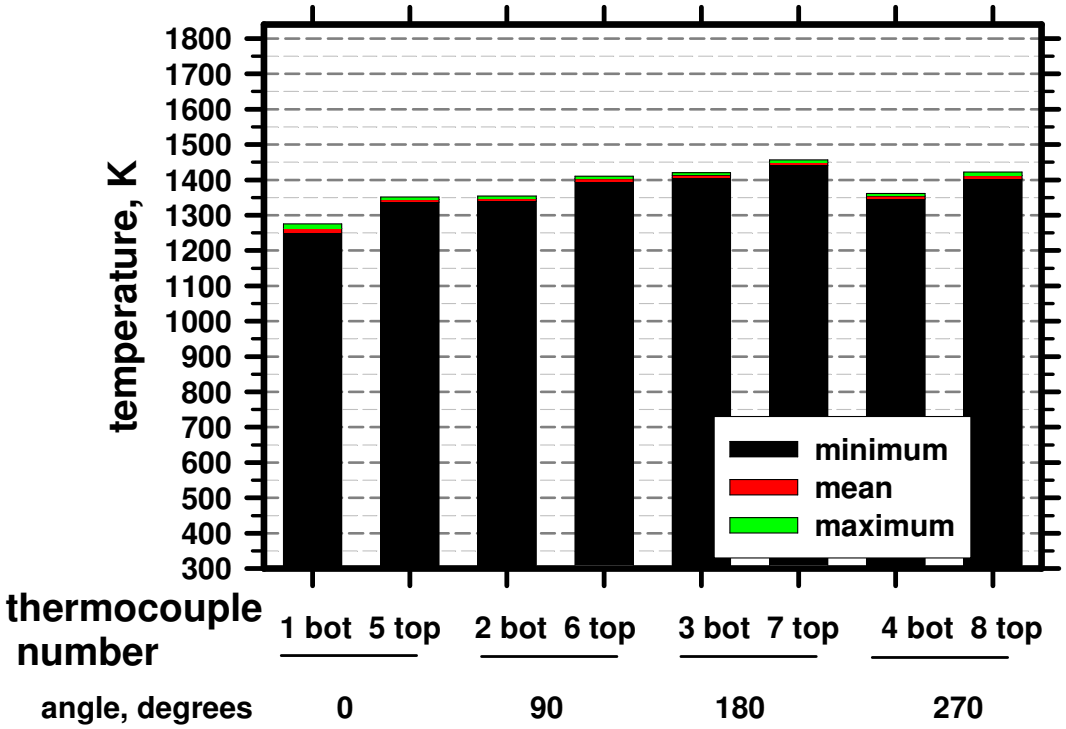

Figure G7: Minimum, midpoint, and maximum steady state temperatures for simulation #5.

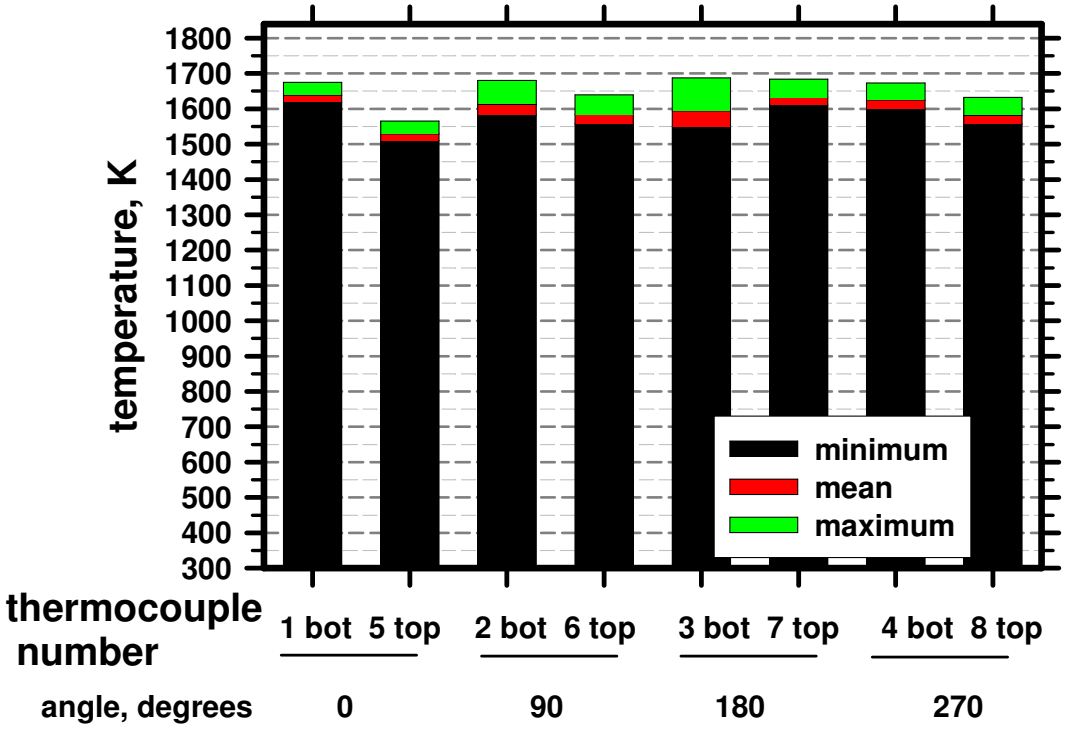

Figure G8: Minimum, midpoint, and maximum steady state temperatures for simulation #6.

Appendix H. Plotted Experimental and Simulation Uncertainties and Comparisons

Figure H1. Thermocouple 1 Experimental and Simulation Uncertainties and Comparisons

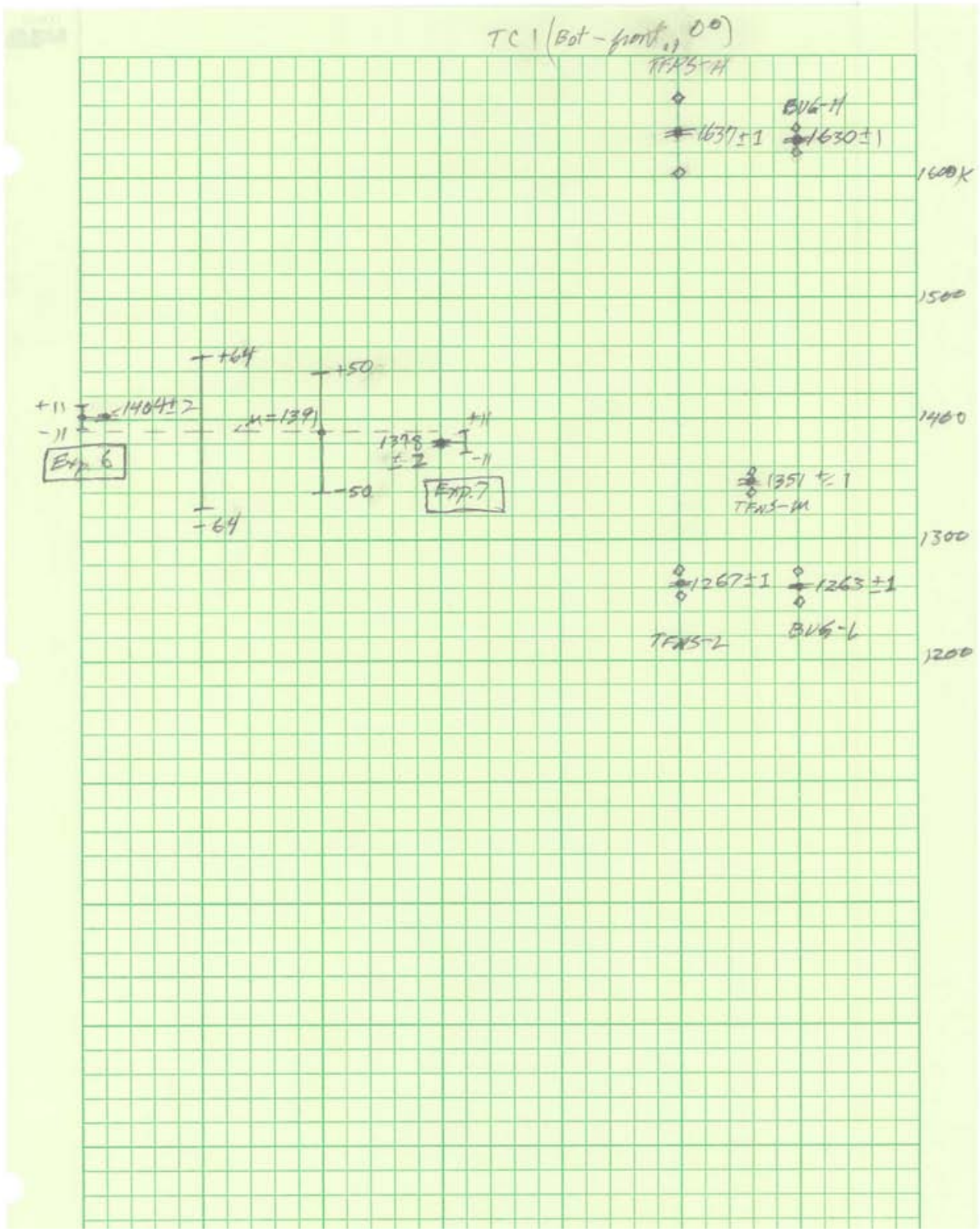

Figure H2. Thermocouple 2 Experimental and Simulation Uncertainties and Comparisons

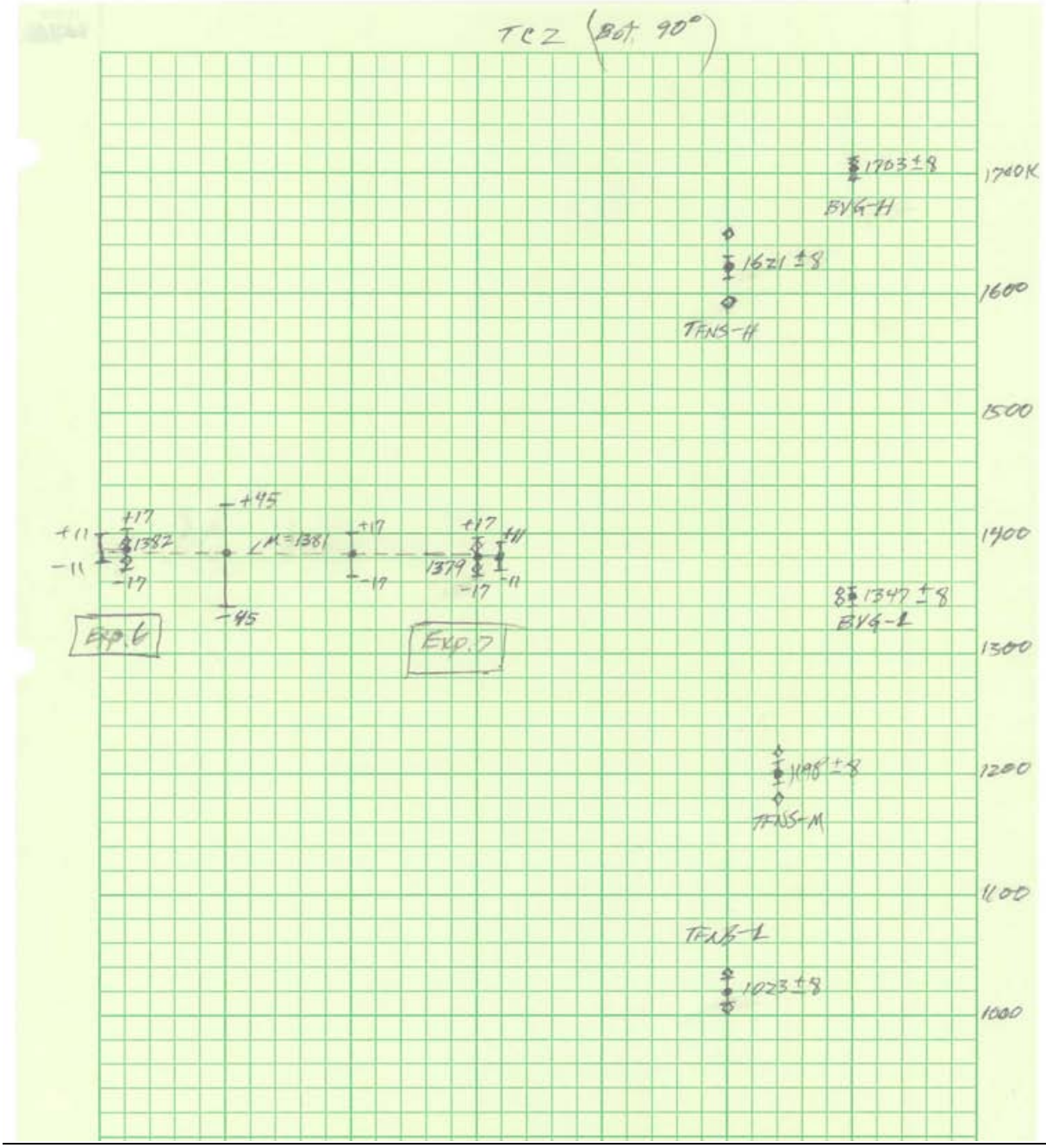

Figure H3. Thermocouple 3 Experimental and Simulation Uncertainties and Comparisons

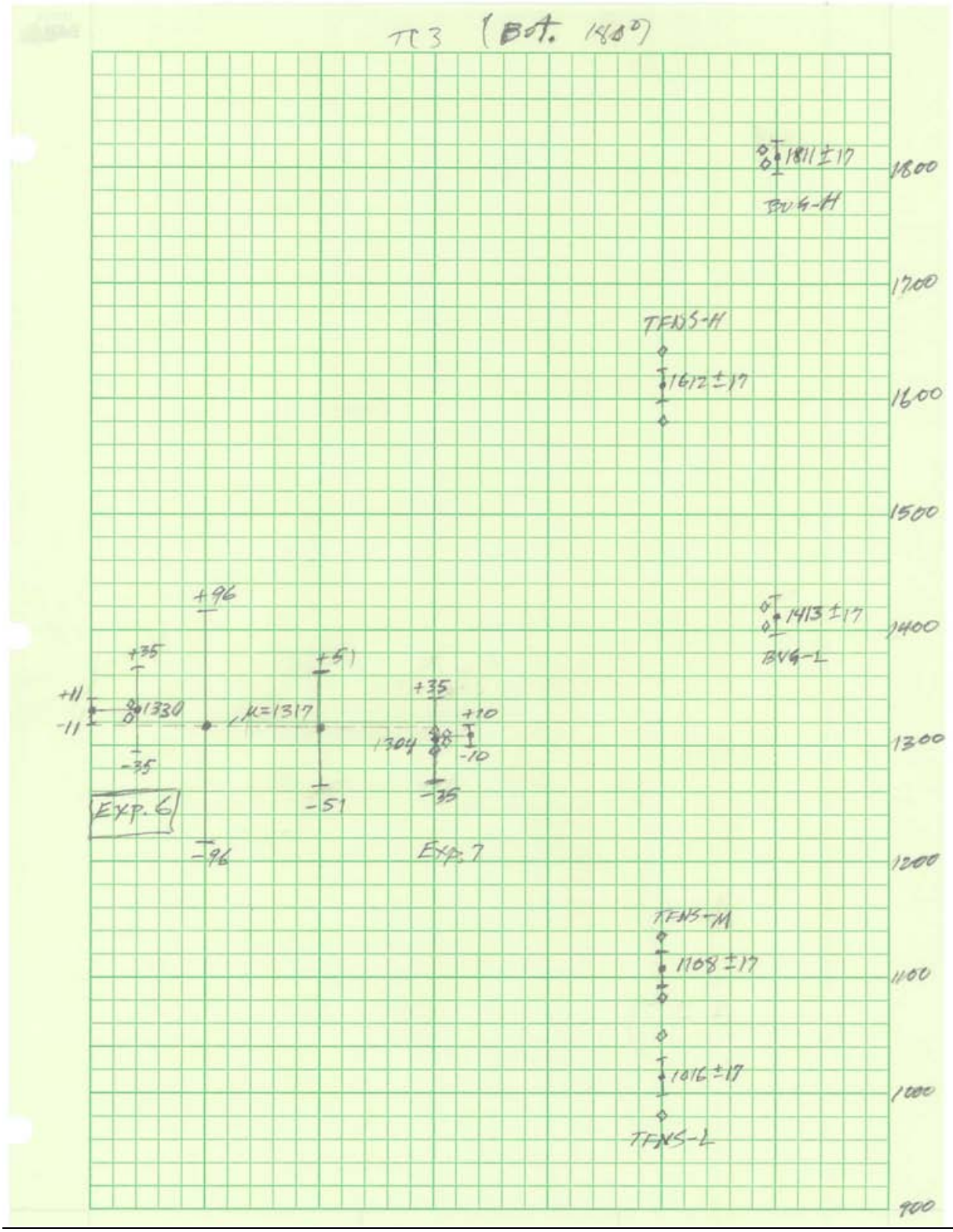

Figure H4. Thermocouple 4 Experimental and Simulation Uncertainties and Comparisons

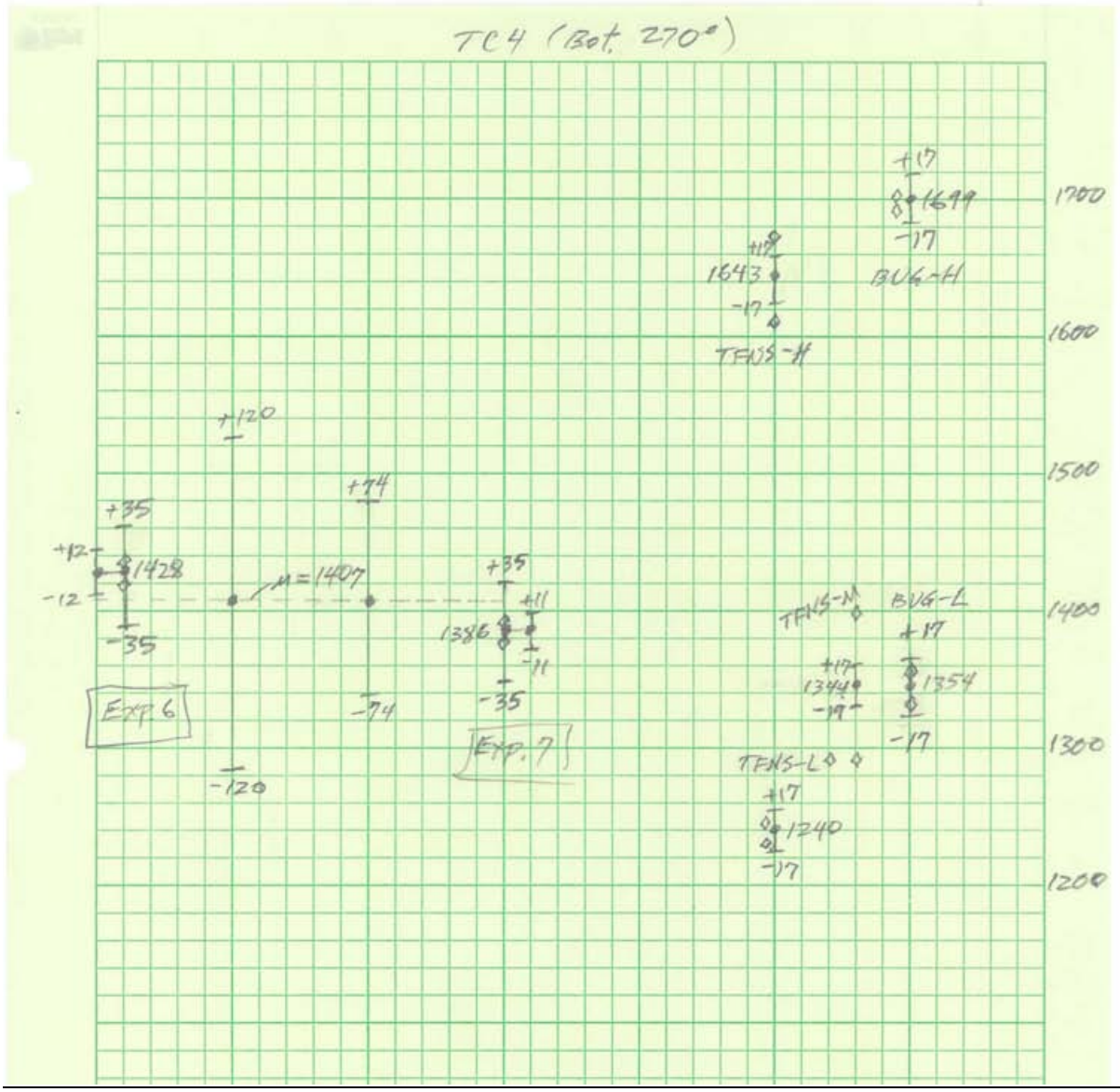

Figure H5. Thermocouple 5 Experimental and Simulation Uncertainties and Comparisons

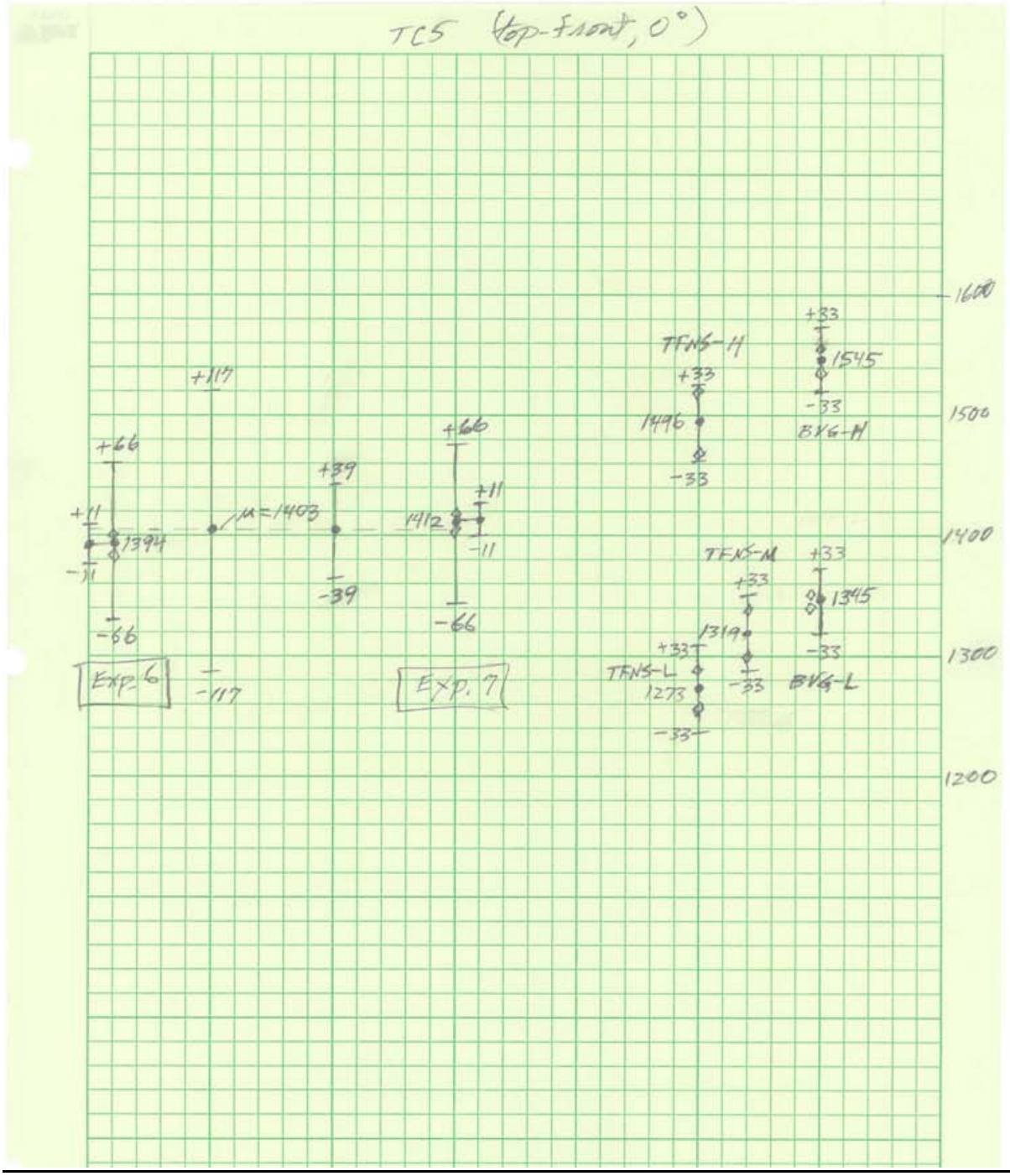

Figure H6. Thermocouple 6 Experimental and Simulation Uncertainties and Comparisons

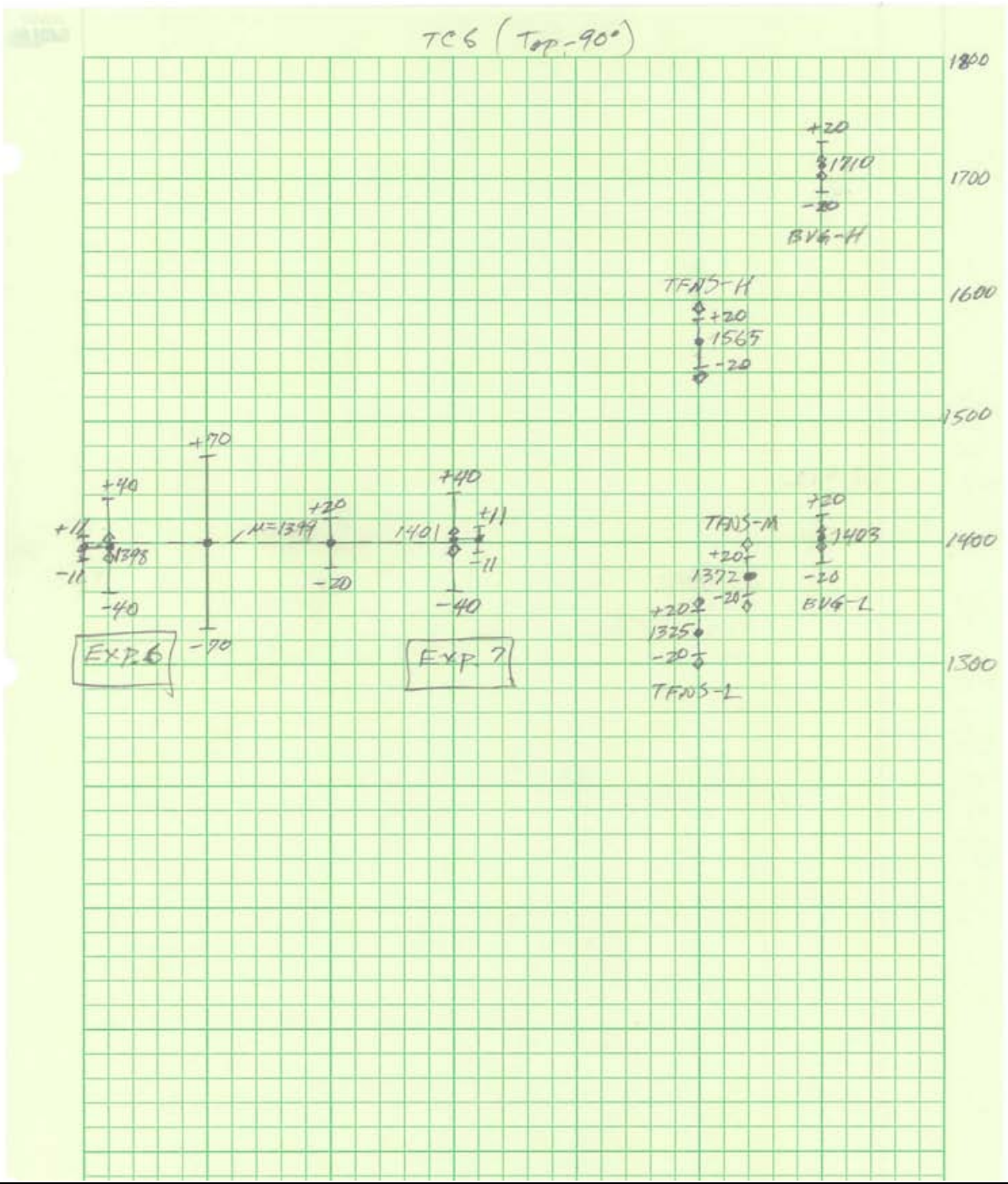

Figure H7. Thermocouple 7 Experimental and Simulation Uncertainties and Comparisons

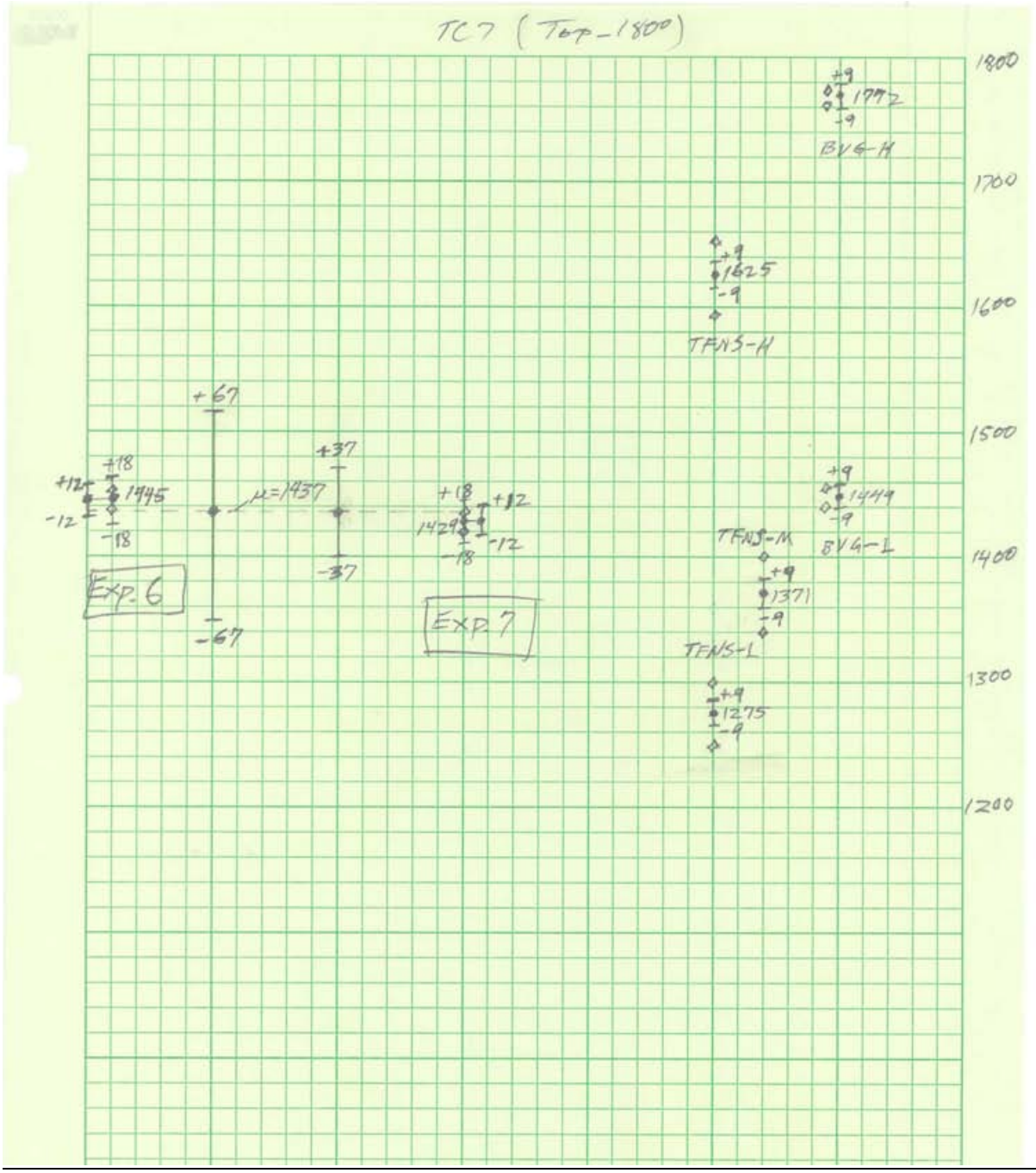

Figure H8. Thermocouple 8 Experimental and Simulation Uncertainties and Comparisons

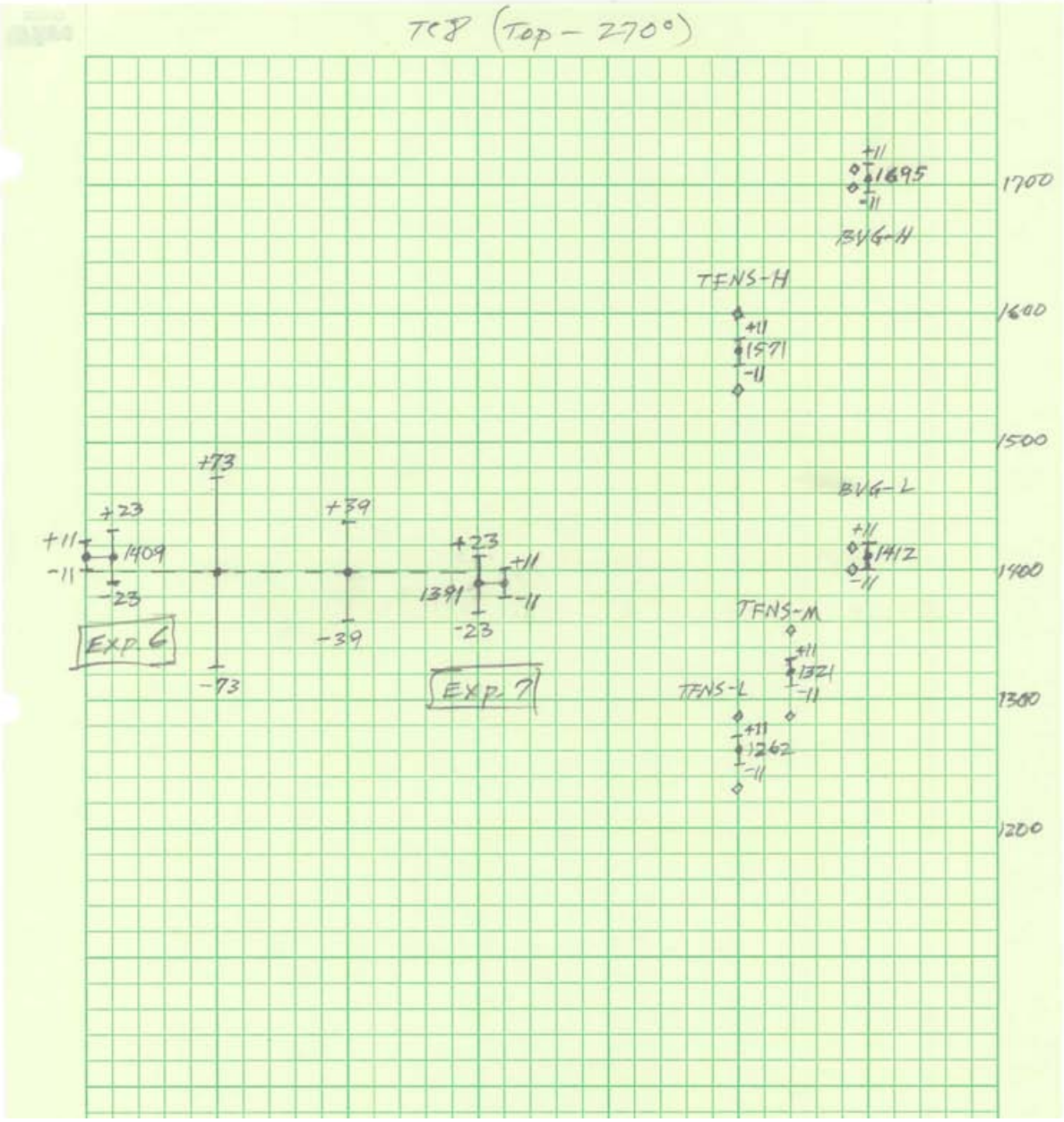

Distribution:

Sandia National Laboratories

1	MS-0384	01500	A. Ratzel
1	MS-0405	12346	R.E. Kreutzfeld
1	MS-0405	12347	T.D. Brown
1	MS-0405	12347	L-J Shyr
1	MS-0481	02132	S.G. Barnhart
1	MS-0481	02132	S.E. Slezak
1	MS-0481	02137	J.F. Nagel
1	MS-0481	02137	B. Boswell/T. Hendrickson
1	MS-0492	12332	H. K. Schriner
1	MS-0633	02952	T. Sterk/B. Bainbridge
1	MS-0718	06765	V. Figueroa
1	MS-0821	01530	A. Thornton
1	MS-0828	01551	M. Pilch
1	MS-0828	01544	A. Black
1	MS-0828	01544	V. Romero
1	MS-0828	01544	M. Sherman
1	MS-0836	01516	D. Dobranich
1	MS-0836	01532	W. Gill
1	MS-0836	01541	S. Domino
1	MS-0836	01541	D. Glaze
1	MS-1135	01532	T. Blanchat
1	MS-1135	01532	J.T. Nakos
1	MS-1135	01532	S. Tieszen
1	MS-1135	01532	A. Brown
1	MS-1135	01532	A. Luketa
1	MS-1135	01532	V. Nicolette
1	MS-1135	01532	J. Hewson
1	MS-0899	04536	Technical Library, 9536 (electronic copy)